Iraqi J. Laser, issue 1, vol., 21, pp. 1-9 (2022)

IRAQI JOURNAL OF LASER

Tunable Optical filters Using Etched Polarization Maintaining Fiber Hybrid Sagnac Interferometer

Raisan M. Taher[1] and Tahreer S. Mansour[1,*]

**Corresponding author: Tahreer@ilps.uobaghdad.edu.iq*

1- Institute of Laser for Postgraduate Studied, University of Baghdad, Baghdad, Iraq.

(Received 15/01/2022; accepted 02/03/2022)

Abstract: In modern optical communication system, noise rejection multiple access interference (MAI) must be rejected in dense access network (DAN). This paper will study the dual optical band pass and notch filters. They will be extracted with tunable FWHM using 10cm (PMF) with different cladding diameters formed with etching 125µm PMF after immersing it with 40% of hydrofluoric acid (HF). This fiber acts as assessing fiber to perform Sagnac interferometer with splicing regions that placed 12cm (SMF) for performing hybrid Sagnac interferometer that consists of Mach-Zehnder instead of Sagnac loop which is illuminated by using laser source with centroid wavelength of 1546.7nm and FWHM of 286 pm or 9 ns in the time domain. . Firstly, Three PMF with the same lengths but with different etching durations (10, 20 and 30) min. Secondly, each of these PMFs with different etching durations will affected under tunable stressing forces (10, 20, 50 and100) g applying on cross sectional area and two weights of (5, 10, 25 and 50) g putting on both micro splicing area separately. The minimum FWHM of dual optical band pass and notch filters at specific etching time with mechanical forces getting the best values equal to 123pm and 90pm, respectively. The study found that the HSI interferometer can be used efficiently as a narrow notch filter in integrated optical communication systems since it has high sensitivity in the pm range.

Keywords: polarization maintaining fiber (PMF), single mode fibers (SMF), hybrid Sagnac interferometer (HSI), FWHM, dual band pass filter, notch filter.

1. Introduction

The generation of ultra-short pulses (USPs) has received a lot of interest among researchers due to the fact that these pulses find potential applications in different fields of science, engineering and medicine [1, 2]. Interferometers have distinctive features such as small size, compactness, noise reduction, bandwidth optimization, simple and low coast implementation capabilities [3, 4], high sensitivity, fast response and immunity to electromagnetic field interference [5]. There are multiple forms of optical fiber interferometers, estimating the fiber Fabry–Pérot interferometer [1], Mach–Zehnder interferometer, Sagnac interferometer and the Michelson [6]. Hybrid inline fiber interferometers accentuate recently as they can enhance sensitivity to sub-pm range, as well as the possibility of selecting best scheme for compact hybrid inline fiber interferometers for the required application [7, 8]. The polymer optical fiber sensor pumped by CO2 laser and achieved strain sensitivity of 28 pm/με [9]. However, there are some drawbacks in the above mentioned interferometers such as complex constructions [7]. Optical fiber-based sensing systems not only require optical band-rejection filters; all-optical signal processing, and optical microwave signal generation also do.

Especially, the notch optical fiber-based filters with limited rejection bandwidths, these are significantly preferred to enhance the detection limit of sensors and enlarge the sensing range [10]. Many intrinsic advantages such as electrically passive operation, remote sensing capability and immunity to electromagnetic interference [11–14]. Several configurations have been employed, such as fiber Bragg gratings (FBGs) [15, 16]. In 2015, Fahad M. Abdulhussein, et al. used two schemes for simultaneous measurements sensors, the first one is with dual FBGs peaks. Every FBG acts as sensing head. The first peak was used for temperature sensing and the obtained sensitivity is 10 pm/˚C and the second peak was used for temperature and pressure measurements with sensitivities 9.2 pm/˚C and 67 pm/ bar for temperature and pressure respectively [17, 18]. OFIs including Fabry-Perot interferometers (FPIs) [18–21], Mach-Zehnder interferometers (MZIs) [22–24] and fiber. Sagnac interferometers (FSIs) [25, 26] are good candidates for highly sensitive temperature sensors. The applied forces imposed stress on the fiber caused elongation in the length of the fiber. The amount of the fiber elongation can be calculated using equations (1) (2), (3) [27].

$$The\ strain = \frac{\Delta L}{L} = \frac{stress}{young\ modulus} \quad (1)$$

$$stress = \frac{Force\ (N)}{Area(m^2)} \quad (2)$$

$$F = m \times G \quad (3)$$

Where: L, is the original length and fixed, ΔL is the change in length, F, is the force applied in (N), A, is the cross sectional area in (m^2), m, is the value of the standard weight mass used to induce mechanical force and G, is the gravitational acceleration. In previous our group studies, the micro splicing regions will be acts as a double convex lenses made from one materials (fused Silica), which produced collapse of splicing regions, so mechanical force will be changed focal length of the convex lenses. But the mechanical force that applied on cross sectional area will made filter elongations (ΔL) that measures in micro strain [28].

Young's modulus is the modulus of elasticity ranges from 66 Gpa to 74 Gpa for the SiO2 i.e. 70 Gpa [29].

After converting weights to force, the mechanical forces in this work were done by applying different forces (0.098, 0.196, 0.49, and 0.98) (N) on the interferometer micro–cavities cross sectional area and applied (0.049, 0.098, 0.245, 0.49) (N) on the micro cavity splicing regions of Pm-MZI.

2. Experimental setups

The hybrid Sagnac interferometer which consists of Mach-Zehnder instead as a loop that means two micro cavity splicing regions (MCSRs), and connected MZI by FC-SC adapter to the coupler 2×2 which will make Sagnac interferometer. Figure (1) shows the schematic diagram for the experimental setup for the tunable singe PM-Mach Zehnder Sagnac interferometer. one cavity length (Lc) connected in the loop of Sagnac interferometer, the PMF had etched with the hydrofluoric acid (HF) of 40 % concentration, for (10, 20 and 30) min adding to case without etching. Then mechanical forces were varied from (10, 20, 50, and 100) g applied on the cross sectional area and to splicing regions separately with various weights (5, 10, 25, and 50) g.

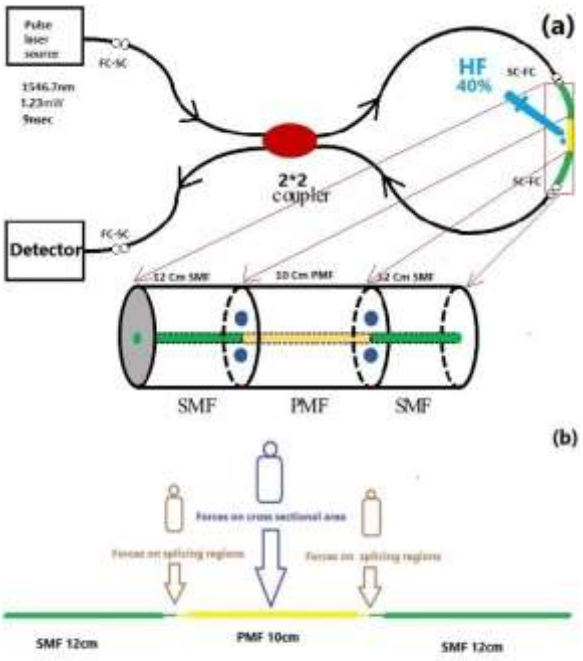

Figure (1): schematic diagram of (a) Sagnac with loop PM-MZI (b) how forces applied on cross sectional area and splicing region separately.

The length of Sagnac interferometer totally (2.34m). And get more details about etching time with HF shows in Figure (2).

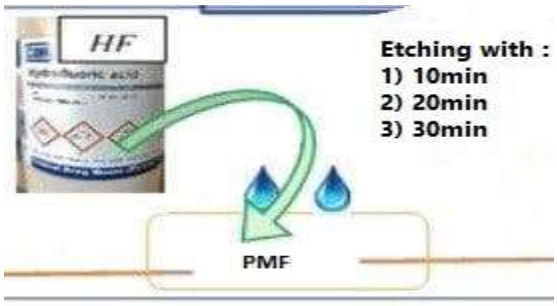

Figure (2): the stages of etching with HF of 40 % concentration.

In this experiment, an optical pulse laser source launched to PM-Mach Zehnder Sagnac interferometer. PM-MZI was building by using PMF with the same lengths and different etching times, each of states will give different results according to change in mechanical forces as shown in figure (3).

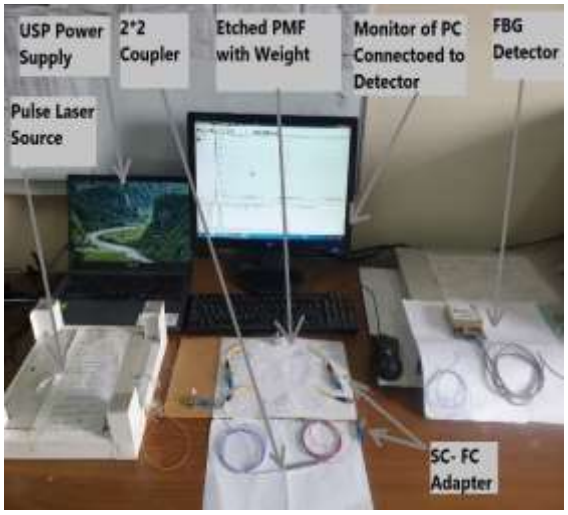

Figure (3): The experimental setup for Sagnac interferometer with loop MZI- PM.

The thickness of PMFs cladding is varying according to etching time of the PMF by 40% of HF with durations (10, 20 and 30) min as shown in table (1), it measured by microscope with 40 X magnifications.

Table (1): Fiber diameter with respect to etching time.

Time of etching (min)	Fiber diameter as a function of etching (μm)
10	112.393
20	72.532
30	69.651

3. Results and discussions

The results divided into two parts, the first part is the relationship between the forces which applied on both cross sectional area and micro-cavities splicing regions with FWHM of dual band pass and notch filters. The second part regarding the effects of etching PMF with different times on the previous results under the same tuning.

The FWHM using HSI with PMF-MZ (as loop) got different results. The minimum FWHM for dual band pass and notch filters are 123 pm, 90 pm respectively when etching at 10min with affecting by weights 100g on cross sectional area and same result was found when use etching at 10min with affecting by weights 10g on both splicing regions. The maximum FWHM for dual band pass and notch filters is 315pm, 125pm respectively was achieved by etching at 20min PMF and affected by weights 50g on cross sectional and the same result was found when using etching at 20min PMF and affected by weights 25g on both splicing regions. All these results shown in the table (2).

Table (2): maximum and minimum value of FWHM according to etching and stress.

Etching PM (min)	Force (N)	FWHM of dual band pass filter (pm)	FWHM of notch filter (pm)
10	0.098 on splicing regions	123	90
10	0.98 on cross area	123	90
20	0.245 on splicing regions	315	125
20	0.49 on cross area	315	125

Due to the high sensitivity of the interferometers, the experimental results of the hybrid Sagnac interferometer with loop PM-MZI under the effect of PM fiber etching for three different cladding diameters adding to original diameter before etching showed optical notches occurring in the optical FWHM of the input laser after getting out of interferometer, this promising result opens the door on using it as a very narrow optical notch pass filter.

All these results will show by the FBGA interrogator as a visualizer.
The effect of two types of filter appeared in the output of setup because PMF has zero PMD (polarization mode dispersion) but this effect disappear by using long SMF (1m) or three paddles PC, so different SMF has large polarization mode dispersion (PMD) but PMF has zero (PMD), which can controlled by its beat length BL

The first case using the PM without etching and applied the mechanical stress as shown in figure (4) which show signals and FHWM of dual band pass filter in the range (126 – 285) pm, and notch filter in range (95 – 114) pm.

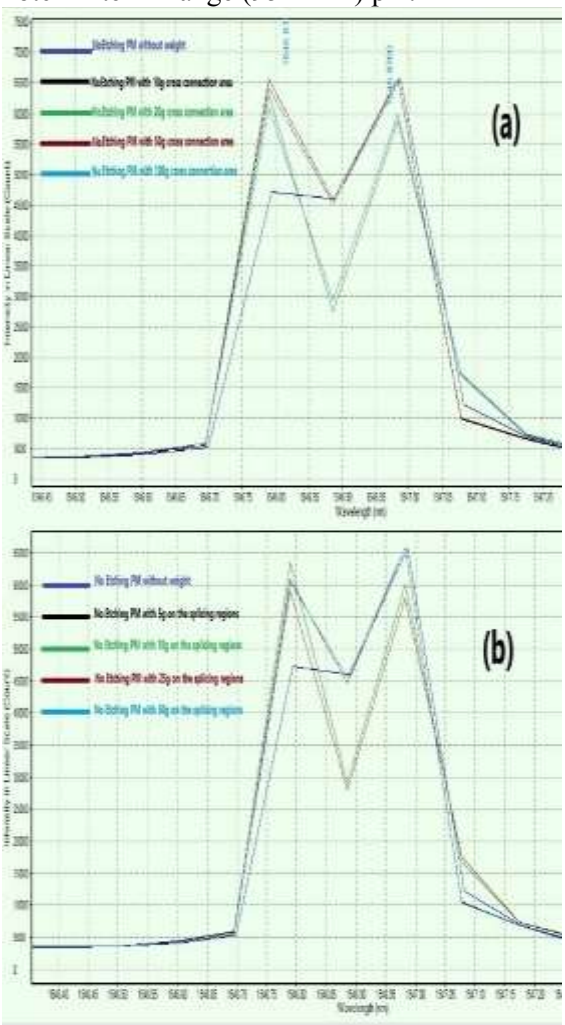

Figure (4): for PMF without etching connected to Sagnac loop adding to (a) weights on cross sectional area (b) weights on the splicing regions

The second case using the PM with etching 10min and applied the mechanical stress as shown in figure (5) which show signals and FHWM of dual band pass filter in the range (123 – 293) pm, and notch filter in range (90 – 115) pm.

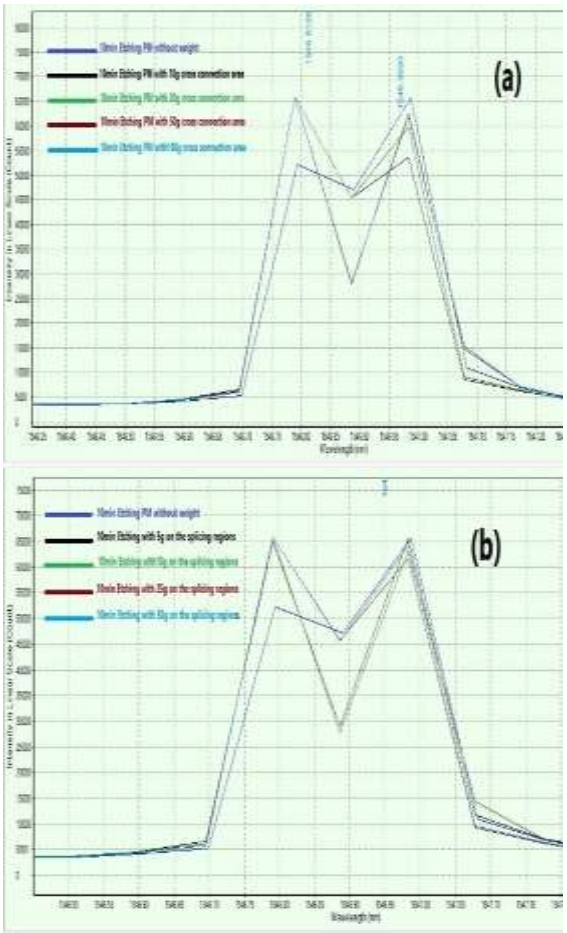

Figure (5): for PMF 10min etching connected to Sagnac loop adding to (a) weights on cross sectional area (b) weights on the splicing regions.

The third case using the PM with etching 20min and applied the mechanical stress as shown in figure (6) which show signals and FHWM of dual band pass filter in the range (137 – 315) pm, and notch filter in range (102 – 125) pm.

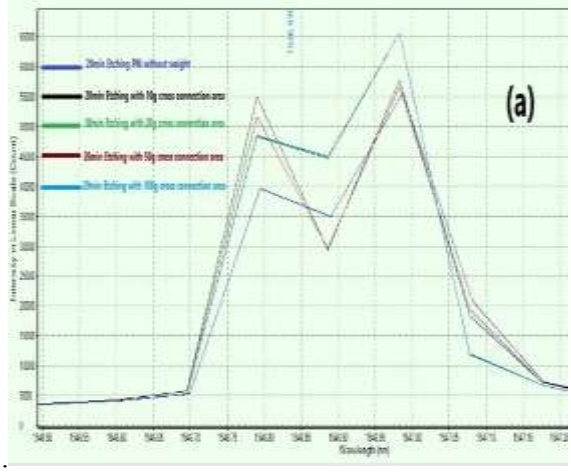

.

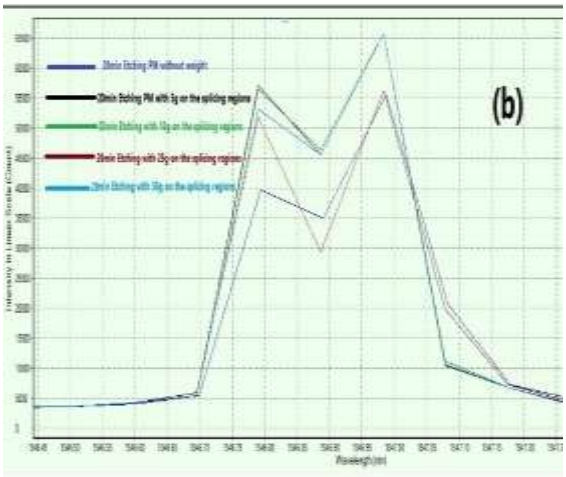

Figure (6): for PMF 20min etching connected to Sagnac loop adding to (a) weights on cross sectional area (b) weights on the splicing regions.

The forth case using the PM with etching 30min and applied the mechanical stress as shown in figure (7) which show signals and FHWM of dual band pass filter in the range (130 – 308) pm, and notch filter in range (99 – 122) pm.

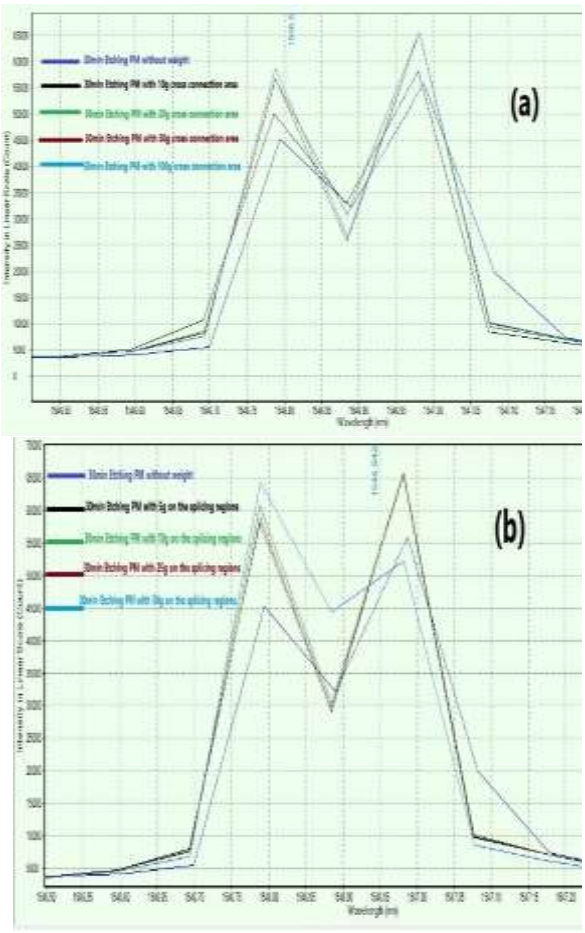

Figure (7): for PMF 30min etching connected to Sagnac loop adding to (a) weights on cross sectional area (b) weights on the splicing regions.

When applied weight on cross sectional area of PM as part of MZI in the loop of hypbrid Sagnac interferomerter will get many results for FWHM(by tuning weights and etching). These results of FWHM will be increased by increasing etching time at the same weights.
Regarding applied weights on both splicing regions will get maximum result for FWHM at the same weights for PM with 20min etching , each of these results are summarized in the figure (8).

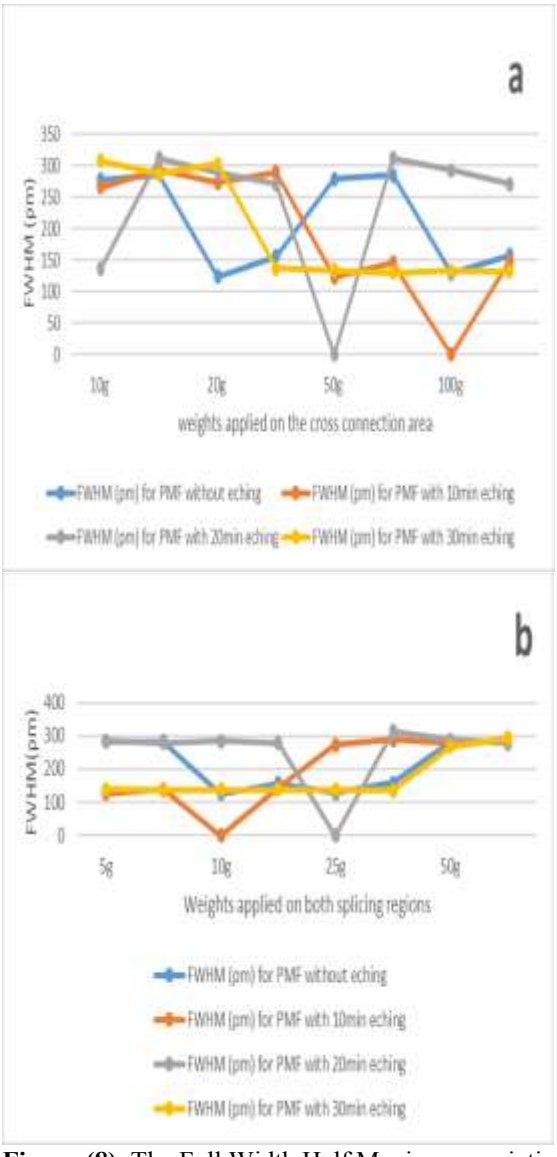

Figure (8): The Full Width Half Maximum variation of HIS which contained PM-MZI as loop (a) for weights apply on cross sectional area (b) for weights apply on the both splicing regions.

The peak wavelength is changed by tuning of etching adding to other parameters which contained weights and get two peaks and involving notch between them , these peaks will

be in different values from (1546.808 nm - 1546.972 nm) , each of these results are summarized in the figure (9).

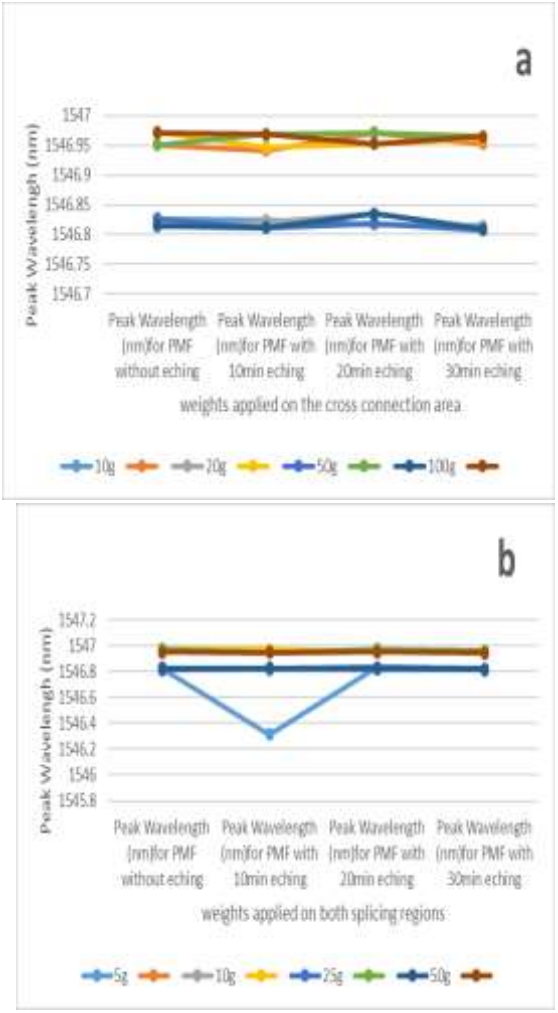

Figure (9): The peak wavelength variation of HIS which contained PM-MZI as loop (a) for weights apply on cross connection area (b) for weights apply on the both splicing regions.

In this paper took etching 10 min for PMF and make relation for result between forces (N) and the strain as show in figure (10)

The FWHM results of notch filter at 10 min etching with weights on cross connection area are summarized in table (3).

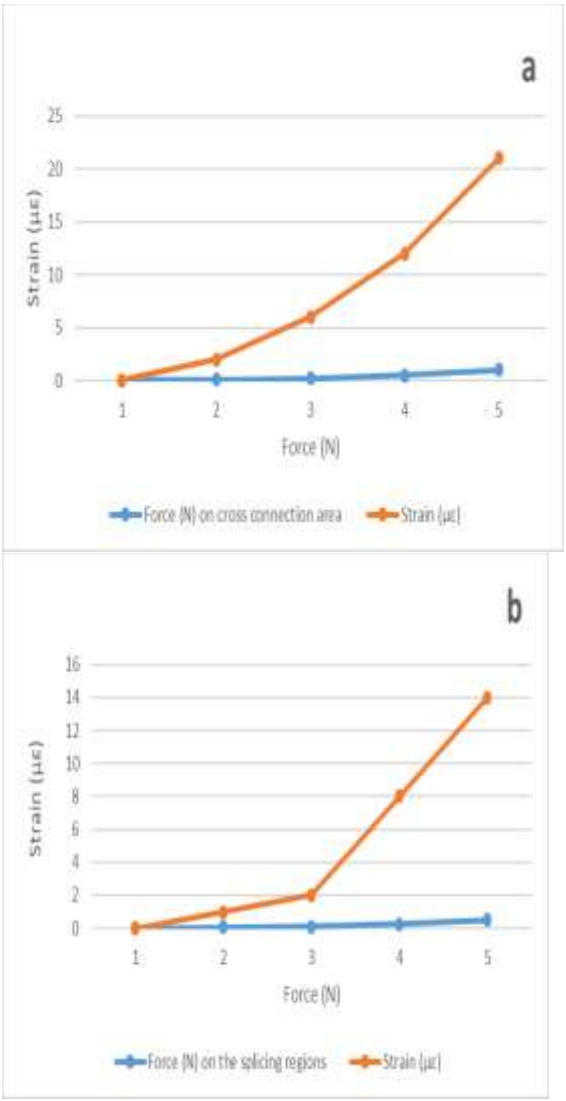

Figure (10): The relation between Mechanical force and strain (με) (a) for weights apply on cross connection area (b) for weights apply on the both splicing regions.

Table (3): FWHM of notch filter with respect to weights on cross connection area.

Weights on cross connection area (g)	FWHM (pm) for of notch filter
10	125
20	128
50	98
100	90

The FWHM results of notch filter at 10 min etching with weights on splicing regions are summarized in table (4).

Table (4): FWHM of notch filter with respect to weights on splicing regions.

Weights on splicing regions (g)	FWHM (pm) for of notch filter
5	99
10	90
25	132
50	134

The FWHM results of dual band pass filter at different duration of etching with weights on cross connection area are summarized in table (5).

Table (5): the result of FWHM of weights applied on cross connection area with different etching.

Weights on cross area (g)	FWHM at no etching (pm)	FWHM at 10 min (pm)	FWHM at 20min (pm)	FWHM at 30min (pm)
10	278	266	137	308
	286	293	312	287
20	127	273	290	303
	156	290	271	137
50	279	141	315	134
	285	146	314	130
100	129	123	293	133
	158	124	271	132

The FWHM results of dual band pass filter at different duration of etching with weights on splicing regions are summarized in table (6).

Table (6): the result of FWHM of weights applied on splicing regions with different etching.

weights on splicing regions (g)	FWHM at no etching (pm)	FWHM at 10 min (pm)	FWHM at 20min (pm)	FWHM at 30min (pm)
5	282	127	285	139
	283	139	279	135
10	126	123	284	137
	157	124	278	138
25	129	274	315	138
	159	288	314	136
50	282	276	288	267
	282	287	276	294

The highest peak power intensity value in watt per square meter was recorded result in the case of no etching is 74564.513 which equal to (914.58 µW) as peak power, in case of 10min etching (977.36 µW) in case of 20min (914.857 µW) and in case of 30min (933.635 µW), the figure (11) show the peak power of HIS which contained PM-MZI as loop after applying different values of mechanical forces as different weighs applied on cross and splicing regions.

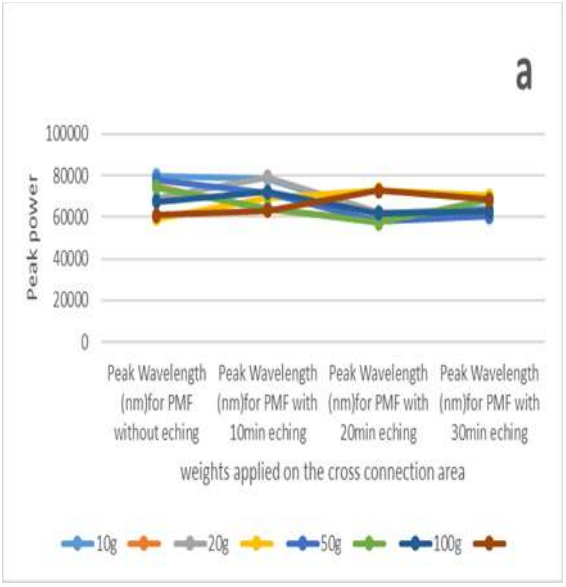

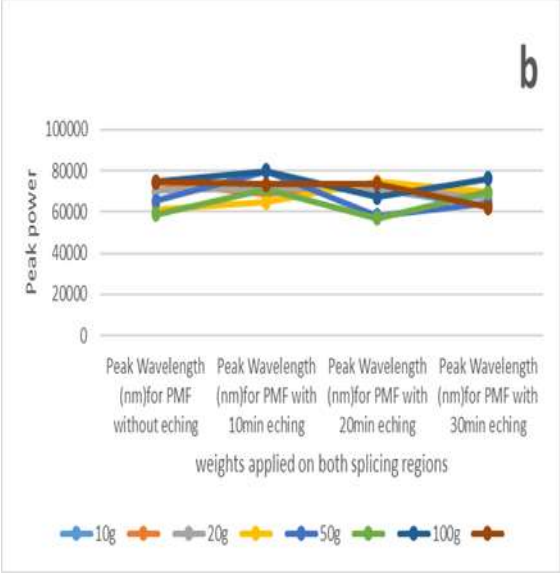

Figure (11): The peak power intensity variation of HIS which contained PM-MZI as loop (a) for weights apply on cross connection area (b) for weights apply on the both splicing regions.

4. **Conclusion**

In conclusion; a simple structure, low cost all optical notch pass filter was designed and the main point that the better filter with narrow FWHM for dual band pass filter and notch filter can be obtained by using hybrid Sagnac interferometer with MZI of PM as a loop with etching 10 min and affected by weights 100g (Force 0.98 N) on cross sectional area or by weights 10g (Force 0.098) on both splicing regions equal to 123 pm and 90 pm, respectively. These results are promising to make possible the acquisition of narrowband pass filters and slit filters for telecom applications. When the FWHM decrease in the frequency domain as it is increasing in the time domain that occurs because there is an inverse relationship between frequency and time. The average power decreased with increase the duration of etching PM in MZI due to change in FWHM of the output signal. It can be used in all optical integrated signal processing devices to reduce the electronics and their characteristics noise there by achieving higher data processing and transmission rates.

References

[1] K. Agrawal, G.P. "*Application of Nonlinear Fiber Optics*", 2nded. Academic Press: New York, (2001).

[2] D. V. Skryabin, "*Coupled core-surface solitons in photonics crystal fibers*," Opt. Express 12, 4841–4846 (2004).

[3] B. Lee, Young Ho Kim 1, Kwan Seob Park, Joo Beom Eom, Myoung Jin Kim, Byung Sup Rho and Hae Young Choi "*Interferometric Fiber Optic Sensors*" Sensors, vol:12, PP.10430-10449, (2012)

[4] S. Korposh, Stephen W. James, Seung-Woo Lee and Ralph P. Tatam "*Tapered Optical Fibre Sensors: Current Trends and Future Perspectives*", Sensors, vol. 19, No. 2294, (2019).

[5] Wu, Shun, et al. "*Temperature-independent ultra-sensitive refractive index sensor based on hollow-core silica tubes and tapers*." Optics Express 29.7, PP. 10939-10948, (2021).

[6] Wang, Jin, et al. "*Temperature insensitive fiber Fabry-Perot/Mach-Zehnder hybrid interferometer based on photonic crystal fiber for transverse load and refractive index measurement.*" Optical Fiber Technology 56, No.102163, (2020).

[7] Peng, Wei, et al. "*Miniature fiber-optic strain sensor based on a hybrid interferometric structure."* IEEE Photonics Technology Letters 25.24, PP. 2385-2388 (2013).

[8] Yi, Liu, and Yu Changyuan. "*Highly stretchable hybrid silica/polymer optical fiber sensors for large-strain and high-temperature application*." Optics express 27.15, PP. 20107-20116, (2019).

[9] Zhao, Ping, Lei Shi, and Xinliang Zhang. "*Single-notch filter based on a compact asymmetric microfiber coupler*." CLEO: QELS Fundamental Science. Optical Society of America, 2013.

[10] J. Yang, Y. Zheng, L. H. Chen, C. C. Chan, X. Dong, P. P. Shum, and H. Su, "*Miniature temperature sensor with germania-core optical fiber*" Opt. Express 23(14), PP.17687–17692, (2015).

[11] Zhao, Yong, et al. "*A ring-core optical fiber sensor with asymmetric LPG for highly sensitive temperature measurement*." IEEE Transactions on Instrumentation and Measurement 66.12, PP. 3378-3386, (2017).

[12] Xu, Zhilin, et al. "*Investigation of temperature sensing characteristics in selectively infiltrated photonic crystal fiber*." Optics express 24.2, PP.1699-1707, (2016).

[13] Wu, Zhifang, et al. "*Supermode Bragg grating combined Mach-Zehnder interferometer for temperature-strain*

discrimination." Optics express 23.26, PP.33001-33007, (2015).

[14] Zhang, Zhe, et al. "*Hollow-core-fiber-based interferometer for high-temperature measurements.*" IEEE Photonics Journal 9.2, PP.1-9, (2017).

[15] Yang, Jingyi, et al. "*Magnetic field sensing with reflectivity ratio measurement of fiber Bragg grating*." IEEE Sensors Journal 15.3, PP. 1372-1376, (2014).

[16] V. Bhatia and A. M. Vengsarkar, "*Optical fiber long-period grating sensors*," Opt. Lett. 21(9), PP.692–694, (1996).

[17] F. M. Abdulhussein, M. Hou, S. Liu, T. S. Mansour, and P. Lu, "*Integrated FabryPerot/Fiber Bragg Grating Sensor for Simultaneous Measurement*" in CLEO: 2015, OSA Technical Digest (online) (Optical Society of America, (2015) .

[18] T. S. Mansour and F.M. Abdulhussein, "*Dual Measurements of Pressure and Temperature With Fiber Bragg Grating Sensor*", Vol.11,pp.86-91,(2015).

[19] T. Zhu, T. Ke, Y. Rao, and K. S. Chiang, "*Fabry-Perot optical fiber tip sensor for high temperature measurement*," Opt. Commun. 283(19), 3683–3685 (2010).

[20] Y. Zhang, L. Yuan, X. Lan, A. Kaur, J. Huang, and H. Xiao, "*High-temperature fiber-optic Fabry-Perot interferometric pressure sensor fabricated by femtosecond laser*," Opt. Lett. 38(22), 4609–4612 (2013).

[21] L. Jiang, J. Yang, S. Wang, B. Li, and M. Wang, "*Fiber Mach-Zehnder interferometer based on microcavities for high-temperature sensing with high sensitivity,*" Opt. Lett. 36(19), 3753–3755 (2011).

[22] J. Zhu, A. Zhang, T.-H. Xia, S. He, and W. Xue, "*Fiber-optic high-temperature sensor based on thin-core fiber modal interferometer*," IEEE Sens. J. 10(9), 1415–1418 (2010).

[23] Abdulwahhab, A. A., and T. S. Mansour. "*Design and Analysis of BIMD Double Clad MMF -MZI Using Optiwave Simulation*". Iraqi Journal of Laser, vol. 20, no. 1, Aug. 2021, pp. 1-5, (2021).

[24] Y. Liu, B. Liu, X. Feng, W. Zhang, G. Zhou, S. Yuan, G. Kai, and X. Dong, "*High-birefringence fiber loop mirrors and their applications as sensors,*" Appl. Opt. 44(12), 2382–2390 (2005).

[25] Mansour, T. S., and D. H. Abbass. "*Chemical Sensor Based on a Hollow-Core Photonic Crystal Fiber*". Iraqi Journal of Laser, vol. 12, no. A, pp. 37-42, (2015).

[26] Noori, Nada F., and Tahreer S. Mansour. "*Design and Construction of Tunable Band Pass Filter Using Hybrid FPMZI*." Design Engineering, 6959-6972, (2021).

[27] B. H. Mutar ,N. Faris, Y. I. Hammadi and T. Mansour, "*In-Line Fiber Tunable Pulse Compressor using PM-Mach Zehnder Interferometer*" Journal of Mechanical Engineering Research and Developments. Vol. 44, pp. 287-297, (2021).

[28] Mutar, B. H., and T. S. Mansour. "*Design of Tunable Optical Band Pass Filter Based on in-Line PM-Mach Zehnder Interferometer*". Iraqi Journal of Laser, vol. 20, no. 1, pp. 6-12, (2021).

تنغيم مرشحات النطاق البصري بواسطة سانتياك باستخدام الالياف الضوئية المحافظة عل الاستقطاب المحفورة

ريسان محي الدين طاهر تحرير صفاء منصور

معهد الليزر للدراسات العليا / جامعة بغداد – بغداد / العراق

الخلاصة: في هذا العمل، تم تقديم مرشح تمرير النطاق المتباين المستند ضمن دائرة السانياك وتحتوي دائرته على مقياس التداخل المتراصف المحافظ على الاستقطاب من نوع ماخ – زندر لكي تعمل كتوليف لعملية انتاج مرشح النطاق البصري الضيق. تم تقشير 10سم من هذا الليف (PMF) و ربطه بين جزأين من الالياف احادية النمط من نوع (SMF-28) بطول (12سم) للكل ليف وربطهما بأستخدام تقنيه اللحام الكهربائي و قد تم ازاله جزء من قطر اليف (PMF) بواسطة حامض الهايدروفلوريك أسد وبتركيز 40% وعلى ثلاث مراحل بفترات متزايدة بمقدار 10ثانيه بالاضافة لعمل توليف بواسطة الاوزان المختلفة على مركز الليف (PMF) وكذلك عل مناطقتين اللحام الجانبية، وقد تم الحصول عل مرشح بصري ضيف وبمديات مختلفة حسب التوليف ولكن تم تثبيت افضل قياس في مرحلة الازالة لمدة 10 ثواني مع تسليط اوزان بقيمة 100غرام عل المنطقة الوسطية لليف او 10 غرام علي منطقتي اللحام وتسجيل اضيق مقدار للمرشح و مقدار عرض الموجة FWHM مساويا 123 بيكو متر للمرشحات المزدوجة و 90 بيكو متر لمرشح الشق. علما ان مصدر اليزر النبضي المستخدم في هذا العمل له ذروة تبلغ 1.2296 ملي واط، FWHM 286 بيكو متر، ويتركز عند الطول الموجي 1546.7 نانومتر.

Iraqi J. Laser, issue 1, vol., 21, pp. 10-17 (2022)

IRAQI JOURNAL OF LASER

Fiber Laser Effect on Bond Strength of Titanium implant abutment to Resin Cement

Ruba Husam Abdulrazzaq[1,*], Basima Mohammed Ali Hussein[1]

** Corresponding Author:* roba.hossam1202a@ilps.uobaghdad.edu.iq
basma.moh@ilps.uobaghdad.edu.iq

1- Institute of Laser for Postgraduate Studies, University of Baghdad, Baghdad, Iraq

(Received 31/01/2022; accepted 30/06/2022)

Abstract: Aim: surface modification of titanium using fiber laser 1064 nm to enhance the bond strength to resin cement. **Material and Methods:** thirty titanium discs of 0.6 cm x 0.3 cm (diameter and thickness respectively) were categorized after preparation into three groups (n=10) as follows: control group with no surface treatment and two test groups were treated with fiber laser after estimation the appropriate parameters in the pilot study which are 81 ns pulse duration, 30,000 Hz frequency, 50 µm spot size and 10,000 mm/s scanning speed and different average power values (10 W and 20 W) depending on the tested group. Titanium discs surface characterization was performed by scanning electron microscope (SEM), and surface roughness tester. Following these tests, resin cement application to titanium discs was performed. Shear bond strength (SBS) values were determined by universal testing machine. ANOVA and Tukey HSD tests were used for analyzing of data ($\alpha = 0.05$).**Results:** Higher average surface roughness (Ra) value was observed in (10 W) group followed by (20 W) group and the lowest surface roughness value was in the control group, additionally lowest SBS value was obtained from the control group and the highest SBS value was obtained from (20 W) group followed by (10 W) group. **Conclusion:** bond strength between titanium and resin cement can be significantly enhanced by using fiber laser as a surface treatment. Average power of fiber laser is essential parameter in enhancing the roughness of titanium surface and bonding to resin cement.

Keywords: fiber laser, shear bond strength, titanium, surface roughness.

1. Introduction:

The most important part of the dental implant system is implant abutment which could be made of titanium or its alloys or recently zirconia and PEEK were also suggested (Shafie, 2014).

Implant abutment represents the connection between the intra boney part (fixture) with the oral substitute structure (crown, bridge, and denture) therefore; this part may play a great role in the restoration longevity (Iocca, 2016). This obligates to establish well-tolerated connection between the restoration and abutment. Two main connection methods were suggested with the introduction of dental implant in service either screws or cement-retained prosthesis (Chaar et al., 2011). The most popular and easier type is cement retained prosthesis because it does not require complicated steps or preparation with very good results and withstand load (Akin & Guney, 2012).

The connection between implant abutment and restoration can be improved depending on many factors including surface area, height of abutment, abutment taper, type of luting cement and finish or roughness of surface (Sahu et al., 2014). When the surface area of abutment increased, the resistance to dislodgement can be physically increased. Wide surface area could be inherent especially in long or wide diameter abutments, but since dental implant cover a wide range of cases some of these could be with short, small in diameter or angled abutment. All these situations require some modification in implant abutment to improve surface area, which in turn enhances restoration resistance to dislodging functional loads (Oshida et al., 2010). Various techniques were used to enhance the bonding characteristics by surface modification of titanium abutment such as sandblasting, acid etching, electro discharge machining, grinding with bur, or a combination of these methods. Studies have shown that these techniques affect the bond strength at various amount (Ates et al., 2017; Cao et al., 2019; Kim & Cho, 2009). Lasers currently used in medical applications because it performs without residue and can be used safely with minimal precautions or preparations. ((Kim et al., 2020; Safi et al., 2019)

Titanium laser treatment were applied for fixture or restoration, it gave interesting results when proper laser was selected. Fiber laser 1064 nm is among the lasers which well absorbed and interact with titanium. Studies using different lasers as Nd:YAG 1064 nm, CO_2 10600 nm or Er:YAG 2940 nm gave promising results considering surface modification of titanium (Marticorena et al 2007; Yeo, 2020) Fiber laser 1064 nm is among the lasers which is well absorbed by titanium, it used currently in surface texturing and in some biological studies to create favorable modification by cells or proteins (Oktem et al., 2010; Riveiro et al. ,2018). Abutment-laser interaction may result in ablation and surface roughness enhancement, which could increase surface area and creates mechanical interlocking which probably improve retention. This roughness can be also obtained by sandblasting, grinding or etching but with wide range of variations, which may affect on standardization and homogeneity (Ajay et al., 2017).The present study aimed to investigate the effect of fiber laser 1064 nm on surface roughness and shear bond strength of titanium being used as abutment to resin cement for enhancing crown retention.

2. Material and methods:

Thirty titanium discs of 0.6 cm x 0.3 cm (diameter and thickness respectively) were cut by wire cut lathe machine (Bantam/ Italy) from commercially pure titanium rod grade II (Baoji Jinsheng Metal Material/China) (Śmielak et al., 2015).Titanium discs were grinded and polished using silicon carbide papers in sequence of 120, 320, 500, 800, 1200, 2000 and 2400 grit size to obtain a uniform surface as shown in figure (1), after that the discs were cleaned ultrasonically with ethanol for 15 min then with distilled water for 10 min and left to dry.

Figure (1): Titanium discs were grinded and polished using silicon carbide papers in sequence of 120, 320, 500, 800, 1200, 2000 and 2400 grit size to obtain a uniform surface)

Ytterbium (Yb) Q-switched fiber laser 1064 nm (Wuxi Raycus fiber laser Technologies /RFL-P 100Q, China) was used for surface modification of titanium discs with 81 ns pulse duration, 30,000 Hz repetition rate, 50 μm spot size and 10,000 mm/s scanning speed. The average power was 10 W or 20 W depending on the tested group. Surface modification pattern was in the form of lines with 100 μm hatch distance.

Titanium discs were arranged into three groups in accordance with the variation in average power of fiber laser (n=10) as follows:

1. Control group: with no surface modification.
2. 10 W group: modification with fiber laser (average power 10 W and peak power 4115.2 W).
3. 20 W group: modification with fiber laser (average power 20 W and peak power 8230.4 W).

Following laser irradiation of titanium discs, from each group one disc surface was examined by (SEM) (TESCAN / VEGA 2, Czech) with

magnification of 2000x to examine the surface morphology and to determine that if any cracks or defects are formed following laser treatment.
Average surface roughness (Ra) of titanium discs were examined by surface roughness tester (SRT 6210, China) that illustrated in figure (2) which contained 5 µm radius diamond probe pin oriented vertically to the surface of titanium disc with 0.25 mm cut off distance. The average value in micrometer was determined from three measurements on each surface.

Figure (2): Surface roughness tester.

After that, titanium discs embedded in mold of cold-cure acrylic to depth of 2 mm and about 1 mm from disc height was remained uncovered to guarantee that Ti disc remain intact throughout cementation as shown in figure (3).
For application of resin cement, a customized made silicon mold that shown in figure (4) was constructed with a central circular opening of 5 mm x 3 mm (diameter and depth respectively) to mold the cement over the disc, and this opening surrounded by another wider border of 6 mm x 1 mm (diameter and depth respectively) for encountering the disc to fit the mold over it.

Figure (3): Acrylic molds of titanium discs which embedded to depth of 2 mm and about 1 mm from disc height was remained uncovered to guarantee that Ti disc remain intact throughout cementation.

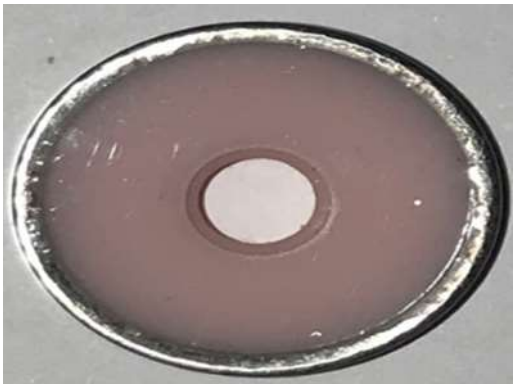

Figure (4): A customized made silicone mold for application of resin cement over the titanium discs.

Cementation procedure that shown in figure (5) was done using resin cement (Breeze self-adhesive resin cement, Pentron/ USA) following manufactures instructions.

Figure (5): Cementation procedure performed by dispensing an equal volume of resin cement through mixing tip and distributed through the mold opening then photopolymerized by light curing device.

An equal volume of resin cement mixed by mixing tip and distributed through the silicon mold opening, then photopolymerization of resin cement done via light curing device for 40 seconds. After silicone mold removing, the discs were kept in a water bath contained distilled water for 24 hours at 37 °C (Ates et al., 2017).
Shear bond strength (SBS) test was performed using universal testing machine (LARYEE/WDW 50, China), the blade-end rod position was perpendicularly to titanium–resin cement interface, and load application performed with 0.5 mm/ min crosshead speed until the occurrence of failure (Cao et al., 2019).
Values of SBS (MPa) were estimated according to this formulation (Murthy, Manoharan, & Livingstone, 2014) :

$$S = \frac{F}{A}$$

Where;
S = Shear bond strength [MPa]
F = Applied force [N]

A = bond area [mm²]

3. Statistical analysis:

Analyzing of data was achieved using SPSS version 24 to analyze the data including descriptive and inferential statistics. ANOVA test was done for detection the significant differences of Ra and SBS between the groups, while Tukey HSD-test performed for detection the significant differences of SBS between every two groups at ($P < 0.05$).

4. Results:

4.1 Scanning electron microscope:

Photographs of SEM of the control and irradiated discs were illustrated in Figure (6). Control specimen appears to be smooth in comparison with test group specimens. The texture of the test group specimens consist of micro retentive grooves and display uniform roughness pattern, deep penetration areas by fiber laser beam without the presence of defects or cracks.

4.2 Surface roughness:

Higher Ra value was observed in (10 W) group followed by (20 W). The control group displayed the lowest Ra value as compared with the other groups Table (1). ANOVA test in table (2) shows a high significant difference for Ra than the control group ($P < 0.05$).

4.3 Shear bond strength:

Results considering SBS test showed that the highest value of SBS mean was obtained at average power of 20 W followed by 10 W while the lowest value SBS mean observed in control group as shown in Table (1). ANOVA test in table (3) shows a high significant difference for SBS than the control group ($P < 0.05$).

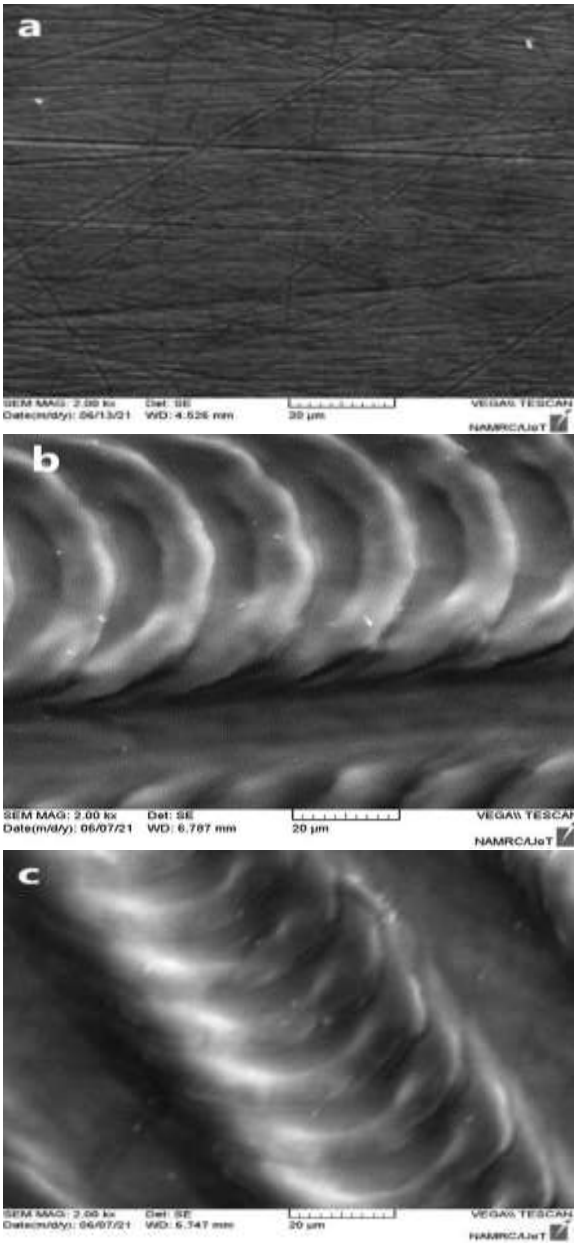

Figure (6): SEM photographs of titanium discs at magnification of 2000x (a) control, (b) 10 W and (c) 20 W.

Tukey HSD test in Table (4) shows that there is a high significant difference between the control group and each of the experimental groups and there is a high significant difference among the laser-irradiated groups.

Table 1: Descriptive statistics of Ra (mean ± SD) and SBS (mean ± SD).

Groups	Ra (µm)	SBS (MPa)
control	0.421±0.030	1.585±0.089
10 W	2.357±0.002	3.896±0.050
20 W	2.292±0.005	5.981±0.058

Table (2): ANOVA Test of Ra Data

	Sum of Squares	Df	Mean square	F	Significance
Between groups	24.162	2	12.081	38057.665	0.000
Within groups	.009	27	.000		
Total	24.171	29			

Table (3): ANOVA Test of SBS Data

	Sum of Squares	Df	Mean square	F	Significance
Between groups	96.727	2	48.363	10466.757	0.000
Within groups	.125	27	.005		
Total	96.852	29			

Table (4): Tukey HSD Test between groups for SBS.

SBS			
Groups		**Mean Difference**	**Significance**
Control	10 W	-2.311	0.000
	20 W	-4.396	0.000
10 W	20 W	-2.085	0.000

5. Discussion:

Retention loss is a common issue with cement-retained implant supported prostheses about 16.8% Chaar et al., 2011), therefore to ensure optimal prosthesis performance, a strong bond between the titanium abutment and cement is required. This study was performed for investigation the effect of different average power values of fiber laser on the surface roughness and SBS of resin cement to titanium. SEM analysis revealed a different in morphology of the surface between control specimen and fiber laser treated specimens that occurred because titanium absorbing laser energy and converting it into thermal energy, resulting in melting and vaporization. Modification of titanium surface with fiber laser enhance Ra that result in increasing the surface

area with no defects or cracks, the surface area is directly proportional with retention which is important to improve bonding of cement to abutment, the findings of this study are in agreement with those of Korkmaz and Aycan 2019, who found that using a fiber laser to treat titanium alloy resulted in an increase in surface roughness without defects or cracks. When compared to the control group, all experimental groups showed greater Ra values, Surface roughness differed between the experimental groups due to differences in the average power of the fiber laser resulting in varying degrees of melting and vaporization. Furthermore, at higher value of average power (20 W) reduction in Ra was noticed because the temperature received by the specimen increased, leading to increase melting and further melt deposition on the surface and this lead to reduction in roughness to particular extent (Xi et al., 2019).

In comparison to the control group, the two laser treated groups had high significant SBS values because the surface area of titanium increases as the Ra increases, and surface roughness produce areas of mechanical interlocking that are advantageous to the cement material, improving bond strength (Elsaka, 2013), This is in conformity with the results of Ates et al. , 2017 study who found that treatment of titanium with fiber laser enhance the roughness of the surface and raised the SBS significantly.

Moreover, in this study it was found that excessive roughness of the surface that obtained from (10 W) group lead to reduction in SBS value as compared with (20 W) group, this leading to actuality that excessive roughness does not increase SBS value because excessive roughness of the surface create intense-stress areas at the interface of cement and titanium wherein severe angled edges contribute to insufficient resin cement flow into the surface's minute roughness, preventing the adhesive from fully bonding to the surface (Fawzy & El-Askary, 2009).This finding is consistent with prior studies that found that increasing roughness of the surface did not increase the bond strength (Elsaka, 2013; Elsaka & Swain, 2013; Seker, et al.,2015).

6. Conclusions:

Irradiation the surface of titanium with Fiber laser lead to increase the surface roughness with no cracks or defects and it has a significant improvement on the SBS between titanium and resin cement.

References:

Ajay, R., Suma, K., Ali, S. A., Sivakumar, J. S. K., Rakshagan, V., Devaki, V., & Divya, K. (2017). *Effect of surface modifications on the retention of cement-retained implant crowns under fatigue loads*: An In vitro study. Journal of pharmacy & bioallied sciences, 9 (Suppl1), S154.

Akin, H., & Guney, U. (2012). *Effect of various surface treatments on the etention properties of titanium to implant estorative cement.* Lasers in medical science, 27(6), 1183-1187.

Ates, S. M., Korkmaz, F. M., Caglar, I. S., Duymus, Z. Y., Turgut, S., & Bagis, E. A. (2017). *The effect of ultrafast fiber laser application on the bond strength of resin cement to titanium.* Lasers in medical science, 32(5), 1121-1129.

Cao, Y., Guo, Y.-y., Chen, L., Han, J., Tong, H., Zhang, B., & Zhang, Y. (2019). *Effects of different surface treatments on bonding strength of resin cement to machined pure titanium.* The journal of adhesive dentistry, 21(5), 401.

Chaar, M., Att, W., & Strub, J. (2011). *Prosthetic outcome of cementretained implant supported fixed dental restorations: a systematic review.* Journal of oral rehabilitation, 38(9), 697-711.

Elsaka, S. E. (2013). *Effect of surface pretreatments on the bonding strength and durability of self-adhesive resin cements to machined titanium.* The Journal of prosthetic dentistry, 109(2), 113-120.

Elsaka, S. E., & Swain, M. V. (2013). *Effect of surface treatments on the adhesion of self-adhesive resin cements to titanium. J* Adhes Dent, 15(1), 65-71.

Fawzy, A. S., & El-Askary, F. S. (2009). *Effect acidic and alkaline/heat treatments on the bond strength of different luting cements to commercially pure titanium*. Journal of Dentistry, 37(4), 255-263.

Iocca, O. (2016). *Evidence-Based Implant Dentistry*: Springer International Publishing.

Kim, H.-K., Park, S.-Y., Son, K., Kim, Y.-G., Yu, W.-J., Lee, K.-B., & Lee, J.-M. (2020). A*lterations in Surface Roughness and Chemical Characteristics of Sandblasted and Acid-Etched Titanium Implants after*

Irradiation with Different Diode Lasers. Applied Sciences, 10(12), 4167.

Kim, J.-T., & Cho, S.-A. (2009). *The effects of laser etching on shear bond strength at the titanium ceramic interface.* The Journal of prosthetic dentistry, 101(2), 101-106.

Marticorena, M., Corti, G., Olmedo, D., Guglielmotti, M., & Duhalde, S. (2007). *Laser surface modification of Ti implants to improve osseointegration.* Paper presented at the Journal of Physics: Conference Series.

Murthy, V., Manoharan, B., & Livingstone, D. (2014). *Effect of four surface treatment methods on the shear bond strength of resin cement to zirconia ceramics-a comparative in vitro study.* Journal of clinical and diagnostic research: JCDR, 8(9), ZC65.

Oktem, B., Kalaycioglu, H., Erdoğan, M., Yavaş, S., Mukhopadhyay, P., Tazebay, U. H., İlday, F. Ö. (2010). *Surface texturing of dental implant surfaces with an ultrafast fiber laser.* Paper presented at the Conference on Lasers and Electro-Optics.

Oshida, Y., Tuna, E. B., Aktören, O., & Gençay, K. (2010). *Dental implant systems.* International journal of molecular sciences, 11(4), 1580-1678.

Riveiro, A., Maçon, A. L., del Val, J., Comesaña, R., & Pou, J. (2018). *Laser surface exturing of polymers for biomedical applications.*Frontiers in physics, 6, 16.

Safi, I. N., Hussein, B. M. A., & Al-Shammari, A. M. (2019). *Testing and characterization of sintered β-tricalcium phosphate coat upon zirconia dental implant using Nd: YAG laser.* Journal of Laser Applications, 31(3), 032002.

Sahu, N., Lakshmi, N., Azhagarasan, N., Agnihotri, Y., Rajan, M., & Hariharan, R. (2014). *Comparison of the effect of implant abutment surface modifications on retention of implant-supported restoration with a polymer based cement.* Journal of clinical and diagnostic research: JCDR, 8(1), 239.

Seker, E., Kilicarslan, M. A., Deniz, S. T., Mumcu, E., & Ozkan, P. (2015). *Effect of atmospheric plasma versus conventional surface treatments on the adhesion capability between self-adhesive resin cement and titanium surface.* The journal of advanced prosthodontics, 7(3), 249-256.

Shafie, H. R. (2014). *Clinical and laboratory manual of dental implant abutments*: John Wiley & Sons.

Śmielak, B., Gołębiowski, M., & Klimek, L. (2015). *The influence of abutment surface treatment and the type of luting cement on shear bond strength between titanium/cement/zirconia*. Advances in Materials Science and Engineering.

Xi, X., Yongzhi, P., Wang, P., & Fu , X. (2019). *Effect of Laser Processing Parameters on Surface Texture of Ti6Al4V Alloy.* IOP Conference Series: Materials Science and Engineering, *563*, 022052. doi:10.1088/1757-899X/563/2/022052

Yeo, I.-S. L. (2020). *Modifications of dental implant surfaces at the micro-and nano-level for enhanced osseointegration.*Materials, 13(1), 89.

تأثير الليزر الليفي على قوة ارتباط دعامة زرعة التيتانيوم بإسمنت الراتنج

ربى حسام عبد الرزاق باسمة محمد علي حسين

معهد الليزر للدراسات العليا، جامعة بغداد/ بغداد – العراق

الخلاصة :الهدف: تعديل سطح التيتانيوم باستخدام الليزر الليفي ذو الطول الموجي 1064 نانومتر لتعزيز قوة الترابط مع اسمنت الراتنج. **المواد والطرق:** تم تصنيف ثلاثين قرصًا من التيتانيوم بحجم 0.6 سم × 0.3 سم (قطر وسمك على التوالي) بعد التحضير إلى ثلاث مجموعات (ن = 10) على النحو التالي: مجموعة التحكم دون أي معالجة سطحية ومجموعتين تمت معالجتهما بألياف الليزر مدة النبضة 81 نانوثانية، التردد 30000 هرتز ، حجم البقعة 50 ميكرومتر وسرعة المسح 10000 مم / ثانية ومتوسط قيم الطاقة مختلفة (10 واط و 20 واط) حسب المجموعة المختبرة. تم إجراء توصيف أقراص التيتانيوم عن طريق مسح المجهر الإلكتروني (SEM) واختبار خشونة السطح. بعد هذه الاختبارات ، تم تطبيق مادة الإسمنت الراتينجية على أقراص التيتانيوم. تم تحديد قيم قوة رابطة القص (SBS) بواسطة آلة اختبار عالمية. تم استخدام اختبارات ANOVA و Tukey HSD لتحليل البيانات ($\alpha = 0.05$). **النتائج:** لوحظ ارتفاع قيمة خشونة السطح في مجموعة (10 واط) تليها مجموعة (20 واط) وأدنى درجة خشونة للسطح كانت في مجموعة التحكم، بالإضافة إلى ذلك تم الحصول على أدنى قيمة SBS من مجموعة التحكم وأعلى قيمة SBS من مجموعة (20 واط) تليها مجموعة (10 واط).**الاستنتاج:** يمكن تعزيز قوة الترابط بين التيتانيوم واسمنت الراتنج بشكل كبير باستخدام الليزر الليفي كعلاج للسطح. يعد متوسط طاقة ألياف الليزر معلمة أساسية في تعزيز خشونة سطح التيتانيوم والالتصاق بإسمنت الراتنج ؛ بالإضافة إلى ذلك ، لوحظ وجود ارتباط سلبي بين خشونة السطح و قوة رابطة القص في المجموعات التجريبية.

Iraqi J. Laser, issue 1, vol., 21, pp. 18-27 (2022)

IRAQI JOURNAL OF LASER

Influence of Er:Cr;YSGG laser Desensitization on SBS of resin cement to dentin

Rusal Mohammed Mubarak[1,*], Basima Mohammed Ali Hussein[1]
Institute of Laser for Postgraduate studies, University of Baghdad, Iraq
*Corresponding author: Rusal Mohammed Mubarak
e-mail: rusal.mohammed1202a@ilps.uobaghdad.eud.iq
basma.moh@ilps.uobabhdad.eud.iq

(Received 31/01/2022; accepted 02/06/2022)

Abstract

Background: Crown preparation of vital teeth involve the removal of a sound tooth structure, and when enamel removed this lead to exposed dentin with an increase in the number of open dentinal tubules also the diameter of dentinal tubules will increase, furthermore lead to increase movement of fluids inside the tubules all that causes post preparation sensitivity. **The aim** of this study is to evaluate the effect of desensitizing by Er:Cr:YSGG laser on shear bond strength of prepared tooth and resin cement. **Materials and methods:** Thirty sound maxillary premolars, grouped into three groups(n=10). Group A is the control group, group B irradiated by Er:Cr:YSGG laser with (0.25 W, 20 Hz, 10%water and air), group C irradiated by Er:Cr:YSGG laser with (0.5 W, 20 Hz, 10% water and air). **Results:** SEM examination showed complete occlusion of opened dentinal tubules after laser irradiation of both groups that irradiated with laser. Statistical analysis showed significant increase in surface roughness in group B and C. SBS was significantly increase in group B with no significant increase in group C. **Conclusion:** Er:Cr:YSGG laser can occlude open dentinal tubules without and adverse effect on the retention of the restoration, on the contrary it increase bonding strength. And this increasing was significant in group B with (0.25W, 20 Hz, 10 % water and air). **suggestion:** so the parameters used in group B (0.25 W, 20Hz, 10 % water and air) is recommended for desensitizing prepared tooth and induce enhancement to the bonding strength of resin to tooth surface.

Introduction

Dentinal hypersensitivity is very common dental issue, characterized by a quick intense pain reaction of exposed dentin anytime it comes into contact with external stimuli, such as thermal, tactile, evaporative, and chemical. When dentin hypersensitivity develops, the patient becomes so irritated that they refuse to eat cold foods or brush the affected tooth. (Arua, Fadare, & Adamu, 2021). Dentin hypersensitivity is defined by the most widely accepted mechanism, which describe by Brännström, he explained it based on the hydrodynamic theory. Dentin hypersensitivity, according to this theory, is caused by fast fluid movement in the dentin tubules as a result of external stimuli. Nerve endings (A- and A-fibers) at the dentin-pulp interface may be activated by stimulus-induced fluid flow; the excited nerve terminations are referred to as mechanoreceptors. Depending on the stimulation, the abrupt migration of dentin fluids may be directed outward or inward. Outward flow is produced by cooling, drying, evaporation, and hypertonic solutions, which causes more discomfort than inward flow caused by heat application. (Brannstrom, 1963). Tubules in the dentin render the tissue porous, especially when the outer protective layer represent by the enamel and cementum is removed. Many dental procedures require the removal of the cementum or enamel layer to reveal the dentin, such as root planning, cavity preparation, and crown preparation. Hypersensitivity of the vital teeth post-cementation due to ingress of luting cement into the opened dentinal tubules this will affect the hydrostatic pressure by moving or displacing equal amount of dentinal fluid inside the tubules (Mausner, Goldstein, & Georgescu, 1996). Several techniques have been tested to date to eliminate such patient discomforts (calcium hydroxide, cavity varnishes, topical fluorides, fluoride iontophoresis, strontium chloride, and potassium nitrate dentifrices) (Sethi & Indurkar, 2015). The majority of therapies have attempted to block exposed dentin tubules, but none have proven to be consistently successful or long-lasting (Romano, Aranha, da Silveira, Baldochi, & de Paula Eduardo, 2011). For the treatment of dentin hypersensitivity, laser therapy was introduced as an alternative. Before crown cementation, desensitizing laser treatment has been found to occlude exposed dentinal tubules and reduce hypersensitivity for longer lengths of time than any other desensitizing agent, and this practice is gaining appeal around the world (Atay, Kara, Kara, Çal, & Usumez, 2017). However, due to the obvious significance in physical and mechanical characteristics of resin cements, the effect of laser desensitizing treatment on crown retention is important (Huang et al., 2020). Er:Cr;YSGG laser which is absorbed by water of the dentin, converting water to steam by heating, then the steam expand and since this reaction is explosive in nature (microexplosion), this microexplosion causing dentin debris to occluded or tightening the dentinal tubules this will prevent emerging of cement to the dentinal tubules and prevent post cementation hypersensitivity (Kumar et al., 2015) . Er:Cr:YSGG aser had been used for treatment of dentinal hypersensitivity successfully , but its effect on surface roughness

or bonding strength is still not clear. So this study aimed to study the effect of tooth desensitization on shear bond strength of resin cement to dentin surface.

Material and Methods

1. Sample collection and preparation

For orthodontic purpose, freshly extracted human maxillary premolars (total 63) with an age average of (16-35) years. These teeth washed in a running water for debris removal. All samples were scaling and root planning, to eliminate any source of infection and to handle with clean samples then preserved in 1% thymole solution. Teeth were molded in an acrylic cylindrical mold up to the cemento-emamel junction.

With the use of a dental surveyor, the teeth were held in the zero plane. The occlusal side of the teeth cut with a diamond disc as shown in figure (1). Then the prepared occlusal side of the samples polished was with non-fluoride pumice for 15 seconds, washed in an ultrasonic cleaner for 15 min.

Finally, teeth were divided randomly into three groups; group A, which is the control group. Groups B, and C, both treated by laser.

2. Laser application

Er:Cr;YSGG 2780 nm Dental laser (WaterLase iPlus .USA) was used to irradiate groups B and C . Standardized irradiation was performed with the use of CNC machine, with scanning speed 10 mm/sec figure (2).

Figure (1) Teeth preparation set-up with the dental surveyor, diamond disc for cutting.

- Group (A) is the control group.
- Group (B) Er: Cr; YSGG laser with (0.25 W, 20 Hz, 10% water and air.
- Group (C) Er: Cr; YSGG Laser with (0.5 W, 20 Hz, 10% water and air.

After many trials to determine the most suitable parameters that induced morphological changes to dentin surface without any carbonization or cracks two parameters selected. Laser light was delivered perpendicular to prepared occlusal surface of the tooth in non-contact mode (2mm away from the tooth surface). For group B laser parameters were (0.25 W, 20 Hz, 10% water and air), while in group C (0.5 W, 20Hz, 10% water and air).

3. SEM Examination

The effect of the laser on dentinal tubules was assessed using a scanning electronic microscope (SEM) (INSPECT F50, USA).

Figure (2) A) Er:Cr;YSGG laser, B) CNC machine.

4. Measurement of Temperature

The temperature rise during laser application was measured using a thermometer on 5 samples from each of the laser-treated groups (Groups B and C) (Amprobe TMD-56). The teeth were prepared with a Sx pro-taper file to provide a passage for the thermocouple wire (with a temperature range of (-200°C to 1372°C) and a head diameter of 0.8 mm) to be inserted from the apical opening of the root to the roof of the pulp chamber, and then fixed with thermal paste. The samples were placed in a water bath at 37°C for testing, with only the root immersed in the water.

5. Roughness Assessment

Roughness was evaluated before and after laser therapy on all samples using a profilemeter (surface roughness tester SRT-6210, China). Surface roughness for each sample was the mean of three reading was determined at three different places on the dentin surface.

6. Cementation of Zirconia disc

The first stage is to make 3 mm diameter (which represent the bonding area) and 5 mm height zirconia cylinders (KATANATM Zirconia, Ht, Japan). They were made using CAD/CAM technology. Cleaned with ultrasonic cleaner before use. Self-adhesive resin cement (Breeze, Pentron Clinical, CA92867, USA) was used for cementation; it was auto-mixed with disposable mixing tips included in the cement kit and applied directly to the tooth surface. To ensure appropriate light curing, a silicon mold was constructed with a central hole of 3 mm in diameter and a 3 mm height split from the internal surface into 1 mm for cement and 2 mm for the zirconia disc. A weight of 2 Kg was employed during the cement setting with the use of a dental surveyor (Beuer, Schweiger, & Edelhoff, 2008) to avoid any air bubbles and ensure adequate cementation. The load was removed after 4 minutes of curing. To ensure full curing, the samples were left on the table for one hour. After that, the cemented samples were placed in a water bath at 37°C for 24 hours before being tested for Shear Bond Strength.

7. Shear Bond Strength measurement

Universal testing machine (ARYEE, WDW-50, 50 KN. China). was used to measure the shear bond strength. The tooth was positioned horizontally, and a stainless steel chiseled-shaped blade was used to cut through the tooth-resin cement contact until total separation was achieved.

8. Results

The results of the laser effect on dentinal tubules, temperature, roughness measurements, and shear bond strength examination. Statistical analysis using descriptive statistics, Paired T test, Independent samples t-test, and one-way ANOVA using (SPSS 24), are lasted below.

8.1. Temperature Measurement

In table (1) mean of temperature rise during laser application was maintained. The maximum rise in temperature in group B (Er:Cr;YSGG irradiation with 0.25 W, 20 Hz, 10% water and air) was 1.1. While in group C (Er:Cr;YSGG irradiation with 0.5 W, 20 Hz, 10% water and air) was 1.4.

Table (1) Mean and Standard Deviation of temperature change.

Groups	Mean	Standard deviation (SD)
Group B	0.9	0.158
Group C	1.24	0.114

8.2. SEM Evaluation

Examination of dentin surface was done by Scanning Electronic Microscope (SEM) (INSPECT F50, USA) as in figure (3) SEM evaluation showed open dentinal tubules in group A, which is the control group.

SEM of group B laser treated dentin shows complete occlusion of dentinal tubules, with no sign of carbonization or cracks, as shown in figure (4)

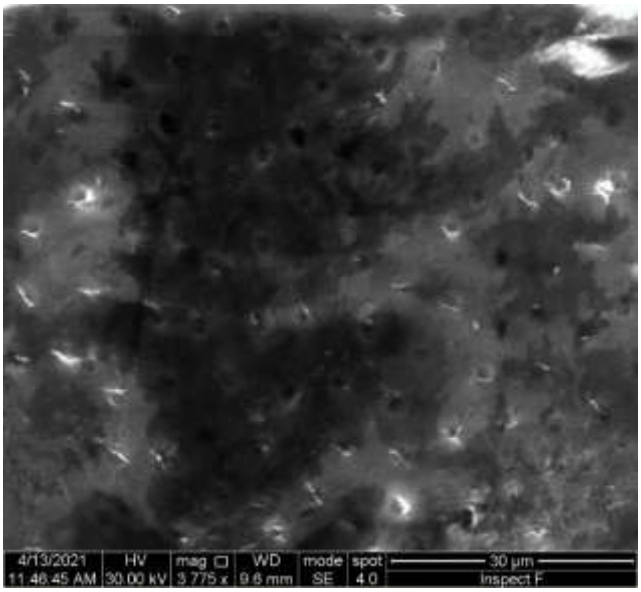

Figure (3) SEM evaluation of group A with open dentinal tubules

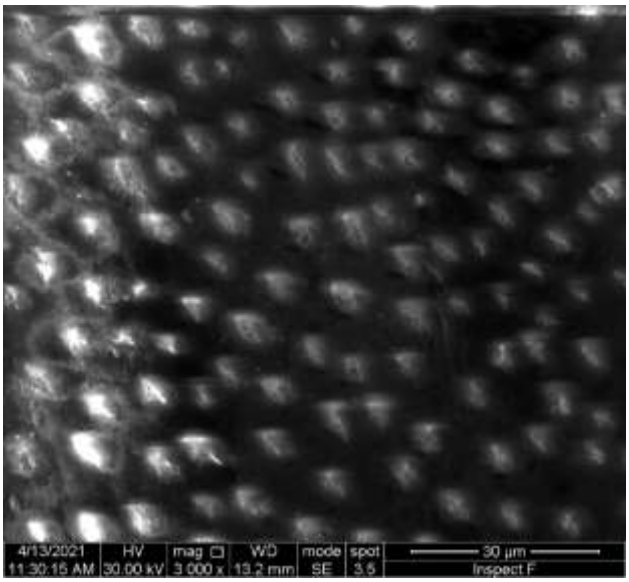

Figure (4) SEM image of group B

In group C laser treated with 0.5 W shows also complete occlusion of dentinal tubules as in figure (5)

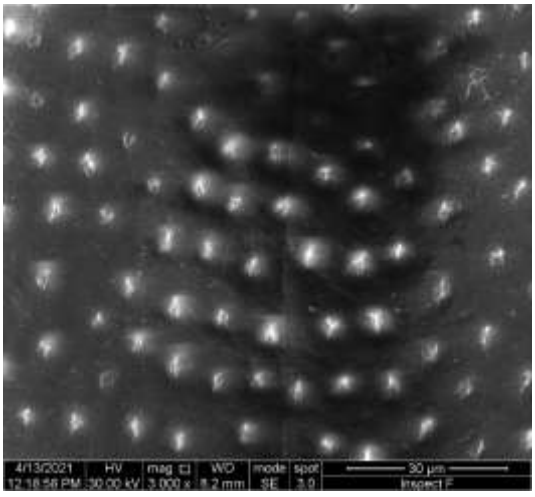

Figure (5) SEM Image of group C

Descriptive statistical analysis of each laser treated groups, before and after laser treatment. With higher increase in roughness in group B after laser irradiation. Statistical analysis using Paired T test, to determine significance in difference in roughness before and after laser irradiation, as maintained in table (2). The result showed that both groups have significant difference in roughness

8.3. Roughness assessment

Table (2) Descriptive statistical analysis, along with Paired T test of Roughness changes

Groups		Before	After
	Effect size	10.916 large	
Group B 0.25 W-ER:CR:YSGG Laser	Minimum	0.632	1.608
	Maximum	0.905	1.930
	Mean	0.765	1.768
	SD	0.088	0.095
	SE	0.028	0.030
	% of change	131.111	
	Paired T test	38.972	
	P value	0.00000 Sig.	
	Effect size	12.324 large	
Group C 0.5 W-ER:CR:YSGG Laser	Minimum	0.769	0.879
	Maximum	0.932	1.127
	Mean	0.827	0.974
	SD	0.055	0.071
	SE	0.017	0.023
	% of change	17.7751	
	Paired T test	6.233	
	P value	0.00015 Sig.	
	Effect size	1.971 large	

3.4. Shear Bond Strength (SBS)

Descriptive statistical analysis of SBS of all groups shown in table (3). The results showed higher mean of bond strength in group B than other groups. And the lowest mean of bonding strength in the control group.

Table (3) The Mean, and Standard Deviation of all groups for SBS in (MPa).

Groups	Mean	±SD	±SE	Minimum	Maximum
Group A (Control Group)	13.1990	1.08611	.34346	12.03	14.80
Group B 0.25 W-ER:CR:YSGG Laser	16.3300	2.18177	.68994	12.70	19.80
Group C 0.5 W-ER:CR:YSGG Laser	13.9800	1.46652	.46375	11.30	16.40

To determine difference between all the groups One-way ANOVA test was performed. The results showed significant difference between all groups as shown in table (4).

Table (4) One-way ANOVA test

ANOVA					
	Sum of Squares	df	Mean Square	F	P value
Between Groups	53.119	2	26.559	9.848	0.001 Sig.
Within Groups	72.814	27	2.697		
Total	125.932	29			

Statistical analysis using Tukey HSD, to determined significance in SBS in all groups, as showed in table (5). Results showed that bond strength in group B is significantly higher than group C and group A which is the control group. While group C is not significantly higher than the control group.

Table (3-5): Tukey HSD test of shear bond strength of all groups.

Dependent Variable: SBS				
Tukey HSD				
(I) Groups	(J) Groups	Mean Difference (I-J)	p value	
Group A (Control group)	Group B	-3.13100-*	.001	Sig.
	Group C	-.78100-	.544	NS.
Group B (0.25 W-ER:CR:YSGG Laser)	Group A	3.13100*	.001	Sig.
	Group C	2.35000*	0.009	Sig.
Group C 0.5 W-ER:CR:YSGG Laser	Group A	.78100	0.544	NS
	Group B	-2.35000-*	.009	Sig

9. Discussion

Crown preparation is an invasive treatment method necessitated the removal of tooth structure, sound tooth structure, to function as an abutment for the bridge's attachment. When tooth structure is removed, open dentinal tubules result, that are susceptible to hypersensitivity (Pilo, Harel, Nissan, & Levartovsky, 2016). The best treatment for this post-operative complication is occluding dentinal tubules without impacting prosthesis retention(Ayer, 2018). In this study two parameters used for treatment of dentinal hypersensitivity, group B (0.25 W, 20 Hz, 10% water and air), and group C (0.5 W, 20 Hz, 10% water and air). Both of the experimental groups as showed by the SEM examination, the result was also complete occluding of dentinal tubules. with no carbonization or cracks. Another trial was done by Klabd et al., and used Er:Cr:YSGG for treatment of dentinal hypersensitivity and get complete occluding of dentinal tubules, which support the results obtained from this study (Habdan, Awdah, Meshari, Mokeem, & Saqat, 2017). The closure of dentinal tubules as seen in the SEM images, could be explained by the action of Er: Cr: YSGG Laser, which interacts with dentin, absorbed by water of the dentin, converting water to steam by heating, then the steam expand and since this reaction is explosive in nature (microexplosion), this microexplosion causing dentin debris to occluded or tightening the dentinal tubules (Stübinger, Klämpfl, Schmidt, & Zeilhofer, 2020). The advantage of this phenomes is preventing environmental factors effecting dentinal tubules, as well as prevent emerging of cement to the dentinal tubules and prevent post cementation hypersensitivity(Abdollahi & Jalalian, 2019). The influence of the laser on temperature indicated that, it was below the proposed temperature rise which cause pulpal necrosis (5.6) (van Gemert & Niemz, 2013) in both experimental groups. That's mean that

laser effect on the dentinal tubules was superficial and heat was not to the pulp, supporting the safety of this technique in the treatment of dentinal hypersensitivity due to tooth preparation. This minimum thermal effect of these parameters due to pulse duration is very short, and shorten the heat generation time that gives the tissue enough time to cool down (Convissar, 2015). Also the use of 10% water and air helped effectively in cooling during laser application. Laser radiation to dentin induced significant increase in roughness in in both lasers treated groups (B, and C). This refers to the Er:Cr:YSGG laser interaction with water and hydroxyapatite of the dentin, that interaction is explosive in nature, induce debris that produced from lasing process, to accumulate on the dentin surface, and produces a roughened surface. As noticed from the obtained results that group B with lower energy induce higher roughness, and this refer to melting produced by group C laser treated with 0.5 W. As Er: Cr: YSGG laser induce melting to peritubular dentin (Gholami, Fekrazad, Esmaiel-Nejad, & Kalhori, 2011). An increase in roughness of dentin will improve bonding of adhesive materials to dentin by increasing shear bond strength (Hossain et al., 2001). SBS was significantly higher in group B than group C. this may attributed to higher roughness obtained from Group B than group C. A study found marginal increase in SBS of resin cement to dentin that desensitized with 0.5 W (Kumar et al., 2015).

10. Conclusion

According to the result we can concludes the following:

1.Er:Cr;YSGG laser is an effective treatment approach for dentinal hypersensitivity with complete occluding of dentinal tubules without any side effects like carbonization, cracks, or inducing damage to the pulp tissue.

2. An increase in dentin surface roughness due to laser irradiation induces an increase in shear bond strength to resin cement.

References

Abdollahi, A., & Jalalian, E. (2019). *Effectiveness of two desensitizer materials, potassium nitrate and fluoride varnish in relieving hypersensitivity after crown preparation*. The journal of contemporary dental practice, 20(4), 489-493.

Arua, S. O., Fadare, S. A., & Adamu, V. (2021). *The etiology and management of dentinal hypersensitivity*. Orapuh Journal, 2(2), e815-e815.

Atay, A., Kara, O., Kara, H. B., Çal, E., & Usumez, A. (2017). *Influence of desensitizing procedures on adhesion of resin cements to dentin.* Journal of adhesion science and Technology, 31(9), 1007-1016.

Ayer, A. (2018). *Study on Effect of Remaining Dentin Thickness and Coronal Pulp Size on Dentin Hypersensitivity Following Tooth Preparation.* Journal of College of Medical Sciences-Nepal, 14(1), 1-6.

Beuer, F., Schweiger, J., & Edelhoff, D. (2008). *Digital dentistry: an overview of recent developments for CAD/CAM generated restorations*. British dental journal, 204(9), 505-511.

Brannstrom, M. (1963). *A hydrodynamic mechanism in the transmission of pain-producing stimuli through the dentine. Sensory mechanisms in dentine, 73-79*.

Convissar, R. A. (2015). *Principles and Practice of Laser Dentistry* - E-Book: Elsevier Health Sciences.

Gholami, G. A., Fekrazad, R., Esmaiel-Nejad, A., & Kalhori, K. A. (2011). *An evaluation of the occluding effects of Er; Cr: YSGG, Nd: YAG, CO2 and diode lasers on dentinal tubules: a scanning electron microscope in vitro study*. Photomedicine and laser surgery, 29(2), 115-121.

Habdan, A., Awdah, A., Meshari ,A., Mokeem, L., & Saqat, R. (2017). *The effectiveness of*

Er. Cr. Ysgg laser in sustained dentinal tubules occlusion using scanning electron microscopy. J Dent Health Oral Disord Ther, 7(6), 00261.

Hossain, M., Nakamura, Y., Yamada, Y., Suzuki, N., Murakami, Y., & Matsumoto, K. (2001). *Analysis of surface roughness of enamel and dentin after Er, Cr: YSGG laser irradiation*. Journal of clinical laser medicine & surgery, 19(6), 297-303.

Kumar, S., Rupesh, P., Daokar, S. G., Kalekar, A., Ghunawat, D. B., & Siddiqui, S. (2015). *Effect of desensitising laser treatment on the bond strength of full metal crowns: an in vitro comparative study*. Journal of international oral health: JIOH, 7(7), 36.

Mausner, I. K., Goldstein, G. R., & Georgescu, M. (1996). *Effect of two dentinal desensitizing agents on retention of complete cast coping using four cements.* The Journal of prosthetic dentistry, 75(2), 129-134.

Pilo, R., Harel, N., Nissan, J., & Levartovsky, S. (2016). *The retentive strength of cemented zirconium oxide crowns after dentin pretreatment with desensitizing paste containing 8% arginine and calcium carbonate*. International journal of molecular sciences, 17(4), 426.

Romano, A. C. C. C., Aranha, A. C. C., da Silveira, B. L., Baldochi, S. L., & de Paula Eduardo, C. (2011). *Evaluation of carbon dioxide laser irradiation associated with calcium hydroxide in the treatment of dentinal hypersensitivity. A preliminary study.* Lasers in medical science, 26(1), 35-42.

Sethi, R., & Indurkar, M. S. (2015). *Comparison of Fluoride Iontophoresis and Dentin Bonding Agent Application in the Treatment of Dentin Hypersensitivity: A clinical study*. Indian J Dent Adv, 7(1), 13-17.

Stübinger, S., Klämpfl, F., Schmidt, M., & Zeilhofer, H. F. (2020). *Lasers in Oral and Maxillofacial Surgery*: Springer International Publishing.

van Gemert, M., & Niemz, M. (2013). *Laser-Tissue Interactions: Fundamentals and Applications*: Springer Berlin Heidelberg.

تأثير ازاله تحسس السنان بليزر الاربيوم كروميوم على قوه رابطه القص بين عاج السن والسمنت الراتنجي

رسل محمد مبارك * ، باسمه محمد علي

معهد الليزر للدراسات العليا / جامعة بغداد

الخلاصة: يتضمن إعداد تاج الأسنان الحيوية إزالة جزء من بنية الأسنان السليمة، وعندما تتم إزالة المينا يؤدي ذلك إلى ان يكون عاج الاسنان مكشوف مع زيادة في عدد أنابيب الأسنان المفتوحة أيضا سيزداد قطر أنابيب الأسنان، مما يؤدي إلى زيادة حركة السوائل داخل الأنابيب كل ذلك يسبب حساسية ما بعد التحضير.الهدف من هذه الدراسة هو تقييم تأثير إزالة الحساسية بواسطة ليزرالاربيوم كروميوم على قوة رابطة القص للأسنان الجاهزة والاسمنت الراتنجي. تم تحضير ثلاثون سن من اسنان الفك العلوي, وتقسيمها الى ثلاث مجاميع. المجموعه أ هي المجموعه الضابطه والمجموعه ب مشعه بليزر الاربيوم كروميوم بقوه 0.25 واط، 20 هرتز، 10% ماء وهواء. المجموعه ج كذلك مشعه بليزر اربيوم كروميوم بقوه 0.5 واط, 20 هرتز، 10% ماء وهواء. اظهر فحص المايكروسكوب الماسح الالكتروني انسداد تام في انابيب الاسنان المفتوحه بعد التشعيع بالليزر لكلا المجموعتين. اظهر التحليل الاحصائي زياده كبيره في خشونه السطح في المجموعتين ب وج. وكانت الزياد في قوه رابطه القص للمجموعه ب كبيره وملحوظه وكانت الزياده غير ملحوظه في المجموعه ج . نستنتج من ذلك ان ليزر الاربيوم كروميوم يقوم بغلق انابيب الاسنان المفتوحه ولايؤثر ذلك على قوه الربط بين الاسنان ومواد الحشوات بل على العكس فالمجموعه ب تظهر زياده ملحوظه في الترابط ويمكن العمل بها بعد تحضير الاسنان لتلافي الاصابه بتحسس الاسنان

Iraqi J. Laser, issue 1, vol., 21, pp. 28-33 (2022)

IRAQI JOURNAL OF LASER

Treatment of intraoral pyogenic granuloma with diode laser 810-980 nm

Aya A. Majeed [1*], Tahrir N. Aldelaimi [2]

*Corresponding Author email: aya.abd1202a@ilps.uobaghdad.edu.iq

tahrir.aldelaimi@uoanbar.edu.iq

1. Postgraduate candidate, Department of Biomedical Application, Laser Institute for Postgraduate Studies, University of Baghdad.

2. Department of Maxillofacial Surgery, College of Dentistry, University of Anbar.

(Received 31/01/2022; accepted 22/06/2022)

Abstract

Background: Pyogenic granuloma is a hyperplastic benign tumor. The most common intra-oral site is marginal gingiva. It is often occurred in the second decade of life, it has a strong tendency to recur after simple excision.

The aim of study: to evaluate the therapeutic advantages of diode laser (810-980 nm) in intraoral Pyogenic granuloma management.

Materials and method: A total of 28 patients (14 men and 14 females) were enrolled in this study and had their pyogenic granuloma surgically removed using a diode laser. All of the patients were given local anesthetic and went through the identical surgical procedure (cartridge containing 1 percent lidocaine with epinephrine 1:100.000). To achieve hemostasis and minimize bleeding, the lesions were completely eliminated by sweeping the laser fiber tip across the operated site. To allow the wounds to heal, they were not sutured. Then, the specimens sent for histopathology.

Results & Conclusions: In the present study, we noticed that the scale of pain, bleeding and oedema gradually decreased during the first two visits. the measured parameters were completely disappeared after two weeks in most cases as well as the patient satisfaction and function also improved. the Patients were recalled after two weeks, the wounds had completely healed and patients were not complaining any type of discomfort. it is generally believed that poor oral hygiene and poor fitting denture may lead to recurrence. According to obtained results; removal of pyogenic granuloma with diode laser (810-980 nm) is successful, effective and reasonable alternative to conventional scalpel technique.

Keywords: pyogenic granuloma, benign hyperplasia, laser institution, laser surgery, diode laser.

1. Introduction

Pyogenic granuloma is a hemorrhagic mass that occurs mostly on the gingiva (it can occur on any surface) in response to various stimuli. It arises as a result of connective tissue fibrovascular growth (Jensen&Barr,1997). It appears clinically as painless red papules on a sessile or pedunculated base. The size of lesion varies in diameter from a few millimeters to few centimeters (Rai et al., 2011) (Al-Mohaya & Al-Malik,2016). The color of the tumor may differ according to the level of vascularity (Rai et al., 2011). The lesion might be pink, red, or purple in hue. Pyogenic granulomas in their early stages feature increased

vascularity and hyperplastic granulation tissue, but mature PGs have more collagen. To prevent recurrence, the traumatic factors must be reduced (Al-Mohaya & Al-Malik, 2016).

Pyogenic Granulomas were found to occupy 44.4 percent to 83 percent of the oral cavity gum. It has also been found to occur in the buccal, lingual, and palatal mucosa (Eversole, 2001) (Neville et al., 2015). It can be occurred everywhere on the human body, including the nose, lips, fingers, and toes. Pyogenic granuloma can occur at any age; however, it is more common in people between the ages of 10 and 40. It is more common in young adult females in their second decade of life. The vascular impact of female sex hormones could be one of the causes**. (**Esmeili et al., 2005**)** (Adusumilli et al., 2014) (Asnaashari et al., 2014). This study aimed to assess the therapeutic benefits of diode laser (810-980 nm) in the management of pyogenic granuloma.

2. Material and methods

A total of 28 patients (14 men and 14 females) were enrolled in this study and had their pyogenic granuloma surgically removed using the diode laser (810-980 nm).

All the patients complained from the same features which involved intraoral painless red, sessile, or pedunculated smooth surfaced mass that can easily bleed on simple probing; It have been reported that the size of lesions range from 0.5cm to 1.5 cm. The patient consent form was obtained before the surgical operation and the detailing of procedure was elucidated to all patient. Demographical information which include patients age, gender, medical history & clinical examination of the tumor. Preoperative intraoral antisepsis using listerine mouth rinse for roughly 30 seconds was used as part of the treatment plan, and all patients and surgical teams were required to wear safety protective eye glasses. Diode laser 810-980nm, 0.8W power according to the recommended procedure, continuous wave mode (CW) with fiber optic delivery system was used to properly remove the lesions in one piece.

All of the patients received the same surgical technique, and they were all given local anesthetic (cartridge containing 1 percent lidocaine with epinephrine 1:100.000). The lesions were carefully removed by passing the laser fiber tip across the surgical site to achieve coagulation and prevent bleeding. The wounds were not sutured to allow them to heal. After that, the biopsy was preserved in a 10% formaldehyde solution for histological examination. Ciprofloxacin Tab 250mg, Metronidazol Tab 500mg to avoid anaerobic bacterial infection of the exposed tissue, Mefanamic acid Cap. 250 mg were utilized as analgesic drugs as well as listerine mouth wash as treatment regimen, as approved by clinical trial or clinical publication.

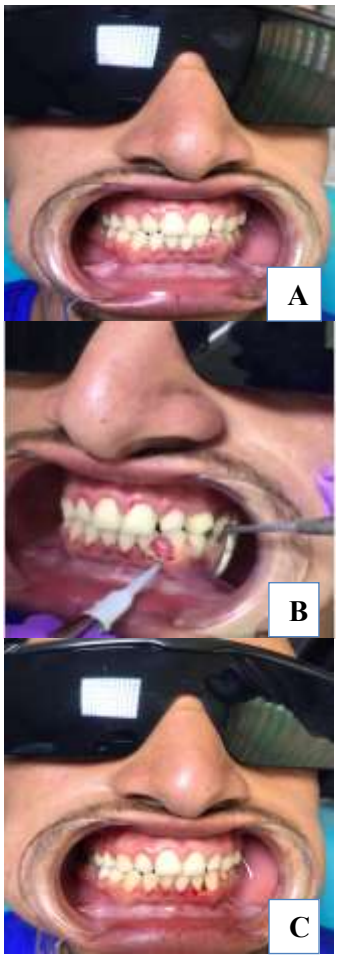

Figure 1: A. Preoperative view B. Application of diode laser C. Postoperative view.

3. Statistical analysis

Data were introduced into SPSS V26 statistical program, tables and graphs were used to present descriptive statistics. While Friedman test was used to measure the improvement in the study dependent

parameters, (Friedman test was used instead of repeated measure ANOVA because the date was not normally distributed) P value< 0.05 was considered as cut-off point of significance.

4. Results

A total of 28 patients (14 females & 14 males) had been enrolled in this study undergone laser excision of pyogenic granuloma by diode laser (810-980nm) aged from 10-45years old. The results of this cross-sectional study show that 28 cases were involved 35.7% of them were in adolescent age while 64.3% were in adult age group, 50% of studied patients were males. Regarding educational level 28.6%, 21.4% and 50% respectively, achieved primary, secondary and university level of education and 35.7% got the disease before less than 3 months.

Table 1: distribution of studied cases according to essential characteristics

		Count	Column N %
Age	<18 year	10	35.7%
	=>18 years	18	64.3%
Gender	Male	14	50.0%
	Female	14	50.0%
Education	Primary	8	28.6%
	Secondary	6	21.4%
	University	14	50.0%
Duration	<3 month	10	35.7%
	=>3month	18	64.3%

Table 2 shows that the level of pain, swelling & bleeding were significantly decreased in median and mean ranks of pain, swelling & bleeding, according to Freidman test, p value ≤ 0.05 in all conditions. Patient satisfaction and function level were found to be steady and significantly increased across different stages of study. P value <0.01 in both conditions.

Table 2: Friedman Test shows differences in pain, swelling, bleeding, patient's satisfaction across different stages of study

		Median	IQR	Mean rank	P VALUE
Pain	1ST	1.00	0.25	3.00	0.001
	2ND	.00	.00	1.57	
	3RD	.00	.00	1.43	
Edema	1ST	1.00	0.25	3.00	0.001
	2ND	.00	.00	1.57	
	3RD	.00	.00	1.43	
Bleeding	1ST	.00	.25	2.21	0.05
	2ND	.00	.00	1.89	
	3RD	.00	.00	1.89	
Satisfaction	1ST	1.00	0.25	1.21	0.001
	2ND	2.00	1	1.96	
	3RD	2.00	1	2.82	
Function	1ST	1.00	1.25	1.18	0.001
	2ND	2.00	1	2.04	
	3RD	2.00	0.25	2.79	

Table 3 shows that Recurrence was noticed in second case when pain, bleeding & swelling were noticed at time of 4th follow up visit, after it has been disappeared at second and third visit just like other 27 patients' lesions, this case was 45 years female employed patient who had primary level of education and she was put poorly fitted denture with multiple manipulation and fitting trials.

5. Discussion

Oral pyogenic granuloma can appear in any decade of a person's life. The majority of the cases were described as a painless mass (Al-Khateeb & Ababneh,2003) (Jafarzadeh et al.,2006) with an ulcerated surface and pedunculated base. in our study, pain, bleeding & swelling completely disappeared in most cases at 2nd visit as well as patient's satisfaction and function also improved at 2nd vis this agree with Roy et al who made it clear that the Patients were recalled after 2 weeks, the lesion had completely healed and patients were not complaining any kind of discomfort (Gupta & Tripathi, 2020).

Table 3: distribution of studied patients according to scores of measured variables according to time of measurements of each patient

	Pain				Edema				Bleeding				Satisfaction				Function			
	R 1	R2	R3	R 4	R1	R2	R3	R 4	R1	R2	R3	R 4	R1	R2	R3	R 4	R1	R2	R3	R 4
1	1	0	0	0	1	0	0	0	0	0	0	0	2	2	3	3	2	2	3	3
2	2	0	0	1	2	0	0	0	1	0	0	1	1	2	2	0	1	2	2	0
3	1	0	0	0	1	0	0	0	0	0	0	0	2	2	3	3	2	2	3	3
4	1	0	0	0	1	0	0	0	0	0	0	0	1	2	3	3	1	2	3	3
5	2	1	0	0	2	1	0	0	1	0	0	0	1	1	2	2	0	1	2	2
6	2	1	0	0	2	1	0	0	1	0	0	0	1	1	2	2	0	1	2	2
7	1	0	0	0	1	0	0	0	0	0	0	0	1	2	2	3	1	2	2	3
8	1	0	0	0	1	0	0	0	0	0	0	0	2	2	3	3	1	2	2	3
9	1	0	0	0	1	0	0	0	0	0	0	0	1	2	2	3	2	1	2	3
10	1	0	0	0	1	0	0	0	0	0	0	0	1	1	2	3	0	1	2	3
11	1	0	0	0	1	0	0	0	0	0	0	0	0	1	2	3	0	1	2	3
12	1	0	0	0	1	0	0	0	0	0	0	0	1	2	2	3	1	2	2	3
13	1	0	0	0	1	0	0	0	0	0	0	0	1	2	2	3	1	2	2	3
14	2	1	0	0	2	1	0	0	1	0	0	0	1	1	2	2	0	1	2	2
15	1	0	0	0	1	0	0	0	0	0	0	0	1	2	2	3	1	2	2	3
16	1	0	0	0	1	0	0	0	0	0	0	0	2	2	3	3	1	2	2	3
17	1	0	0	0	1	0	0	0	0	0	0	0	1	2	2	3	2	1	2	3
18	1	0	0	0	1	0	0	0	0	0	0	0	1	1	2	3	0	1	2	3
19	1	0	0	0	1	0	0	0	0	0	0	0	0	1	2	3	0	1	2	3
20	1	0	0	0	1	0	0	0	0	0	0	0	1	2	2	3	1	2	2	3
21	1	0	0	0	1	0	0	0	0	0	0	0	1	2	2	3	1	2	2	3
22	1	0	0	0	1	0	0	0	0	0	0	0	1	2	3	4	2	2	3	3
23	1	0	0	0	1	0	0	0	0	0	0	0	2	2	3	3	2	2	3	3
24	1	0	0	0	1	0	0	0	0	0	0	0	1	2	3	3	1	2	3	3
25	2	1	0	0	2	1	0	0	1	0	0	0	1	1	2	2	0	1	2	2
26	1	0	0	0	1	0	0	0	0	0	0	0	1	2	3	3	1	2	3	3
27	2	1	0	0	2	1	0	0	1	0	0	0	1	1	2	2	0	1	2	2
28	1	0	0	0	1	0	0	0	0	0	0	0	0	1	2	3	0	1	2	3

R1=3 days post op, R2= 1 week postop, R3=2 week postop.,R4=4 week postop.

One case only undergo recurrence due to poor oral care and poor fitting partial denture.

Oral pyogenic granuloma with Short duration much more easily bleed due to less collagen fibers as well as high vascularity; in contrast the older one has more collagen and less vascularity (Gordon et al., 2010) (Debadutta, 2020). The socioeconomic status & oral hygiene practice for the patient play an important role in the growth of the tumor. In our investigation, the tumors of oral pyogenic granuloma varied in size from (0.5 – 2.5) cm in diameter. Simple surgical excision of the oral pyogenic granuloma with a diode laser 810-980 nm bonded to the lesion base, including about approximately (2 mm) of the surrounding healthy tissue. In order to avoid recurrence, it is critical to follow up on treated patients. Because recurrence was caused by insufficient lesion removal as well as the persistence of causative variables (Kamran et al., 2006) (Ujwala et al., 2018) (Wasan et al., 2020). 2 mm of the surrounding normal healthy tissue was ablated after removing the irritating factors (i.e. low-grade trauma, poor oral hygiene, overhanging restoration & prolonged local irritation) in order to have a good prognosis.

Histopathological analysis of the excised oral pyogenic granulomas revealed inflammatory cells and macrophages infiltrating the vascular granulation tissue , i.e distinguished vascular growth suggesting angiogenesis of a strong performance which may develop with any age but are mostly seen in adolescents and young adults (Papageorge & Doku, 1992) (Kamran et al., 2006) (Marla et al., 2016) (Rossa et al., 2017) (Rugma et al., 2020).This study showed no radiographical sign of bone resorption associated with tumor growth.

References

Adusumilli, S., Yalamanchili, P. S., & Manthena, S. *Pyogenic granuloma near the midline of the oral cavity: A series of case reports*. Journal of

indian society of periodontology, 2014; 18(2), 236.

Al-Khateeb T, Ababneh K *Oral pyogenic granuloma in Jordanians: a retrospective analysis of 108 cases.J Oral Maxillofac Surg* 2003; 61, 1285-1288.

Al-Mohaya MA, Al-Malik AM. *Excision of oral pyogenic granuloma in a diabetic patient with 940nm diode laser*. Saudi Med J 2016; 37:1395-400.

Asnaashari, M., Bigom-Taheri, J., Mehdipoor, M., Bakhshi, M., & Azari-Marhabi, S. *Posthaste outgrow of lip pyogenic granuloma after diode laser removal.* Journal of lasers in medical sciences, 2014; 5(2), 92.

Debadutta Sahu. *Oral pyogenic granuloma: a clinicopathological analysis of thirty-five cases. indian journal of research* | Volume-9 | Issue-1 January - 2020 | PRINT ISSN No. 2250 - 1991 DOI: 0.36106 /paripex.

Esmeili, T., Lozada-Nur, F., & Epstein, J. *Common benign oral soft tissue masses.* Dental Clinics of North America, 2005; 49(1), 223-40.

Eversole, L. R. Clinical outline of oral pathology: diagnosis and treatment. PMPH -USA, 2001.

Gordon- Nunez MA, de Vasconcelos Carvalho M, Benevenuto TG, Lopes MF, Silva LM, Galvao HC. *Oral pyogenic granuloma; a retrospective analysis of 293 cases in a Brazillian population.* J Oral & Maxillofac Surg. 2010, 68:9.

Gupta TR. R, and Tripathi, A.K.: *Management of Pyogenic Granuloma in pregnancy with Diode laser: a case report,* 2020.

Jafarzadeh H, Sanatkhani M, Mohtasham N. *Oral pyogenic granuloma: A review. J Oral S*ci 2006; 48:167-75.

Jensen JL, Barr RJ. Lesions of the facial skin. *Differential diagnosis of Oral an Maxillofacial Lesions,* 5th edn. St Louis, MO: Mosby Books, 1997: 549– 550.

Kamran Ali, Muhammad Rafique Chatha, Navid Rashid, Mahwish Raja, *Pyogenic Granuloma - Review*; Pakistan Oral & Dent. Jr. 26 (1) June 2006; p 59-62.

Marla V, Shrestha A, Goel K, Shrestha S. *The Histopathological spectrum of pyogenic granuloma*: A Case Series. Case Rep Dent. 2016;2016:ID1323798, 6p.

Neville, B. W., Damm, D. D., Allen, C. M., & Chi, A. C. *Oral and maxillofacial pathology.* Elsevier Health Sciences, 2015;483.

Papageorge MB, Doku HC. *An exaggerated response of intraoral pyogenic granuloma during puberty. J* Clin Pediatr Dent. 1992 Spring;16(3):213-6.

Rai S, Kaur M, Bhatnagar P. Laser: *A powerful tool for treatment of pyogenic granuloma. J.* Cutan Aesthet Surg 2011; 4:144-7.

Rossa C, Cartagena A, Torre A. *Oral pyogenic granuloma diagnosis and treatment:* A series of cases. Rev Odontol Mex 2017; 21:244-52.

Rugma U M, Amit K W, Uthappa K B, Sajeesh R, Anjali K. *Laser excision of pyogenic granuloma: a case report; international journal of scientific research*; Volume-9 Issue-1 |January-2020| PRINT ISSN No. 2277 – 8179 pp 48-49.

Ujwala Rohan Newadkar, Swapnil khaimar, Arun Dodamanil pyogenic granuloma: *A clinicopathological analysis of fifty cases*. Journal of Oral Research and Review 2018; 10: 1.

Wasan L A, Nadia M K, Suha T A. *Assessment of Pyogenic granuloma of the Gingiva in Iraqi Patient*. Indian Journal of Public Health Research & Development, November 2020, Vol. 11, No. 11.

معالجة الورم الحبيبي الليفي الفموي باستخدام دايود ليزر ثنائي الطول الموجي 980نانومتر و 810 نانو متر

اية عبدالكريم مجيد تحرير نزال الدليمي

جامعة بغداد / معهد الليزر للدراسات العليا

الخلاصة

الخلفية والمعلومات: الورم الحبيبي القيحي (PG) هو ورم حميد مفرط التنسج ، يقع غالبا داخل الفم مكان اللثة الحدية ، وغالبًا ما يحدث في العقد الثاني من العمر ، وله ميل قوي للتكرار بعد الاستئصال البسيط.
الهدف من الدراسة: تقييم المزايا العلاجية لليزرالصمام الثنائي 810-980 nm في علاج الورم الحبيبي القيحي داخل الفم.
المواد والطريقة: تم تسجيل ما مجموعه 28 مريضًا (14 رجلاً و 14 أنثى) في هذه الدراسة وتم إزالة الورم الحبيبي القيحي جراحيًا باستخدام ليزر ديود. خضع جميع المرضى لتخدير موضعي وخضعوا لعملية جراحية مماثلة (خرطوشة تحتوي على 1 بالمائة ليدوكائين مع إبينيفرين 1: 100.000). لتحقيق الإرقاء وتقليل النزيف ، تم القضاء على الآفات تمامًا عن طريق مسح طرف ألياف الليزر عبر موقع العملية. للسماح للجروح بالشفاء، لم يتم خياطتها. ثم أرسلت العينات للتشريح النسيجي المرضي.
النتائج والاستنتاجات: في الدراسة الحالية ، لاحظنا أن حجم الألم والنزيف والوذمة انخفض تدريجياً خلال أول زيارتين. اختفت العلامات التي تم قياسها تمامًا بعد أسبوعين في معظم الحالات ، كما تحسّن أيضًا رضا المريض والاداء الوظيفي. تم استدعاء المرضى بعد أسبوعين ، وقد التئمت الجروح تمامًا ولم يشكو المرضى من أي نوع من الانزعاج. من المعتقد بشكل عام أن بيئة الفم السيئة وسوء تركيب طقم الأسنان قد يؤدي إلى تكرار الإصابة. وفقا للنتائج التي تم الحصول عليها ؛ إزالة الورم الحبيبي القيحي باستخدام ليزر دايود ثنائي الطول الموجي 810-980 nm هو بديل ناجح وفعال ومعقول لتقنية المبضع التقليدية (الطريقة الجراحية).

Iraqi J. Laser, issue 1, vol., 21, pp. 34-43 (2022)

IRAQI JOURNAL OF LASER

Temporal Pulse Compression Using Double Cladding Polarization Maintaining Fiber Nested Mach- Zehnder Interferometer

Ahmed U. Kareem[1] , Tahreer S. Mansour[1]

Institute of Laser for Postgraduate Studies, University of Baghdad, Baghdad, Iraq

(Received 19/02/2022; accepted 11/04/2022)

Abstract: Narrow laser pulses have been essential sources in optical communication system. High data rate optical communication network system demands compressed laser source with unique optical property. In this work using pulsed duration (9) ns, peak power 1.2297mW, full width half maximum (FWHM) 286 pm, and wavelength center 1546.7 nm as compression laser source. Mach Zehnder interferometer (MZI) is built by considering two ways. First, polarization maintaining fiber (PMF) with 10 cm length is used to connect between laser source and fiber brag grating analysis (FBGA). Second, Nested Mach Zehnder interferometer (NMZI) was designed by using three PMFs with 10 cm length. These three Fibers are splicing to single mode fiber (SMF-28) that has 5cm length. Both designs are etching in Hydrofluoric acid HF 40 percent concentration with three different duration time (10,20 and 30) min. Tunability of this pulsed laser source can be chained after applying different mechanical weights (0,10,50,100,250,500) g are applied to two areas across the fiber; the cross section and splicing regions. It was possible to observe, the maximum excitation of higher order modes for compression factor (FC) was found in splicing region which it is 1.02. this value is recorded under 500g that subjected to the fiber that has 10cm length with 30 min etching. In addition, the thickness cladding was 72.8 µm. also, the maximum peak power for both designs is 90.124 µw and wavelength center is 1546.817 nm.

Keywords: pulse compression, nested fiber interferometer, HF fiber etching, Much Zehnder Interferometer, Polarization Maintaining fiber. Force weight

1. Introduction

optical systems have been an important target by many researchers. Because, it has been applied in many fields. Optical fibers are uses in different applications like fiber sensing, spectroscopic analysis, optical fiber laser, and optically filtering [1]. The Compressed laser source is an essential part for high data rate communication system in the applications of network fiber sensing and wavelength division multiplexing. In this experiment, panda polarization-maintaining fiber(PMF) was used, which is a special type of single mode fiber, designed to transmit only one polarization of the input light. It has a high birefringence with predetermined slow and fast axes. Specification (PMF)operating wavelength range (1440-1625) nm, cutoff wavelength (1370nm), extinction ratio (23) db. [2,3]. The interferometer was subjected to different mechanical forces to compress the optical pulse out from the interferometer and

develop a low cost, narrow optical Hussain implemented a pulse compressor using a tunable Mach-Zehnder interferometer made of 7 and 19 hollow fiber optic photonic cells after applying mechanical forces along the fiber cross-sectional area to obtain a compression factor (FC) equal to 2 and 4 for 7- and 19-cell hollow core optical crystal fibers (HC-PCF) respectively [4]. In (2019), Haseda, Yuki Pulse wave signals were measured by POF-FBG and silica-FBG sensors for four subjects. After signal processing, a calibration curve was constructed by partial least squares regression[5]. In Ali A. Dawood used 7 and 19 HC-PCF cells to build the Mach-Zehnder interferometer, but they replaced the air holes with fibers with 25% dilute acrylic acid with 75% ethanol and were able to achieve FC = 4.9[6]. in (2021) using Bara H Muter a tunable narrow pulse laser source using polarization-preserving fibers using the comsol multi-physics dynamic simulation model, version (5.5) to obtain a compression factor (FC) equal to (1.1) [7].

In this paper, two ways are considered to design (MZI). The first method is single fiber (10) cm with different etching (10,20,30) min. The second method is (NMZI) with same etched that mentioned in first method. In section 2, the methodology and procedure are explained deeply. The results are discussed in section 3 with graphs. The paper ended with conclusion in section 4.

1. methodology and procedure

Optical pulse laser source launched to PM-Mach Zehnder Interferometer. PM-MZI was building by using PMF with three constant (10) lengths cm sandwiching between two standard single-mode optical fibers (SMF-28e) with length (5) cm with different etching (10,20,30) min. PMF is design in two ways. the first case the single fiber and other case (NMZI)with etched each two cases The single PM-MZI consists of one PM-MZI that means two micro cavity splicing regions (MCSRs), one cavity length (Lc), the mechanical force in (g) was varied from (0,10,50,100,250,500) (g) applied on the interferometer micro–cavities splicing regions in two cases. The mechanical force was used to tune the phase of the optical communication source. In (2018), Surat signal on one arm of the PM-MZI. The applied forces-imposed stress on the fiber caused elongation in the length of the fiber. The amount of the fiber elongation can be calculated using equations (1)(2),(3) [1].

$$\text{the strain} = \frac{\Delta L}{L} = \frac{stress}{young\ modulus} \qquad (1)$$

$$\text{stress} = \text{Force (N)} / \text{Area (m)} \qquad (2)$$

$$F = m \times G \qquad (3)$$

where:

L is the original length.

ΔL is the change in length.

F is the force applied in (N).

A is the cross-sectional area in (m^2).

M is the value of the standard weight mass used to induce mechanical force.

G is the gravitational acceleration.

The obtained experimental results of strain measurement will be divided according to the change length of Polarization maintaining fibers that used in interferometers. The values of the mass in g were converted to the force in N, this conversion process has been evaluated according to equation (3). The increase in the force that applied on the micro-cavity leads to an increase in the strain When the force was applied on PM-MZI cavity in case single PMF and NMZI The elongation for micro cavity splicing region will be reducing of the geometric parameters of PMF, this change of parameters caused decreased the group velocity for all modes which propagated through the core and cladding. In case NMZI switch has a balanced structure, in which the optical path lengths are equal in the three main interference arms, as a result, the bandwidth of the optical process is not limited by the converter structure, that is, broadband performance can be achieved. In general, the interference

pattern depends on the optical path length, the offset between the two arms of the interferometer because the base mode has a higher effective index than cladding mode [8]. For the above reasons, we have to calculate the values of the phase differences that give us the three-arm synchronous photon propagation of the NMZI as equation (4) [9,10].

The phase different between the cladding and core mode is described by:

$$\Delta\Phi=\frac{2\pi}{\lambda\Delta n\, L} \quad (4)$$

Where L is the interaction length in cm.

The intensities the cladding and core modes measured function wavelength of physical length.

$$I(\lambda)= I_1 + I_2+2\sqrt{I_1 + I_2}\cos(\Delta\Phi) \quad (5)$$

Where I_1+I_2 are the mode intensities of core and cladding modes.

The change in the effective refractive index of the mode can calculated by.

$$\Delta n_{eff}= nx_{eff} - ny_{eff} \quad (6)$$

The beat length, LB, can be calculated in direct relation to the refraction B using equation (7).

$$LB = \frac{2\pi}{\Delta\beta} = \frac{\lambda}{B} \quad (7)$$

where Δβ is the difference between the x and y components of the wave propagation constant along the PMF and n_x, n_y is the effective refractive index as a function of the wavelength of both the x and y polarization component [11].

In other hand the important parameter as a part of fiber characteristics was fiber dispersion, because etching fibers and applied force cause multipath in fiber. There is multipath dispersion inside each arm of NMZI, Rays disperse in time at the output end of the fiber where they were coincident at the input end and traveled at the same speed inside the fiber, this can be estimated by considering the shortest and longest ray paths. The sensing area in the design is represented by the Multimode fiber because of use of different refractive index result etched PMF. the normalized frequency must be obtained according to the following equation (8):

$$V=2\frac{\pi a}{\lambda}\sqrt{n_1^2 - n_2^2} \quad (8)$$

Where V is normalized frequency [12].

Where a is core radius, λ is wavelength central. In (nm).

The narrower pulse in time domain has the wider spectrum in spatial domain is a very well-known concept in communication. Therefor the figure of merit of this study is characterized by the Temporal compression factor which is the ratio of input signal full width at half maximum to the output signal full width at half maximum.

$$Fc= FWHM_{\,i/p} / FWHM_{\,o/p} \quad (9)$$

The temporal FWHM can be obtained from the spatial FWHM using the equation:

$$FWHM_{(temporal)} = \frac{(\lambda C)^2}{C \times FWHM(\text{spatial})} \quad (10)$$

where: λc central wavelength in nm.

c is the speed of light in vacuum [13].

In this experiment In addition to the use of force applied to two areas in the fiber, the fibers were etched by Hydrochloric acid (HF) of 40 % concentration was used experimentally to etch the polarization maintaining fiber for three different time periods ranged from (10,20,30) min. each step 10min. polarization maintaining fiber has two stress cores parallel to each other. When etching period take longer duration a portion of the two stress cores will be removed and as a consequence; new form of optical fiber will be developed at the etching region. it is important to inform that only 2-3 cm of PMF was etched not the whole 10cm [14].

The work was the installation of two designs. The first is the single fibers, three fibers, each fiber 10 cm long, with

different etching time of (10, 20, 30) min, and the authority of different weights (0,10,50 100, 250, 500) on each fiber and on two areas of the fibers (cross section and splicing region) It is the same as the above fibers (SMF), The second design is the same as the first case fibers with the same specifications mentioned and the supplied force, but in the design (NMZI) as block diagram in the below

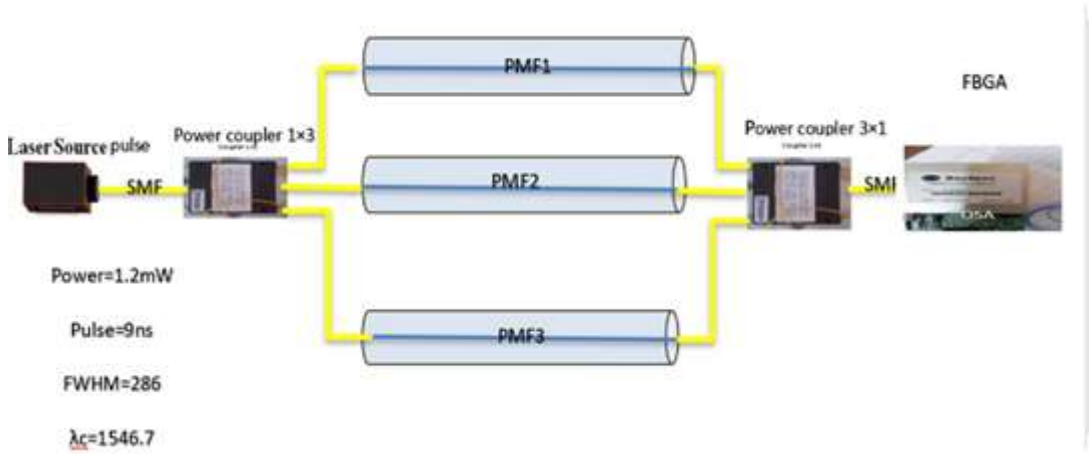

Figure (1): Schematic diagram of Nested PM-MZI

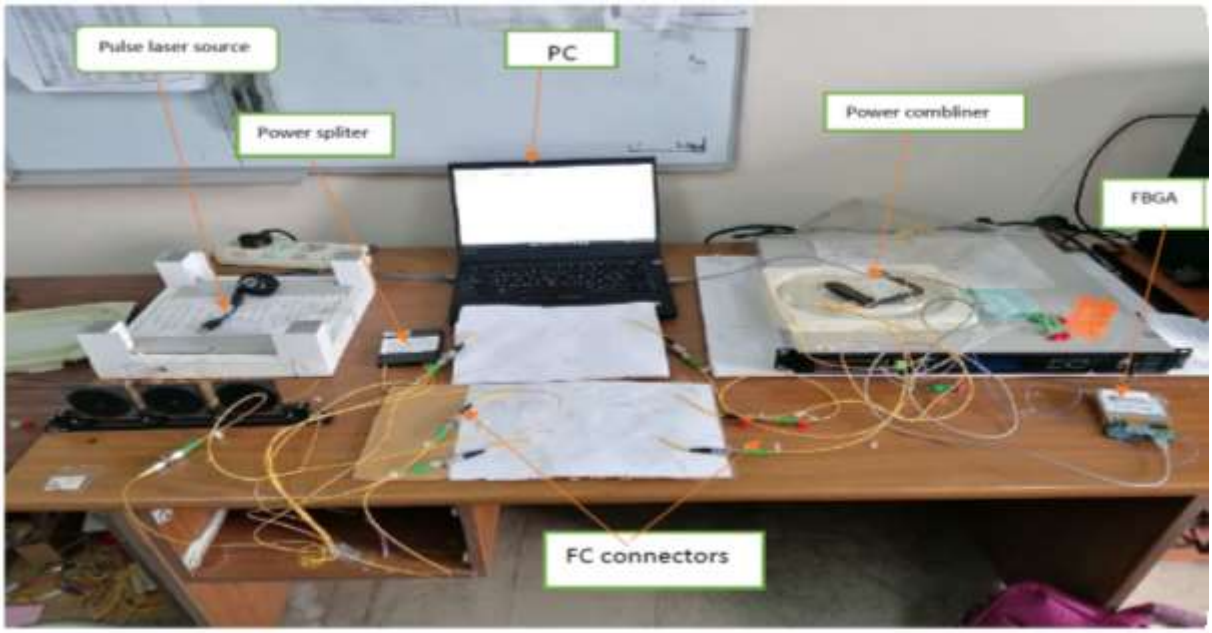

Figure (2): photograph image of the etched PM-NMZI experiment

In this study was used the pulse laser source has peak power 1.2297mW, full wave half maximum (FWHM) 286 pm, and wavelength centered at 1546.7 nm. The measured output wave length, peak power, FWHM, by type from Thorlabs (fiber Bragg grating analysis) Bay spec-FBGA, as in figure (2)

Result and Discussion

The result divide into two parts, the first part is the two designs (single fibers, NZMI) etched without applied force and the second part with applied force.

A. Results for etching effect

The laser beam profile is characterized by its linewidth which is calculated by taking the Full Width at Half Maximum (FWHM) of intensity distribution of laser beam versus wavelength. This work recorded the effect of etching on FWHM. which showed efficient temporal pulse compression for communication networks. The detected peak power was increased with etching for the whole constant fiber length samples, this result arises promising application for the etched PM-MZI in refractive index sensing because the etching process of PMF modified the effective refractive index for the optical fiber. In general, it is known for fiber sensors; the polarization rotation along optical fiber reduces the accuracy of them. Therefore, the obvious power increasing with longer etching duration while the central wavelength is almost fixed can provide more accurate measurements. Table (1) show the results the wavelength, peak power, FWHM and compression factor after the different time etched (10,20,30) to PMF single fiber and NMZI. Note that the length of the fiber used was (10) cm.

Table (1): The change of PMF and NMZI under the etching effect for three-time durations.

Etching period (min)	λc(nm)	Po(mW)	FWWH (pm)	FC	Normalized frequency (V)
10 min	1546.708	0.769	246	1.1	136.56
20 min	1546.725	0.752	227	1.2	158.44
30 min	1546.853	0.696	155	1.8	174.90
NMZI with etching (10,20,30) min	1546.884	0.188	210	1.3	-

When etched PMF the refractive index changes in the cladding. This phenomenon shows the Fiber diameter after etching is change causes different refractive index in the surrounding and can be applied to measure the RI new. When chemical etching ends- the cladding diameter of thinned PMF is obtained about 72.8μm after the etched 30 min. It is worth noticing that Δn is decreased after chemical etching. The benefit of this process is to make all the laser beam inside the core and thus increase temporal pulse compression for communication networks.

The effect of the time periods for etching on fiber we can observe in Figure (3-a,b,c) relationship with wavelength ,peak power and Fiber diameter.

Table (2): show the effect etching to the fiber thickness.

Time of etching	Fiber diameter after etching (μm)	Refractive index
10min	112.1	1.3876
20 min	88.3	1.36253
30min	72.8	1.34122

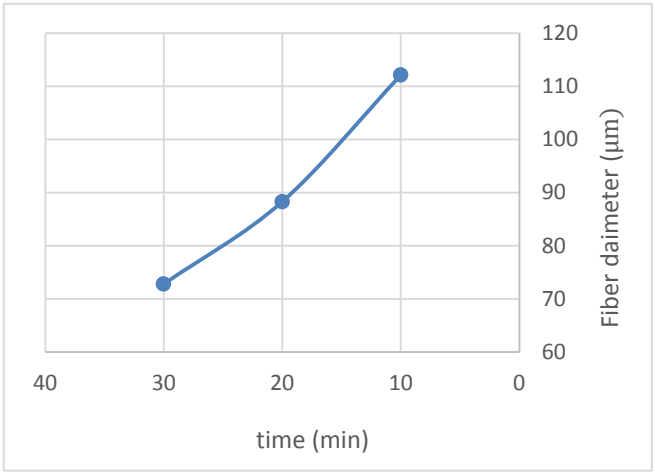

Figure (3-a): The relationship between time etching and fiber diameter (µm).

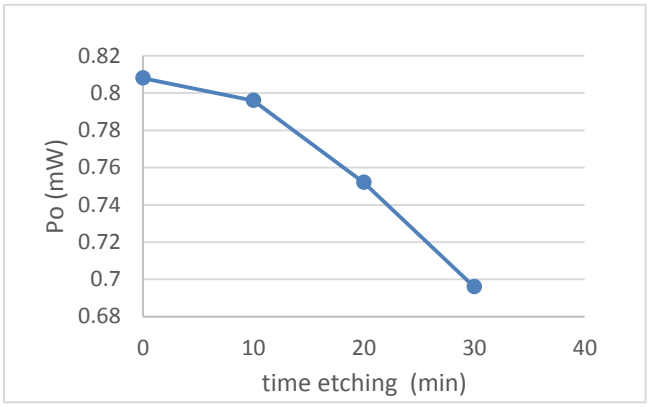

Figure (3-b): The relationship between time etching and peak power.

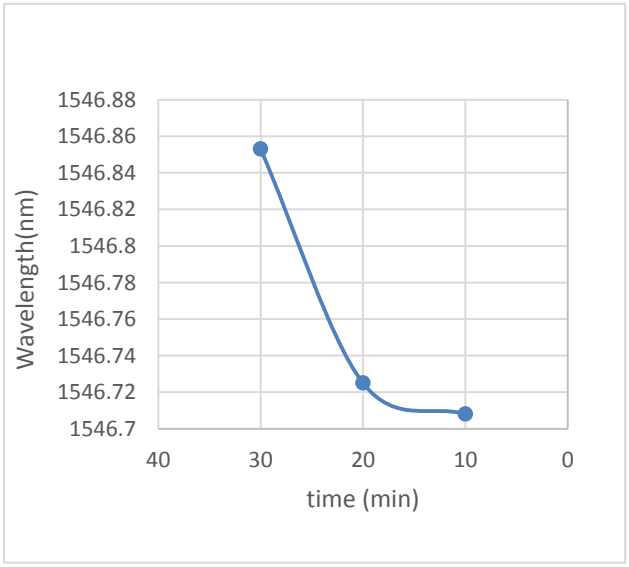

Figure (3-c): The relationship between time etching and wavelength

B. Results for force effect with etching fiber

When the force was applied on PM-MZI as single fiber and nested which is etching. The first case single fiber is the elongation for micro cavity splicing region of PM-MZI will be reducing of the geometric parameters of PMF, this change of parameters caused

decreased the group velocity for all modes which propagated through the core and cladding for the fiber and the reducing in parameters of fiber will be changed on the parameters of pulse that propagated through the fiber. The output spectra of PM-Mach Zehnder Interferometer due to the force effect, that was obtained by applying different values of force (0,10,50,100,250,500) on the micro- cavity of PM-MZI with three constant length and different etching time (10,20,30). The increase in the force applied to the micro-cavity leads to an increase in the FWHM. The highest spectral width 280 (pm) has been gained when the PMF was 10 cm length and time etching 30 min applied weight 500 g on micro cavity splicing regions. The second case NMZI the high result record, when applied weight 500 g in splicing region which FWHM 271(PM), compression factor 1.05.

The output spectrum of the PM-Mach Zehnder interferometer was visualized by using Bay spec -FBGA, after applying different mechanical weights, on their micro cavities splicing regions, to measured optical power, wavelength center shift, FWHM, as shown in figure (4-a,b,c).

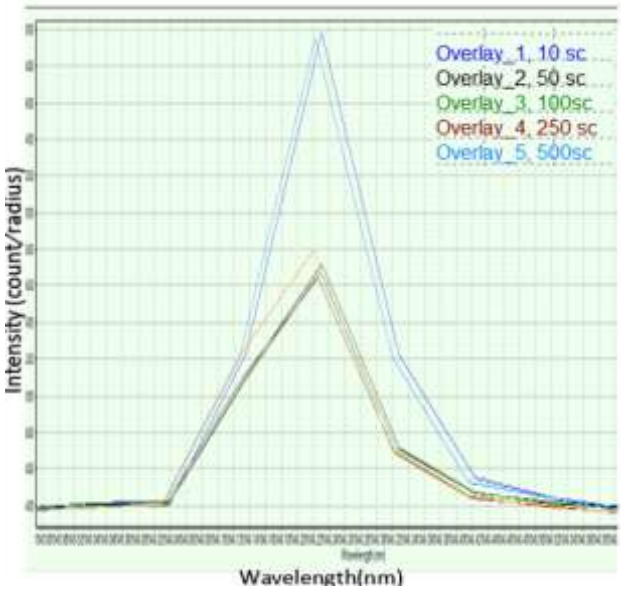

Figure (4-a): The spectrum of the output laser source PM-MZI after applying different weights in case PMF length 10cm and time Etching 10 min on micro cavities

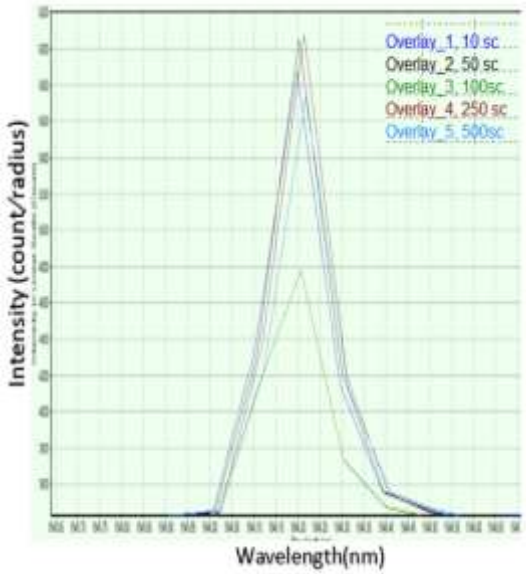

Figure (4-b): The spectrum of t fferent weights in case PMF length 10cm and time Etching 2

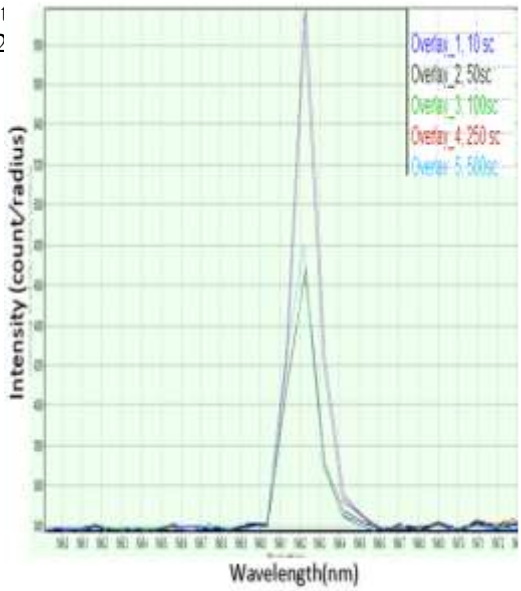

Figure (4-c): The spectrum of the output laser source PM-MZI after applying different weights in case PMF length 10cm and time Etching 30 min on micro cavities.

The increase in the force applied to the micro-cavity leads to an increase in the FWHM. The highest spectral width 280(pm) has been gained when the PMF was 10 cm length, time etching 30 min and 500 g weights applied on micro cavity splicing regions as show in figure (5-a).

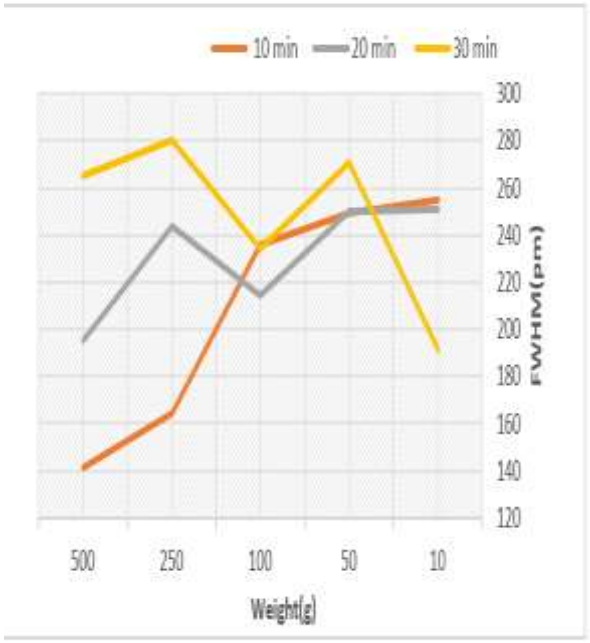

Figure(5-a): The Full Width Half Maximum variation of PM-MZI with (10cm), time etched (10,20,30) and different forces applied on micro cavities splicing regions.

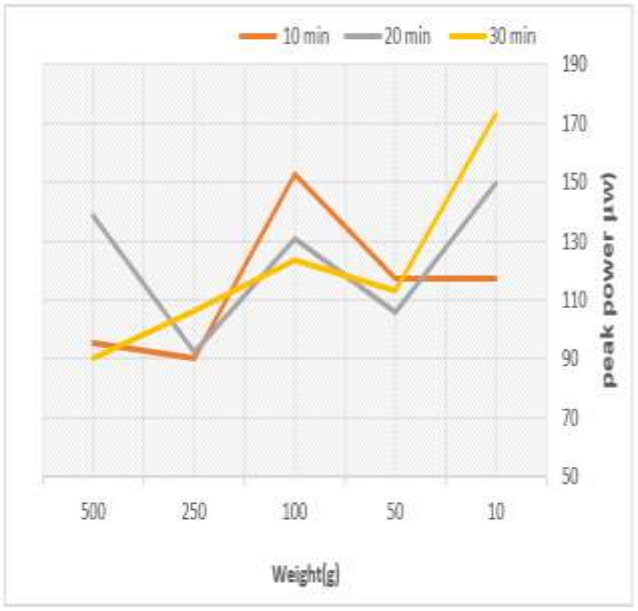

Figure(5-b): The peak power variation of PM-MZI with (10 cm),time etched (10,20,30)min and different weights applied on the micro cavities splicing regions.

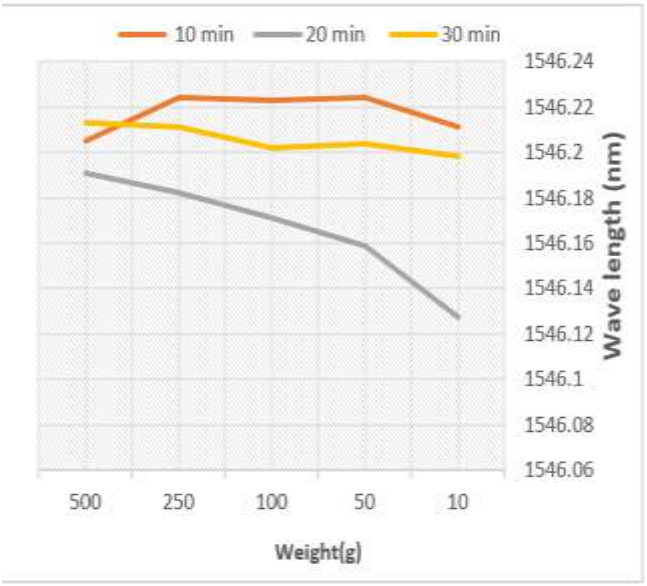

Figure(5-c): The wavelength variation of PM-MZI with (10 cm) and time etched (10,20,30) different weights applied on the micro cavities splicing region

The wavelength shift of the PM-MZI spectrum is very clear due to the different values of weights applied on the micro-cavity splicing region as shown in figure (5-c).

4. Conclusion

The main points that can be concluded from this work are, the MZI micro-cavities shows high interference and good sensitivity and are thought to be caused by the large force that is applied to a small area and also because of the etch. After etch 10 cm from PMF with (HF) of 40 % concentration was used experimentally to etch the polarization maintaining fiber, these results to give rise to the possibility of getting narrower temporal pulses for communication applications. when the PMF was 10cm in length, etch 30 min and the force (0.00489N) applied on micro cavity splicing regions cause the compression factor 1.01 because this fiber has two stress members which make it highly sensitive to any physical effect. When comparing this experiment with previous experiments in the same field, the following becomes clear: The fibers used in this experiment are short in length and a small number of adaptors, and accordingly we get the least losses, less dispersion, the best temporal compassion factor, and a smaller size (MZI) in terms of the lengths of the linked fibers. In addition to using (NMZI) with applied weights and etch fiber. which gave good results in terms of wavelength, peak power and FWHM.

5. References

[1] A.T. Yahiya and T. S. Mansour, "Tunable band pass Filter based on Nested Mach-Zehnder interferometer," J. Eng. Applied Sci., Vol.13.pp7450-7458, (2018).

[2] E. Schema, D. Tosi, P. Sacco mandi, E. Lewis, and T. Kim, "Fiber optic sensors for temperature monitoring during thermal treatments: an overview", Sensors, vol. 16, no. 7, p. 1144, (2016).

[3] Y. Wang, S. Wang, L. Jiang, H. Huang, L. Zhang, P. Wang, L. Lv, and Z. Cao, "Temperature-insensitive refractive index sensor based on Mach-Zehnder interferometer with two micro cavities," Chin. Opt. Lett., Vol.15, pp.020603, (2017).

[4]M. Sura Hussein, T. S. a. Mansour, H. Yousif Ibrahim, and M. Laith Tariq, "Pulse compression by using 7 and 19 cells 1550 hollow core photonic crystal fiber," *J. Eng. Appl. Sci.*, vol. 13, no. 17, pp. 7198–7204, 2018, doi: 10.3923/jeasci.2018.7198.7204.

[5]Y. Haseda, J. Bonefacino, H.-Y. Tam, S. Chino, S. Koyama, and H. Ishizawa, "Measurement of pulse wave signals and blood pressure by a plastic optical fiber FBG sensor," *Sensors*, vol. 19, no. 23, p. 5088, 2019.

[6]A. A. Dawood, T. S. Mansour, and Y. I. Hammadi, "Demonstration of All-Fiber Pulse Compression Using Hollow Core Photonic Crystal Fibers," *Cont. Math. Sci*, vol. 14, no. 5, pp. 158–169, 2019.

[7]B. H. Mutar, N. F. Noori, Y. I. Hammadi, and T. S. Mansour, "In-line fiber tunable pulse compressor using PM-Mach Zehnder interferometer," *J. Mech. Eng. Res. Dev.*, vol. 44, no. 5, pp. 287–297, 2021.

[8]A. M. Shrivastav, D. S. Gunawardena, Z. Liu and H. Tam, "Microstructured optical fiber based Fabry–Perot interferometer as a humidity sensor utilizing chitosan polymeric matrix for breath monitoring" Scientific Reports, Vol:10, (2020).

[9] S. Deng, H. Meng, X. Wang, X. Fan, Q. Wang, M. Zhou, X. Guo, Z. Wei, F. Wang, C. Tan, and X. Huang, " Graphene oxide-film-coated splitting ratio adjustable Mach-Zehnder interferometer for relative humidity sensing", optics express, Vol. 27, No. 6, (2019).

[10] Q. Wang, W. Wei, M. Guo and Y. Zhao, "Optimization of cascaded fiber tapered Mach–Zehnder interferometer and refractive index sensing technology", Sensors and Actuators B: Chemical, Vol. 222, pp.159-165, (2016).

[11] M. Chena, Y. Zhao,_, H. Wei and Krishnaswamy, "Cascaded FPI/LPFG interferometer for high-precision simultaneous measurement of strain and temperature", Elsevier, Vol. 53, No.102025 ,(2019).

[12] L. Zhang, S. Sun, M. Li, and N. Zhu, "All-optical temporal fractional order differentiator using an in-fiber ellipsoidal air-microcavity," Journal of Semiconder., Vol. 38, No. 12, pp. 126001, (2017).

[13] F. Q. Mohammed, T,S. Mansour and A. W. Abdul wahhab, " A tunable Mach–Zehnder interferometer based on dual micro‐cavity photonic crystal fiber for load measurement, " Photon Newt Common. Vol.38, pp. 270-279 (2019).

[14] X. Dong, H. Du, Z. Luo and J. Duan, "Highly Sensitive Strain Sensor Based on a Novel Mach-Zehnder Interferometer with TCF-PCF Structure" *Sensors*, Vol. 18, No. 1: 278, (2018).

ضغط النبض الزمني باستخدام استقطاب الكسوة المزدوجة للحفاظ على مقياس التداخل ماخ زندر المتداخل بالألياف

احمد عذافه كريم تحرير صفاء منصور

معهد الليزر للدراسات العليا، جامعة بغداد، بغداد، العراق

الخلاصة: كانت نبضات الليزر الضيقة من المصادر الأساسية في نظام الاتصال البصري. يتطلب نظام شبكة الاتصالات الضوئية ذات معدل البيانات العالي مصدر ليزر مضغوط بخاصية بصرية فريدة. في هذا العمل باستخدام مدة نبضيه (9) ns، وقوة الذروة mW1.2297، ونصف العرض الكاملة القصوى 286 (FWHM)، ومركز الطول الموجي 1546.7 نانومتر كمصدر ليزر للضغط. تم بناء مقياس التداخل Mach Zehnder (MZI) من خلال النظر في طريقتين. أولاً، يتم استخدام ألياف الحفاظ على الاستقطاب (PMF) بطول 10 سم للربط بين مصدر الليزر وتحليل شبكة الألياف الضوئية (FBGA). ثانيًا، تم تصميم مقياس التداخل Nested Mach Zehnder (NMZI) باستخدام ثلاثة PMFs بطول 10 سم. تقوم هذه الألياف الثلاثة بالربط إلى ألياف أحادية النمط (SMF-28) يبلغ طولها 5 سم. كلا التصميمين محفور في تركيز حمض الهيدروفلوريك 40 HF في المائة مع ثلاث فترات زمنية مختلفة (10، 20 و30) دقيقة. يمكن ضبط قابلية ضبط مصدر الليزر النبضي هذا بعد تطبيق أوزان ميكانيكية مختلفة (500،250،100،50،10،0) جم على منطقتين عبر الألياف؛ المقطع العرضي ومناطق الربط. كان من الممكن ملاحظة أن أقصى إثارة لأوضاع الترتيب الأعلى لعامل الضغط (FC) تم العثور عليها في منطقة الربط وهي 1.02. يتم تسجيل هذه القيمة تحت 500 جم التي تم تسليطها على الألياف التي يبلغ طولها 10 سم مع نقش 30 دقيقة. بالإضافة إلى ذلك، بلغت سماكة الكسوة 72.8 مايكرومتر. كما أن أقصى قدرة للذروة لكلا التصميمين هي 90.124 µw ومركز الطول الموجي 1546.817 نانومتر.

Iraqi J. Laser, issue 1, vol., 21, pp. 44-50 (2022)

IRAQI JOURNAL OF LASER

Towards C+L Band Three-Mode (De)Multiplexer Using Subwavelength Grating (SWG) Technology

Zaid Lateef Hussain[1], Raad S. Fyath[2]

1University of Baghdad, Institute of Laser for Postgraduate Studies, Baghdad, Iraq
2Al-Nahrain University, College of Engineering, Department of Computer Engineering, Baghdad, Iraq

(Received 05/02/2022; accepted 30/03/2022)

Abstract: Recently, there is increasing interest in using mode-division multipelexing (MDM) technique to enhace data rate transmission over multimode fibers. In this technique, each fiber mode is treated as a separate optical carrier to transfer its own data. This paper presents a broadband, compact, and low loss three-mode (de)multiplexer designed for C+L band using subwavelength grating (SWG) technology and built-in silicon-on-insulator SOI platform. SWG offers refractive index engineering for wider operating bandwidth and compact devices compared to conventional ones. The designed (de)multiplex deals with three modes (TE0, TE1, and TE2) and has a loss > -1 dB and crosstalk < −15 dB, and its operation cover 160 nm (1490 to 1650) nm wavelength span. The overall size of the designed device is 80 × 4 μm^2.

1. Introduction

Demultiplexers are the key elements in mode division multiplexing (MDM) technology and bandwidth expansion [1,2]. Several (de)multiplexing schemes such as Y-junction, micro-ring resonators (MRR), multimode interference (MMI), directional couplers (DC), and coupled waveguides have been reported [3-7]. The MMI coupler has the most interest in multiplexer's design since it offers good performance over a wide bandwidth [8]. Generally, these devices are designed to operate in the C-band range. In MDM, it is preferred to operate with a maximum number of modes and wide operating bandwidth [9]. Expanding the operating bandwidth beyond the C-band is an effective solution to handle capacity issues in the existing optical infrastructure with no need to add new hardware resources [10]. Thus, extending the operating bandwidth towards L-band will allow the use of current technologies to be used over the C+L band [11]. The reason behind considering L-band is due to attenuation losses for C and L bands are approximately the same, also the erbium-doped fiber amplifier can be tuned easily to operate for the new C+L band [12]. Recently, researches have been reported for demultiplexer operating in C+L bands utilizing Y-junctions, directional couplers (DC), and air-core ring fiber [13-17]. Recalling the advantages of the MMI coupler, yet, it is still restricted by the refractive index of the silicon in terms of limited bandwidth and large size and therefore subwavelength grating (SWG) technology has been introduced for refractive index engineering [18]. SWG waveguides are built from two materials arranged periodically as strips in dimensions less than the wavelength of the propagating light. This results in suppression of dispersion effect and an

equivalent homogenous medium with optical properties that combine those of the constructing materials [19]. Applying this technology produces compact, wide-band, and low-loss devices [20].

In this paper, a dual-bandwidth, low loss, compact, and fabrication tolerant three-mode demultiplexer is designed utilizing subwavelength grating (SWG) technology. The device consists of an MMI coupler, a phase shifter, and a splitter to (de)multiplex the three input modes TE0, TE1, and TE2 into a uniform fundamental TE0 mode at the output ports. The results show that the designed device has a loss > -1 dB and crosstalk < −15 dB, 160 nm wavelength span (1490 to 1650) nm covering C+L bands, and 80 × 4 μm^2 overall footprint. The simulation is carried out via Rsoft photonics CAD version 2020.03.

2. Design Dimensioning and Analysis

According to the 100 GHz, IUT wavelength grid issued for wavelength division multiplexing (WDM), each of the L- and C- bands covers 10 THz bands. The L-band covers 50 channels starting from 186 THz (1161.78 nm) to 190.9 THz (1570.41 nm). The C-band covers 50 channels too, starting from 191 THz (1569.59) nm to 195.9 THz (1530.33 nm). Thus C+L starts from 1530.33-1611.78 nm centered at 1569.59 nm which is the designed wavelength of the proposed device. The scheme of the proposed device is shown in Figure 1.

The device is designed using SWG technology and based on an SOI platform with a rib/ridge waveguide structure. The SWG comprising materials are Si (n_{Si}=3.46) and SiO_2 (n_{SiO2}=1.46) arranged periodically as strips of thickness a_i and duty cycle D.C =Λ_i/a_i, repeated over a period $\Lambda_i \ll \lambda_{light}$. The slab and component heights are 0.2 μm and 0.5 μm, respectively. The device consists of three sections, the 1x3 splitter, $\pi/2$ phase shifter, and 3x3 MMI coupler. It handles three input modes TE0, TE1, and TE2 which are converted into a TE0 mode at the output ports.

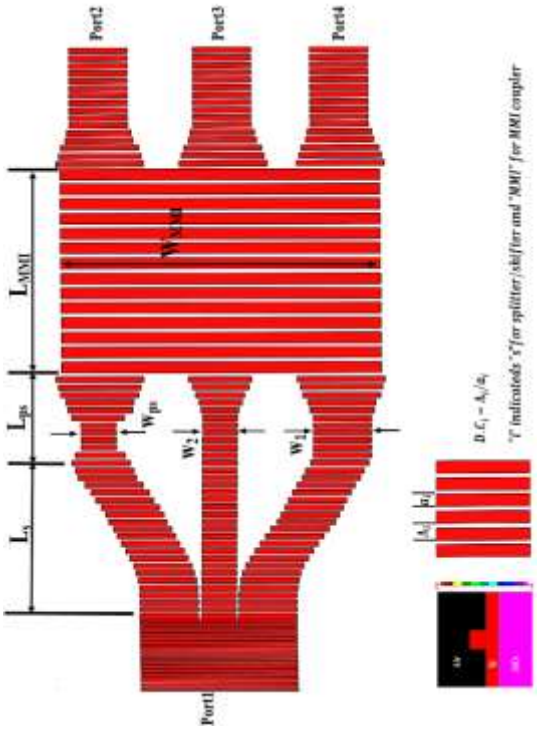

Fig.1: Schematic diagram of the proposed device. The inset is waveguide cross-section and SWG details.

The 1x3 splitter is designed so that TE0 and TE1 modes are split equally to the outer arms (of width w_1), while TE2 is guided through the central arm (of width w_2) only. To satisfy the desired operation, splitter dimensions including pitch length Λ_s (duty cycle (D.C) %), arm length and arms widths L_s, w_1, and w_2 are numerically determined for the optimum performance. Figures 2(a) shows simulation results of the splitter normalized transmission as a function of arm width variation for each one of the input modes. It is obvious that outer arms, for the case of TE0 and TE1, can be guided with maximum transmission and TE2 with minimum transmission when w_1 is set to 0.5 μm (refer to the orange and blue lines). In contrast, for central arm, the maximum transmission of TE2 and minimum transmission of TE0 and TE1 occur when w_2 is 0.27 μm (refer to the red and violate lines) Similarly, the length of the splitter arms is deduced to achieve maximum transmission for each mode. The result is depicted in Figure 2(b) which shows that the optimum value of the length is at L_s= 25 μm. Note that to ensure a smooth transition of the field along the segmented waveguide, the eddect of Λ_s (duty cycle (D.C) %), is simulated and the results are shown in Figure 2(c), and thus Λ_s is set to 0.16 μm yielding D.C. = 70%.

The device transmission characteristics can be obtained as a multiplication of the transmission functions of the three stages compromising the device. Recall that the device consists of three sections, the 1x3 splitter, $\pi/2$ phase shifter, and3x3 MMI coupler. Note that the transfer function of the splitter is wavelength dependent.

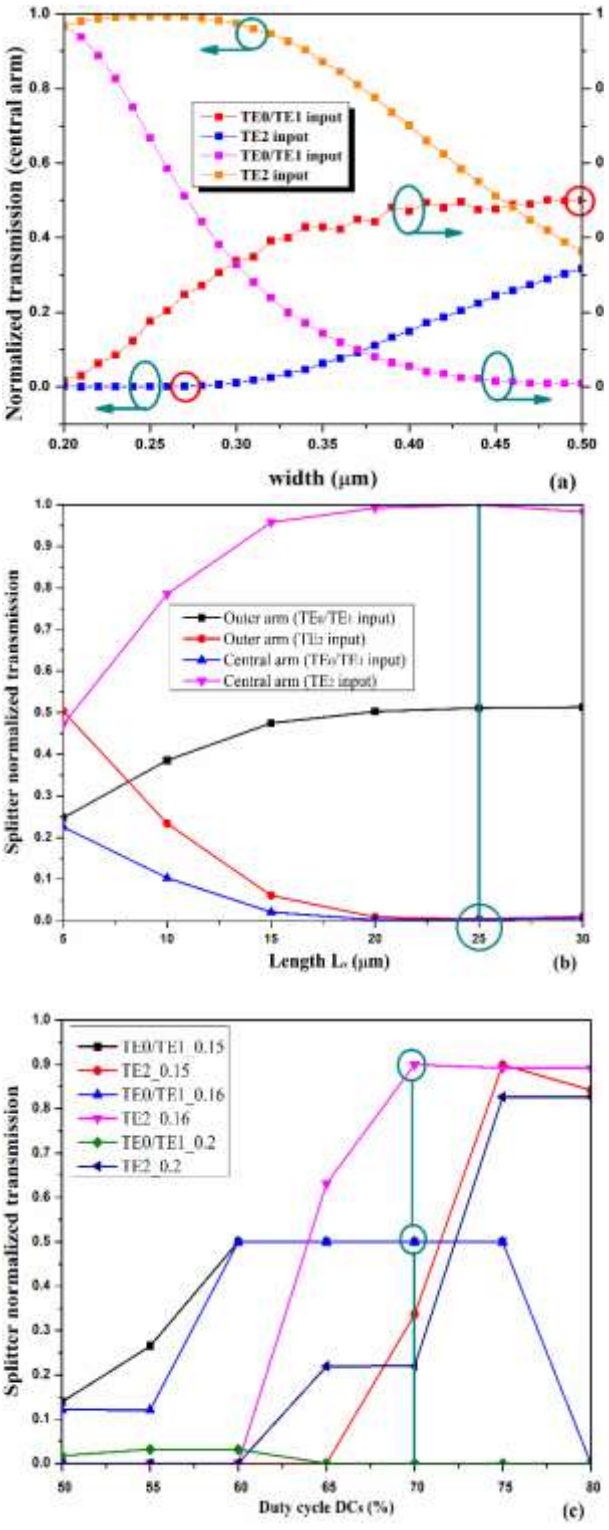

Fig.2: Splitter transmission as a function of arms (a) width (b) length (c) duty cycle.

Next, a $\pi/2$ the phase shifter is designed based on the phase difference between two waveguides of different widths. The shifter is placed at one of the outer arms, thus only TE0 and TE1 cases are affected. The dimensions of the shifter are the length L_{ps} which is set to 3 μm for compactness purposes, and the width w_{ps}. Figure 3 shows the phase difference as a function of width variation w_{ps}. Note that the desired shift can be achieved at any intersection point of the red line curve with the $\pi/2$ margin line. Thus, width $w_{ps} = 0.22, 0.26, 0.31, \text{and } 0.42$ μm can serve the purpose. In this design $w_{ps} = 0.31$ μm is choosen

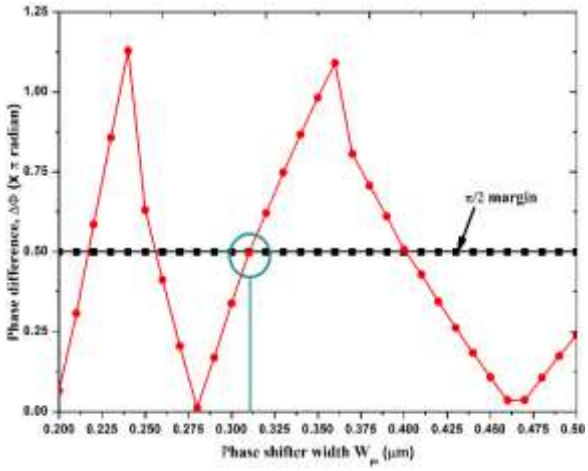

Fig.3: Phase difference as a function of shifter width w_{ps}.

Finally, the 3x3 MMI section is designed. The desired function is to act as a 3-dB splitter for the case of TE0 and TE1 mode (outer input ports), whereas for the TE2 mode case, the field is guided directly from the central input port to the central output port. Thus, it is required to choose MMI length L_{MMI} , width W_{MMI}, pitch length Λ_{MMI} to satisfy these requirements. The MMI length can be expressed in terms of modified beat length L_π formula by the effect of SWG technology as follows [8]

$$L_{MMI} = 1.5L_\pi \quad (1)$$

$$L_\pi = \frac{4n_{eff}W_{MMI}^2}{3\lambda_{light}} \quad (2)$$

where λ_{light} is the wavelength of the light ($\lambda_{light} = 1569.6\,nm$), n_{eff} is the SWG effective refractive index given by [20]

$$n_{eff} = \left[(n_{Si}^2 + n_{SiO_2}^2).\frac{\Lambda}{a}\right]^{1/2} \quad (3)$$

The width W_{MMI} and pitch length (duty cycle %) are set to 4 µm, and 0.2 µm (50%) for compactness purposes, respectively. Numerical simulation for the optimum value of L_{MMI} is carried out around theoretical value calculated from equation (1). Figure 4 presents the response of the MMI coupler as a function of its length. The results show that the suitable L_{MMI} value is 45 µm at which TE0 and TE1 are split equally through the outer ports, whereas the TE2 field is guided directly from the central input to the central output port.

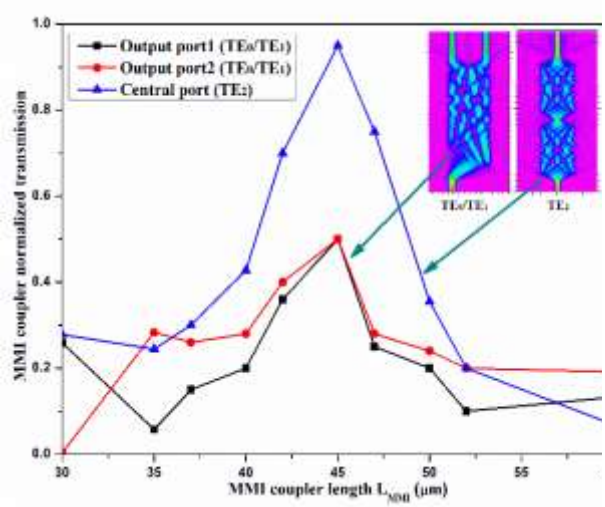

Fig.4: Coupler transmission as a function of the length L_{MMI}.

3. Performance Characteristic and Evaluation

Intensity distribution study along the (de)multiplexer is carried out using Rsoft photonics CAD suit for each case of input modes across the designed device at the operating wavelength λ_{light} = 1569.6 nm. The simulation is repeated for the L+C band corresponding to 1530.3 nm and 1611.8 nm. The results are shown in Figures 5 to 7. The TE0 and TE1 mode split equally through the outer arms and the output for each case is detected from port4 and port2, respectively. For TE2 mode, guided along the central arm of the splitter and the output is detected at port3.

To evaluate the performance of the device, the insertion loss (I.L), and crosstalk (C.T) are calculated for each described case and using the following formula

$$I.L\ (dB) = 10\log(\frac{P_{out}}{P_{in}}) \quad (4)$$

$$C.T\ (dB) = -10\log(\frac{P_{out}}{\sum P_{out\_undesired}}) \quad (5)$$

where P_{in}, P_{out}, $P_{out\_undesired}$ are input power, desired output power from desired port, undesired output power from other ports, respectively. The I.L at the design wavelength > -1 dB and the C.T is better than −17.3 dB.

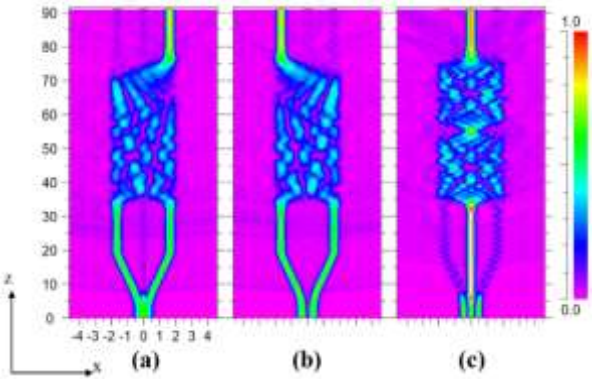

Fig.5: Intensity distribution along the demultiplexer for input mode (a) TE0, (b) TE1, (c) TE2. at 1569.6 nm.

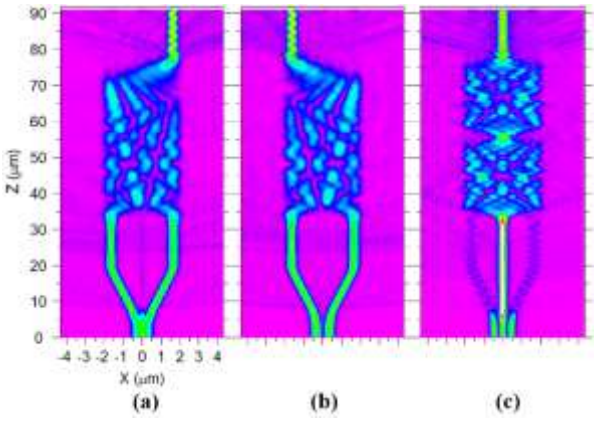

Fig.6: Intensity distribution along the demultiplexer for input mode (a) TE0, (b) TE1, (c) TE2. at 1530.3 nm.

Wavelength (nm)	I.L (dB)			C.T (dB)		
	TE0	TE1	TE2	TE0	TE1	TE2
1530.3	-1.4	-1.7	-1.4	-24	-23	-18
1569.6	-0.8	-0.73	-0.55	-19.3	-22.4	-17.3
1611.8	-1.17	-1.2	-1	-18	-25	-15

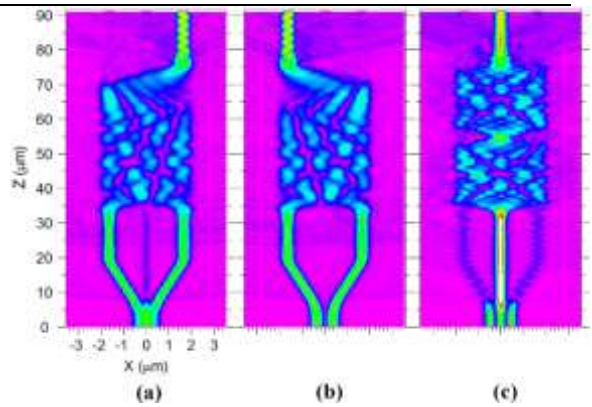

Fig.7: Intensity distribution along the demultiplexer for input mode (a) TE0, (b) TE1, (c) TE2. at 1611.8 nm.

To obtain the operating bandwidth of the designed device, both parameters are plotted over a certain wavelength and the 3 dB threshold from the optimum performance is used. The result is depicted in figure 8. It is clear that the designed device shows good performance of I.L > -3 dB and C.T better than −15 dB over 160 nm operating bandwidth covering (1490 to 1650) nm wavelength span which confirms that the designed device is capable to cover the C+L band of the optical spectrum.

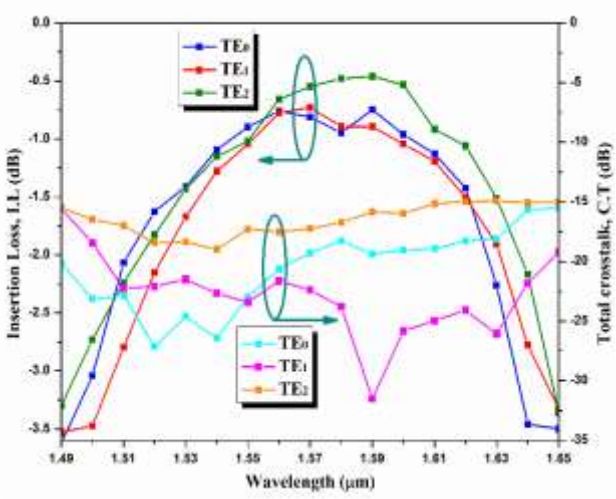

Fig. 8: Demultiplexer response dependency on operating wavelength.

Table 1 lists the insertion loss and crosstalk readings of the proposed device for each of the input mode cases at the wavelengths 1530.3, 1569.6, and 1611.8 nm.

Table (1) Device performance.

4. Fabrication Error Investigation

Errors during the fabrication process that may occur are investigated by checking the response of the proposed device to the deviation of its main parameters from their designed value based on the I.L and C.T measures. Table 2 lists the summary of the allowed fabrication errors measured in nm.

Table (2) Allowed fabrication error summary.

Parameter	Designed (μm)	Fabrication error (nm)	I.L (dB)	C.T (dB)
Λ_{MMI}	0.2	±2	>-2	<-15
w_{ps}	0.21	±15		
w_1, w_2	0.5, 0.3	±17, ±12		
W_{MMI}	4	±20		

5. Conclusions

In conclusion, a dual-band, compact, low loss, the three-mode demultiplexer is designed utilizing SWG technology. With popper parameters selection, such as pitch lengths, duty cycles, widths, and lengths of each part, desired functions can be achieved. The simulation and result show the proposed device has a loss > -1 dB, with 160 nm operating bandwidth extending over (1490 to 1650) nm wavelength span confirming its capability to cover the C+L band of the optical spectrum. Additionally, the device shows a high degree of compactness with an overall area of 80×4 μm^2. The device offers good performance even under fabrication imperfections. Finally, SWG technology served the target to obtain wideband, low loss, and fabrication tolerant devices.

References

[1] H. Xie et al., "An Ultra-Compact 3-dB Power Splitter for Three Modes Based on Pixelated Meta-Structure," IEEE PHOTONICS Technol. Lett., vol. 32, no. 6, pp. 341–344, 2020. doi: 10.1364/OFC-2020-W4C.4.

[2] H. Xie et al., “Highly Compact and Efficient Four-Mode Multiplexer Based on Pixelated Waveguides,” IEEE Photonics Technol. Lett., vol. 32, no. 3, pp. 166–169, 2020. doi: 10.1109/LPT.2020.2964308.

[3] K. T. Ahmmed, H. P. Chan, and B. Li, “Multi-Function Mode Processing Device for Mode Division Multiplexing Optical Networks,” IEEE Photonics Technol. Lett., vol. 33, no. 2, pp. 101–104, 2021. doi: 10.1109/LPT.2020.3041627.

[4] A. Bagheri, F. Nazari, and M. K. Moravvej-Farshi, “Tunable Optical Demultiplexer for Dense Wavelength Division Multiplexing Systems Using Graphene–Silicon Microring Resonators,” J. Electron. Mater., vol. 49, no. 12, pp. 7410–7419, 2020. doi: 10.1007/s11664-020-08522-y.

[5] R. Liu et al., “Integrated Dual-Mode 3-dB Power Splitter Based on Multimode Interference Coupler,” IEEE Photonics Technol. Lett., vol. 32, no. 14, pp. 883–886, 2020. doi: 10.1109/LPT.2020.3002344.

[6] A. Kaushalram et al., “Ultra-broadband fabrication-tolerant mode division (de)multiplexer on thin film Lithium niobate,” Opt. Commun., vol. 475, pp. 126251 (1-8), 2020. doi: 10.1016/j.optcom.2020.126251.

[7] J. P. Nath et al., “Compact Mode Division (de)Multiplexer Based on Collaterally Coupled SOI Waveguides,” IEEE Photonics Technol. Lett., vol. 32, no. 10, pp. 595–598, 2020. doi: 10.1109/LPT.2020.2985959.

[8] A. T. Tran et al., “A new simulation design of three-mode division (de)multiplexer based on a trident coupler and two cascaded 3 × 3 MMI silicon waveguides,” Opt. Quantum Electron., vol. 49, no. 426, pp. 1-15, 2017. doi: 10.1007/s11082-017-1248-4.

[9] W. K. Zhao et al., “Broadband five-mode (de)multiplexer with horizontal tapered directional couplers,” in: Asia Communications and Photonics Conference, 2017, pp. Su3K.7. doi: 10.1364/ACPC.2017.Su3K.7

[10] M. Cantono et al., “Opportunities and Challenges of C+L Transmission Systems,” J. Light. Technol., vol. 38, no. 5, pp. 1050–1060, 2020. doi: 10.1109/JLT.2019.2959272.

[11] T. Ahmed et al., “C + L-band upgrade strategies to sustain traffic growth in optical backbone networks,” J. Opt. Commun. Netw., vol. 13, no. 7, pp. 193–203, 2021. doi.org/10.1364/JOCN.427097.

[12] K. Minoguchi et al., “Beyond 100-Tb/s ultra-wideband transmission in S, C, and L bands over single-mode fiber,” Next-Generation Opt. Commun. Components, Sub-Systems, Syst. IX, vol. 11309, pp. 113090I (1-9), 2020. doi: 10.1117/12.2541990.

[13] W. K. Zhao, K. X. Chen, and J. Y. Wu, “Broadband mode multiplexer formed with non-planar tapered directional couplers,” IEEE Photonics Technol. Lett., vol. 31, no. 2, pp. 169–172, 2019. doi: 10.1109/LPT.2018.2887352.

[14] H. Shu, B. Shen, Q. Deng, M. Jin, X. Wang, and Z. Zhou, “A Design Guideline for Mode (DE) Multiplexer Based on Integrated Tapered Asymmetric Directional Coupler,” IEEE Photonics J., vol. 11, no. 5, pp. 1–12, 2019. doi: 10.1109/JPHOT.2019.2941742.

[15] W. K. Zhao et al., “Reconfigurable Mode (De)multiplexer with Integrated Thermo-Optic Long-Period Grating and Y-junction,” 2018 Conf. Lasers Electro-Optics, CLEO 2018 - Proc., vol. 30, no. 24, pp. 2119–2122, 2018. doi: 10.1364/OL.43.002082.

[16] D. Chen et al., “C + L band polarization rotator-splitter based on a compact S-bend waveguide mode demultiplexer,” Opt. Express, vol. 29, no. 7, pp. 10949, 2021. doi: 10.1364/oe.412992.

[17] Y. Wang et al., “Air-Core Ring Fiber Guiding >400 Radially Fundamental OAM Modes across S + C + L Bands,” IEEE Access, vol. 9, pp. 75617–75625, 2021. doi: 10.1109/ACCESS.2021.3078504.

[18] L. Sun et al., “Subwavelength structured silicon waveguides and photonic devices,” Nanophotonics, vol. 9, no. 6, pp. 1321–1340, 2020. doi: 10.1515/nanoph-2020-0070.

[19] D. Zhu et al., “High-Contrast and Compact Integrated Wavelength Diplexer Based on Subwavelength Grating Anisotropic Metamaterial for 1550/2000 nm,” IEEE Photonics J., vol. 13, no. 2, 2021. doi: 10.1109/JPHOT.2021.3061966.

[20] S. Han, W. Liu, and Y. Shi, “Ultra-Broadband Dual-Polarization Power Splitter Based on Silicon Subwavelength Gratings,” IEEE Photonics Technol. Lett., vol. 33, no. 15, pp. 765–768, 2021. doi: 10.1109/LPT.2021.3095257.

نحو مُضاعِف ارسال ثلاثي النمط بنطاق C + L
و باستخدام تقنية المحزز مادون الطول الموجي

زيد لطيف حسين* , رعد سامي فياض**

*معهد الليزر للدراسات العليا, جامعة بغداد, بغداد, العراق
**جامعة النهرين, كلية الهندسه, قسم هندسة الحاسوب, بغداد, العراق

الخلاصة: يقدم هذا العمل مضاعف إرسال ثلاثي ا لنمط واسع النطاق, مدمج, ومنخفض الخسارة صمم لتغطية نطاق C+L باستخدام تقنية المحزز مادون الطول الموجي (SWG) ومنصة SOI . تقدم تقنية ال SWG هندسة معامل الانكسار لعرض نطاق تشغيل أوسع وأجهزة مدمجة مقارنة بقريناتها التقليدية. يتعامل مضاعف الإرسال المصمم مع ثلاثة انماط TE0 TE1و TE2 وله خسارة > -1 ديسيبل وتداخل < -15 ديسيبل. الجهاز المصمم يغطي تشغيله 160 نانومتر (1490 إلى 1650 نانومتر) من الطول الموجي. الحجم الكلي للجهاز المصمم 80 × 4 ميكرومتر مربع.

Iraqi J. Laser, issue 1, vol., 21, pp. 51-60 (2022)

IRAQI JOURNAL OF LASER

Mechanical Properties of AISI 316L Stainless Steel Produced Via Selective Laser Melting

Raid Mohammed Hadi[1], Ziad Aeyad Taha[2]

raed.mohammed1001a@ilps.uobaghdad.edu.iq *Corresponding author:*

[1, 2] *Institute of Laser for Postgraduate Studies, University of Baghdad*

(Received 21/04/2022; accepted 18/07/2022)

Abstract Additive manufacturing has been recently emerged as an adaptable production process that can fundamentally affect traditional manufacturing in the future. Due to its manufacturing strategy, selective laser melting (SLM) is suitable for complicated configurations**.** Investigating the potential effects of scanning speed and laser power on the porosity, corrosion resistance and hardness of AISI 316L stainless steel produced by SLM is the goal of this work. When compared to rolled stainless steel, the improvement is noticeable. To examine the microstructure of the samples, the optical microscopy (OM), scanning electron microscopy (SEM), and EDX have been utilized. Hardness and tensile strength were used to determine mechanical properties. The results indicated that the samples were completely dissolved, and the hardness was 285HV. Compared with the models produced by other parameters, the best 0.3% porosity was obtained using 100 W laser power, a hatching distance of 70 µm, a layer thickness of 30µm, and a scanning speed of 600 mm/sec. In addition, the volumetric energy density value for the best result was 79 J/mm^3.

Keywords: Additive Manufacturing, Stainless Steel SS316L, Selective Laser Melting, Volumetric Energy Density, Corrosion Resistance

1. Introduction

Lasers are nowadays used in various industries, such as welding, drilling, cleaning, and ablation [1-3]. Additive manufacturing (AM) is an impressive field for lasers in industrial applications, and it has a promising future. AM technology has lately attracted a lot of attention, mainly because of its high effectiveness in producing light-weight components and its recognized usefulness in fabricating parts with complicated interior characteristics [4-9]. Metal powder-based technologies are currently employed in the dentistry sector to manufacture tiny, durable, and corrosion-resistant prostheses [10]. The Selective Laser Melting (SLM) technology involves manufacturing a fully dense part in a layer-by-layer manner through the selective melting of a metallic powder bed [11]. Whereas this technology has the potential to open new directions for manufacturing machine parts; it has some flaws. The recognized faults include porosity, incomplete powder melting, insufficient dimensional and shape correctness, and significant surface roughness [12]. The rapid emergence of SLM as an emerging technology has aroused the industry sector's interest. One and the foremost reason behind this rapid popularity is the wide spectrum of applications that can AM technology aid in producing efficiently regardless of their complexity. aerospace, automotive, medicine, engineering and are typical examples of nowadays and promising applications. The austenitic stainless steel AISI 316L is noted for its superior corrosion resistance and mechanical qualities. Austenitic stainless steel has higher percentages of Cr and Ni in its composition than those existing in the ordinary steel. The Ni

presence improves corrosion resistance and stabilizes the austenite phase at low temperatures; 316L is protected from corrosion by a Cr_2O_3 oxide layer [13]. Because of its superior flexibility and corrosion resistance, austenitic stainless steel is one of the most often utilized alloys in the maritime, biomedical, and aerospace industries [14]. The aim of the present work is to study the effect of several SLM-related parameter including the power and scanning speed on key mechanical properties such as the porosity, corrosion resistance, wear resistance, and micro hardness of stainless steel 316L specimens, and then to calculate the VED for each set of parameters. In addition to comparing corrosion resistance with 316L samples made using the traditional approach.

2. Materials and methods

The SLM method uses the gas-atomized 316L stainless steel powder as the principal material for specimen fabrication. The powder has a nominal composition of Fe-17Cr-13Ni-2.5Mo-0.03C and a particle size of < 65µm. Cubic specimens (10×10×10 mm^3), as shown in Fig 1, were fabricated by the SLM technique. To avoid an oxidation phenomenon occurring during laser melting, this process was performed in an argon atmosphere using a 3D printer (M100) equipped with a continuous wave and a fiber laser of 300W. An approximate laser beam of 80 µm was used for the fabrication of specimens. The layer thickness for all the models was 30 µm. Rectangular samples of (60 × 12 × 2) mm, were manufactured for the uniaxial tensile test, which was machined according to ASTM E8 standard, as shown in Figure 2. Energy-dispersive X-ray spectrometry EDX was used for inspecting the proportions of the produced stainless steel sample's elements, as shown in Figure 3. And table 1 shows the percentage of elements of SS316L .Figure 4 shows the diagram of how the SLM process is performed inside the SLM100 machine. The 316L SS powders are delivered through a powder feeder, which uses a moving drum to create a powder bed; it is then totally melted by heat energy from a continuous or pulsed laser beam, and the steps are repeated layer by layer until the required shape is achieved. The temperature during the process was 80 C. The specimens were not heat-treated after being manufactured. The best volumetric energy density was calculated after stabilizing the power and changing the speed. The volumetric energy density is computed by equation 1.

$$VED = \frac{p}{vhd}\ J/mm^3 \quad ----- \quad (1)$$

Fig. 1: SLM as-manufactured specimens**.**

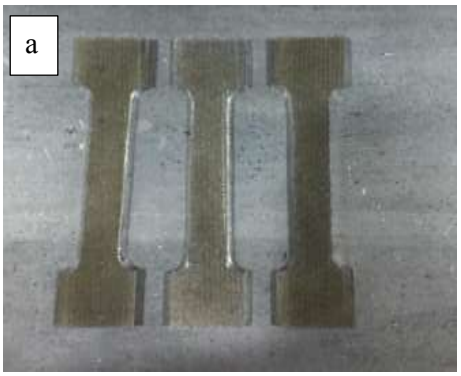

.

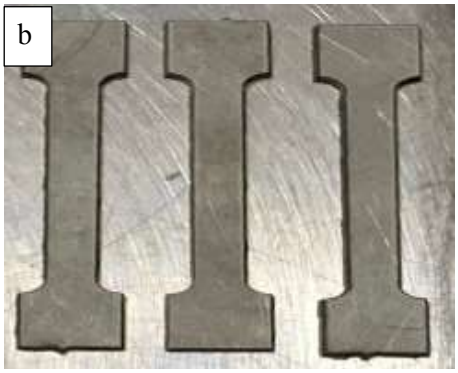

Fig. 2: **a**; SLM manufactured specimens **b**; conventionally manufactured, for tensile tests.

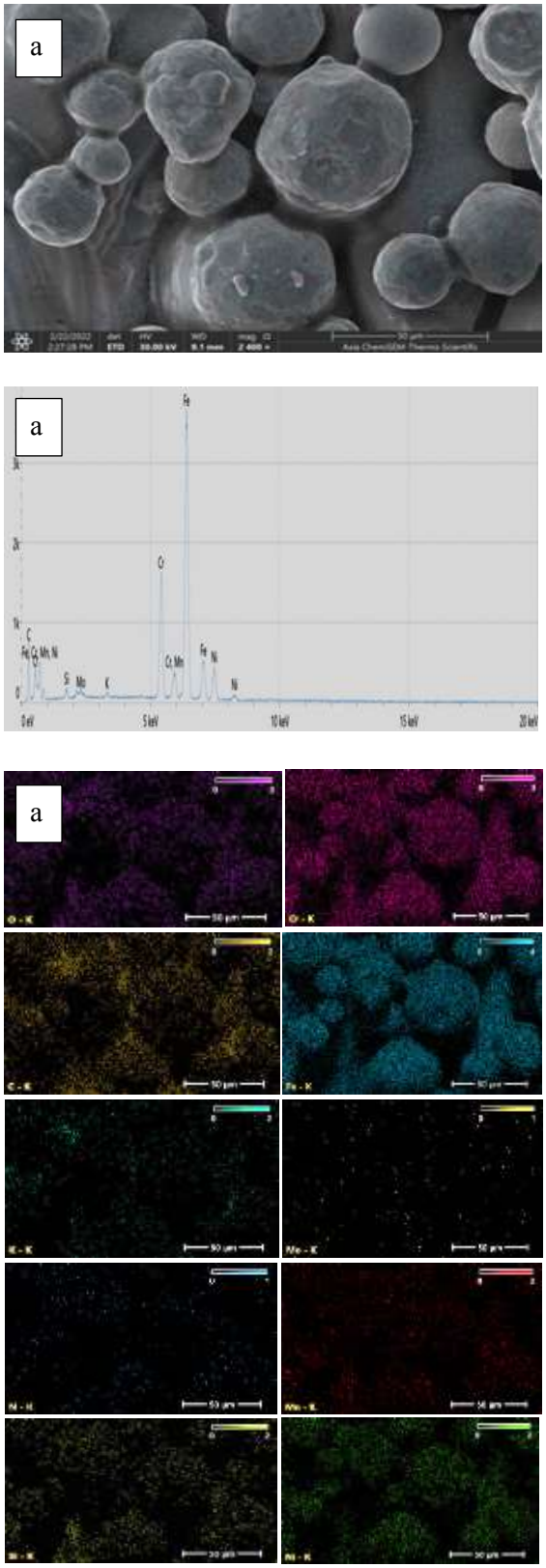

Fig. 3: EDX of AISI 316L by SLM. (a) SEM of the sample fabricated with a laser power of 100 W and scanning speed of 600 mm/s (b) EDX analysis performed on area marked. (c) EDX of individual elements maps

Where VED is the volumetric energy density of the powder bed (J/mm^3), P is the laser power (W), v is the laser scan speed (mm/s), h is the hatch distance (mm), and d is the powder bed layer thickness (mm) [15]. The corrosion test uses a Wenking MLab multichannel and SCI Mlab wear measurement system from Bank Electronics- Intelligent controls GmbH, Germany, as shown in Figure 5. A sliding wear resistance test was performed to investigate the coefficient of friction and the wear resistance of the AISI 316L, a steel ring was installed on the test machine, which was used for direct dry sliding contact with the testing surface of the sample, as shown in Figure 6.

Table (1) Shows the proportions of the ingredients of SS316L checked by EDS.

Weight % Error	Weight %	Atomic % Error	Atomic %	Element
0.6	17.4	1.5	42.8	C
0.5	2.4	1.0	5.1	N
0.5	6.8	0.9	12.6	O
0.0	1.0	0.0	1.0	Si
0.0	0.4	0.0	0.3	K
0.2	13.6	0.1	7.7	Cr
0.2	1.8	0.1	1.0	Mn
0.3	47.5	0.2	25.2	Fe
.2	7.6	0.1	3.8	Ni
0.9	1.6	0.3	0.5	Mo

Three groups have been made, each with a constant power at different speeds. The VED for each group was calculated by Equation No.1. The relationship between VED and porosity for each group after examining samples was then plotted to select the best criteria from each group. The relationship between VED and exact hardness was then determined to determine the best model among the pieces tested for wear and corrosion resistance. Figure 7 shows the relation between VED and porosity of each group. Figure 8 chooses the best sample from this set.

Table 2 summarizes the working procedures for this experiment.

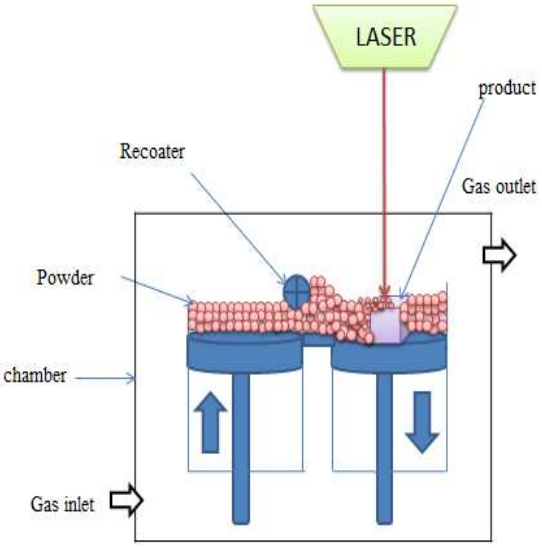

Fig. 4: schematic diagram that illustrates how the SLM process was conducted inside the machine.

Fig.5: Corrosion test

Fig. 6: wear test

Table (2) Experimental table of laser parameters.

Group	No	Power (W)	Scanning speed (mm/s)	VED ($J/mm^{3)}$
G1	S1	100	600	79
	S2	100	700	68
	S3	100	800	59
	S4	100	900	52
G2	S5	125	600	99.2
	S6	125	700	85
	S7	125	800	74.4
	S8	125	900	66
G3	S9	150	600	119
	S10	150	700	102
	S11	150	800	89
	S12	150	900	79

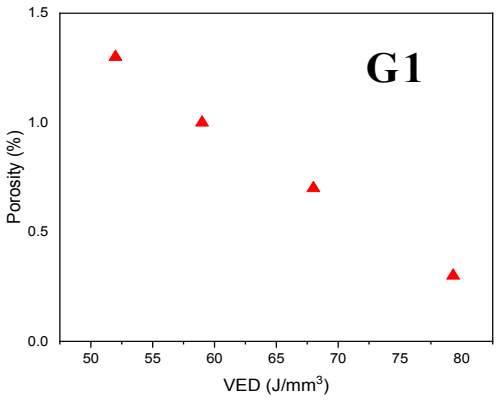

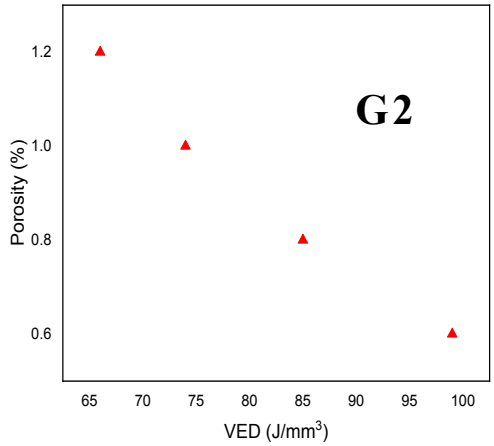

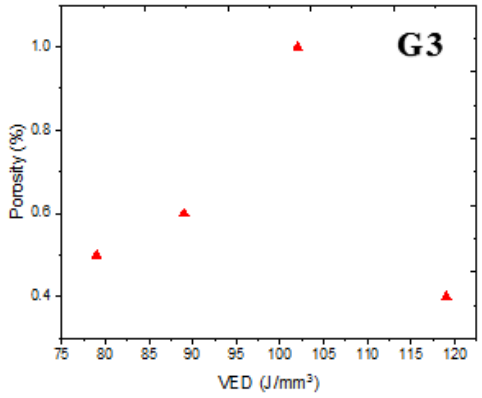

Fig.7: VED of samples produced with deferent porosity in G1, G2, G3**.**

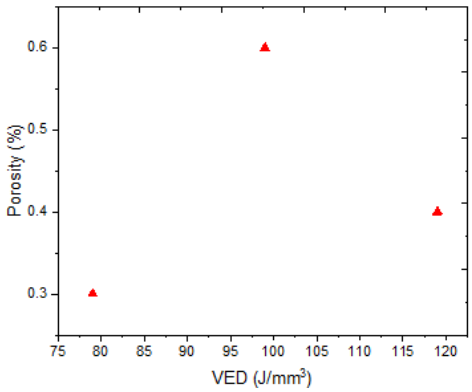

Fig. 8: The best graphic of the three groups to determine the best porosity and therefore the best parameters

3. Results and Discussion

The corrosion test results indicate that the SLM specimens are superior to the traditional samples. The mineral surface goes through three stages of behavior as shown in Fig 9. In addition, metal shows higher corrosion resistance and tends to be with uniform corrosion, where it is an inert layer with stable dynamic behavior. Pitting on the surface was apparent and very little, as in figure 10b, which means that the reaction with the solution occurs at a slow rate, and this means that the voltage continues as the inert layer continues. The potential increase to positive values (more noble alloy), meaning that the protection is higher[16] For the cast sample, the material began to interact due to interactions with the solution where it is clear from the beginning as in Figure 9. , The microstructure images in Figure 10a show that the surface corrosion of the poured sample is with clear and strong pitting, meaning that the protection range is very little. As a result of the interactions, where the layer stops creating and does not resist the oxidation reaction, and when the voltage rises, it generates bubbles that prevent the ions and electrons from interacting and therefore appear vertically. When it returns, it intersects the anodic curve at the point (0.328mA, 278mV), where it appears to have a limited scope for protection. Figure 11 depicts the SEM of the best sample at different magnifications as it reveals that some of the granules are bound to the body despite the completely dissolving powder. The remaining particle size of the adhesive powder and agglomerated particles appears at an additional magnification.

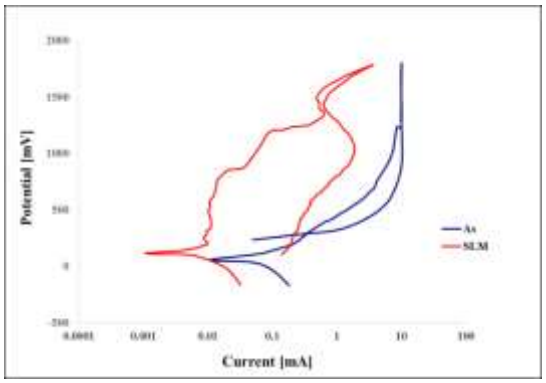

Fig. 9: Electrochemical characteristics of wrought stainless steel 316 L using, conventional method, SLM

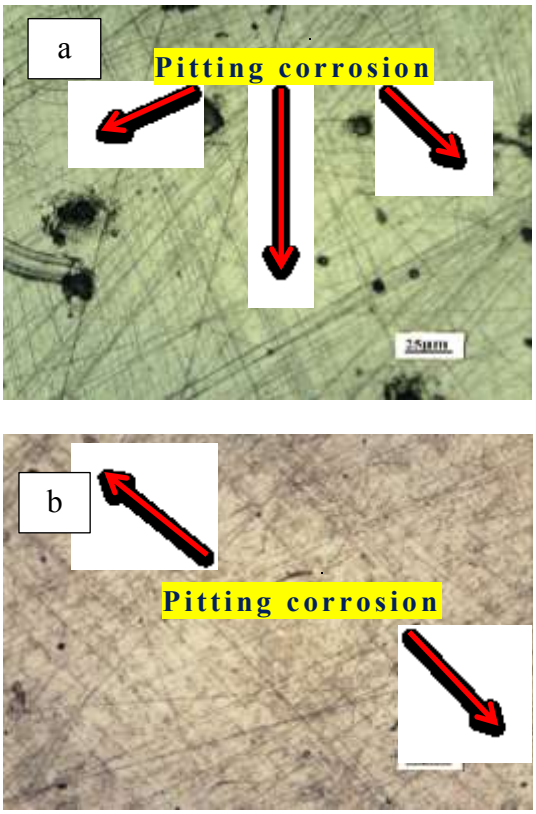

Fig. 10: Optical microscope of SS316L manufacturing by **a**; conventional method. **b**; SLM .

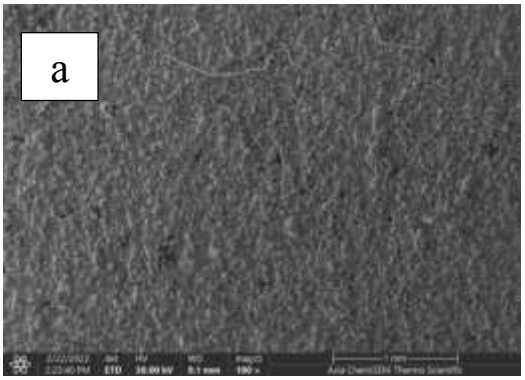

Fig. 11: SEM with magnification a; 100 X.

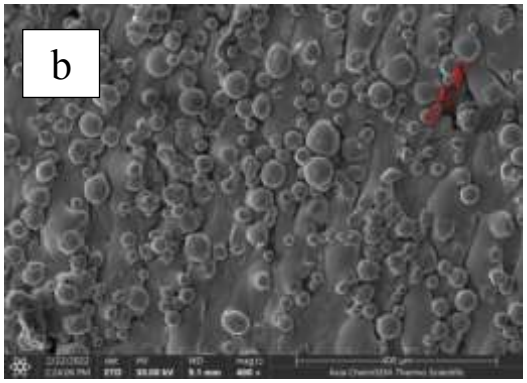

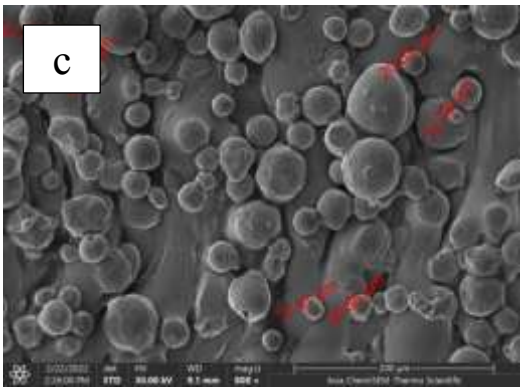

Fig. 11: SEM with magnification b; 400 X. c; 800X.

In the wear resistance test, the plowing process was evident in the rolled casting samples compared to the SLM-produced models; where the sliding type metal is clear and both pieces were subjected to the same load and period. The highest wear rate on the surface, and the difference gradually becomes less with increasing time. Wear is mainly through slippage of the load for the first time, and the microstructure is responsible for these properties. The product wear performance of SLM is better than that of rolled cast alloys, where the SLM samples were “ultra-hard” and more resistant to wear, with the time-frequency of the same load increases, as shown in Figure 12. A long period, the wear rate decreases due to the increase in deformation by removing parts of the sample surface after breaking the bumps. That is due to exposing the sample for a more extended period and thus more significant stress [17], as shown in Figure 13. The wear rate of

the SLM sample was 7.2E-9 (g/mm) while in rolled was 16E-9.

It was found that the difference in microhardness can be attributed to the scanning speed. Changes in the hardness value correspond to a certain scanning speed. Because the laser process has a fast cooling rate/cooling process, decreasing the scanning speed can lead to an increase in the heat accumulated in the material, which raises the temperature to the melting point and produces the molten phase. The highest hardness achieved was 285 HV for sample S1 of the first group, as shown in Figure 14, which has the highest density of 99.7% among the manufactured samples. These results of the high density that were obtained in the experimental are close to the literature by Bhowmik et al. [18], and Yusuf et al.[19].

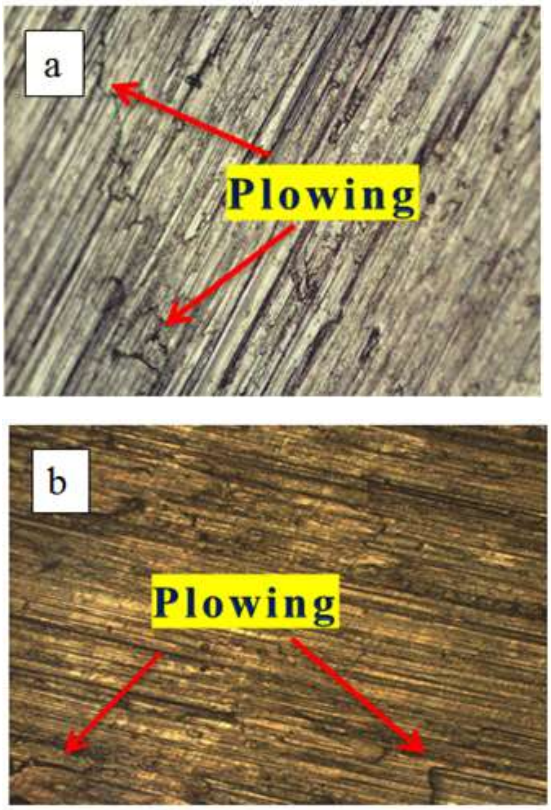

Fig. 12: Optical Microscope for Microstructure wear test for samples manufactured from SS316L **a)** Conventional method **b)** SLM.

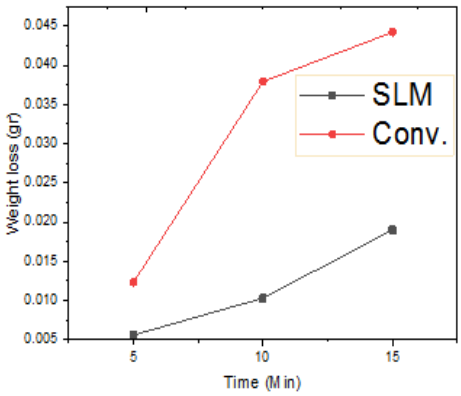

Fig.13: The difference in weight loss for rolled and SLM samples for the same load with a variable time.

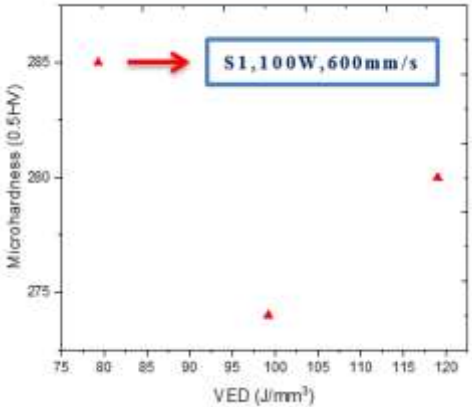

Fig.14: Micro hardness for samples with volumetric energy densitys.

In Figure 15, the samples were prepared and tested to measure the tensile strength at a junction velocity of 1 mm/min according to the ASTM-E8. According to Figure 16 (a), the rise in the load appears to reach 565MPa to break the SLM samples whereas it was 615MPa to break the rolled one. Figure 16 (b) reveals that while the high yield strength in the SLM case equals 480MPa and with low deformation of 9.8mm, the yield strength for rolled case was 260MPa and with high deformation of 27.9 mm. The intragranular cellular segregation network structure is confirmed to be the reason for improving the yield strength of the SLM SS316L compared with the SS316L fabricated by traditional methods [20].

Fig. 15: The tensile testing machine for tensile testing, samples after testing

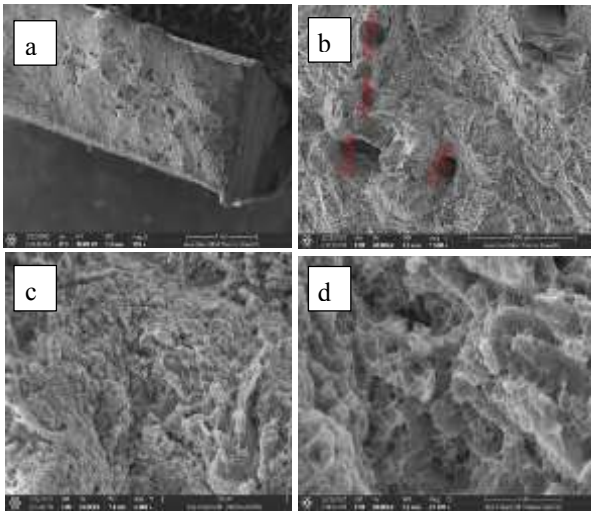

Fig. 17: Fractography for the SLM-316L sample after tensile strength. SEM images show (a) the fracture sample, (b) micro porosity, (c- d) completely melted regions.

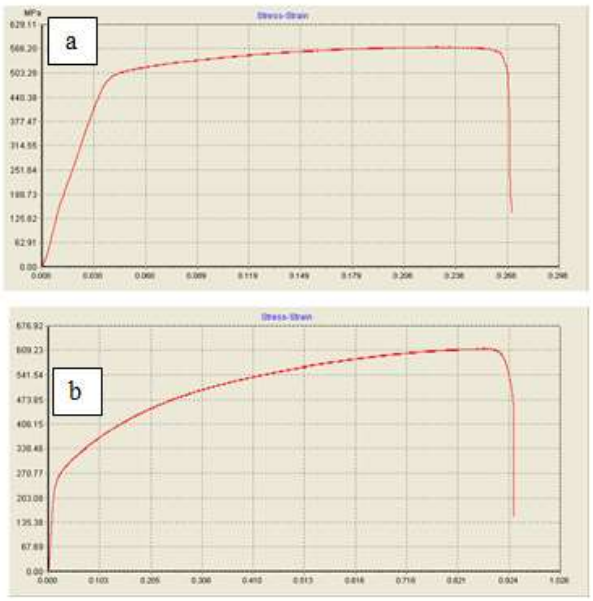

Fig. 16: Tensile strength for breaking sample a) 565MPa SLM b) 615MPa Conv.

The specimen fracture consists of uniformly distributed dimples. Most boils were larger than one micrometer and the dimples were uniform. More minor dimples indicate a lower deformation capacity. The micro pores in the sample of SLM can be noticed in Figure 17b.

Porosity is a common flaw in the SLM additive manufacturing and may adversely influence the mechanical characteristic. Gas-induced pores with nearly spherical shape occur during the gas deterioration of the 316L SS feedstock before the SLM process and may still present in the final product. [19]. The porosity lacks energy as it is insufficient to dissolve the powder completely. This leads to a lack of fusion or welding between each adjacent sweep and between successive layers. The excessive energy absorption leads to vaporization due to intense fusion, resulting in a keyhole. Fully molten areas are demonstrated in Figure 17(c) whereas Figure 17 (d) shows the boils.

4. Conclusions

The SLM316L proved a superior corrosion resistance over the as-cast counterpart due to a wider passive region, higher polarization resistance, and higher pitting potential. This was attributed to the lower density of micro-pores and the homogeneous distribution at the investigated scale. The SLM samples experience less plastic deformation than wrought samples. The wear resistance of the SLM parts is related to their high hardness and fine microstructure. The wear test reveals a highest and lowest wear due to the varying slip resistance under load. With increasing time, this distinction becomes less noticeable as the behavior in the SLM samples change. The results also show that the exact hardness of the samples ranges between 250 and 285 HV, and this was due to the different manufacturing parameters. This hardness was the highest compared to what was reported in the literature. The speed can play an important role in this criterion in the same manufacturing method. The analysis of the

image of the fractured sample after stretching under high magnification reveals that there is almost no porosity, indicating that the best sample of the selected groups is of the best parameter to achieve a high density of 99.7 percent.

References

[1] Z. A. Taha," Hole drilling of high density polyethylene using Nd: YAG pulsed laser", Iraqi Journal of Laser, vol. 18, no. 2, pp.41-46,2019.

[2] H. A. Jasim, G. A. Demir, B. Previtali, and A. Z. Taha, " Process development and monitoring in stripping of a highly transparent polymeric paint with ns-pulsed fiber laser," Optics & Laser Technology, vol. 93, pp. 60-66, 2017.

[3] A. F. Mutlak, M. Jaber, and H. Emad," Effect of Laser Pulse Energy on the Characteristics of Au Nanoparticles and Applications in medicine," Iraqi Journal of Science, PP. 2364-2369 , 2017.

[4]N. K. Rajak and Prof. A. Kaimkuriya, "Design and Development of Honeycomb Structure for Additive Manufacturing," International Journal of Trend in Scientific Research and Development, vol. Volume-2, no. Issue-6. South Asia Management Association, pp. 1198–1203, Oct. 31, 2018. doi: 10.31142/ijtsrd18856.

[5] R, Huang, et al, "Energy and emissions saving potential of additive manufacturing: the case of lightweight aircraft components," Journal of Cleaner Production, 135 PP.1559-1570. (2016).

[6]T. Xia et al., "Effect of Heat Treatment on Microstructure and Mechanical Properties of a Selective Laser Melting Processed Ni-Based Superalloy GTD222," Materials, vol. 14, no. 13. MDPI AG, p. 3668, Jun. 30, 2021. doi: 10.3390/ma14133668.

[7]L. E. Murr et al., "Fabrication of Metal and Alloy Components by Additive Manufacturing: Examples of 3D Materials Science," Journal of Materials Research and Technology, vol. 1, no. 1. Elsevier BV, pp. 42–54, Apr. 2012. doi: 10.1016/s2238-7854(12)70009-1.

[8]W. E. Frazier, "Metal Additive Manufacturing: A Review," Journal of Materials Engineering and Performance, vol. 23, no. 6. Springer Science and Business Media LLC, pp. 1917–1928, Apr. 08, 2014. doi: 10.1007/s11665-014-0958-z.

[9] N. T. Aboulkhair, N. M. Everitt, I. Ashcroft, and C. Tuck, "Reducing porosity in AlSi10Mg parts processed by selective laser melting," Additive Manufacturing, vol. 1–4. Elsevier BV, pp. 77–86, Oct. 2014. doi: 10.1016/j.addma.2014.08.001

[10]T. Kozior, J. Bochnia, P. Zmarzły, D. Gogolewski, and T. G. Mathia, "Waviness of Freeform Surface Characterizations from Austenitic Stainless Steel (316L) Manufactured by 3D Printing-Selective Laser Melting (SLM) Technology," Materials, vol. 13, no. 19. MDPI AG, p. 4372, Sep. 30, 2020. doi: 10.3390/ma13194372.

[11]Y. Huang et al., "Microstructure and wear properties of selective laser melting 316L," Materials Chemistry and Physics, vol. 254. Elsevier BV, p. 123487, Nov. 2020. doi: 10.1016/j.matchemphys.2020.123487

[12]A. Matras, "Research and Optimization of Surface Roughness in Milling of SLM Semi-Finished Parts Manufactured by Using the Different Laser Scanning Speed," Materials, vol. 13, no. 1. MDPI AG, p. 9, Dec. 18, 2019. doi: 10.3390/ma13010009.

[13]M. Mokhtari, P. Pommier, Y. Balcaen, and J. Alexis, "Laser Welding of AISI 316L Stainless Steel Produced by Additive Manufacturing or by Conventional Processes," Journal of Manufacturing and Materials Processing, vol. 5, no. 4. MDPI AG, p. 136, Dec. 14, 2021. doi: 10.3390/jmmp5040136.

[14]K. Chadha, Y. Tian, J. Spray, and C. Aranas, "Effect of Annealing Heat Treatment on the Microstructural Evolution and Mechanical Properties of Hot Isostatic Pressed 316L Stainless Steel Fabricated by Laser Powder Bed Fusion," Metals, vol. 10, no. 6. MDPI AG, p. 753, Jun. 05, 2020. doi: 10.3390/met10060753

[15]M. Letenneur, P. Imbrogno, A. Molavi Kakhki, and V. Brailovski, "Laser Powd Bed Fusion with Intentionally-Seeded Porosity for Prototyping of Powder Metallurgy Parts, " Journal of Manufacturing and Materials Processing, vol. 4, no. 4. MDPI AG, p. 119, Dec. 11, 2020. doi: 10.3390/jmmp4040119.

[16] X. Shang, Z. Wang, F. He, J. Wang, J. Li, and J. Yu, "The intrinsic mechanis of corrosion

resistance for FCC high entropy alloys," Science
China Technological Sciences, vol. 61, no. 2.
Springer Science and Business Media LLC, pp.
189–196, Oct. 17, 2017. doi: 10.1007/s11431
017-9114-1.
[17] Al-Khazraji, Mohammed Abdulateef Ahmed."Study Effect of Alternative Movement on rate of Dry and wet Wear and on The Microstructure of Structural Steel Type (A36ASTM)." DIYALA JOURNAL OF ENGINEERING SCIENCES 6.No.1, pp 24-36. (2013).
[18]A. Bhowmik, W. Zhai, W. Zhou, and S. M. L. Nai, "Characterization of carbide particle-reinforced 316L stainless steel fabricated by selective laser melting," Materials Characterization, vol. 179. Elsevier BV, p. 111360, Sep. 2021. doi: 10.1016/j.matchar.2021.111360.
[19]S. Yusuf, Y. Chen, R. Boardman, S. Yang, and N. Gao, "Investigation on Porosity and Microhardness of 316L Stainless Steel Fabricated by Selective Laser Melting," Metals, vol. 7, no. 2. MDPI AG, p. 64, Feb. 20, 2017. doi: 10.3390/met7020064.
[20]Y. Zhong, L. Liu, S. Wikman, D. Cui, and Z. Shen, "Intragranular cellular segregation network structure strengthening 316L stainless steel prepared by selective laser melting," Journal of Nuclear Materials, vol. 470. Elsevier BV, pp. 170–178, Mar. 2016. doi: 10.1016/j.jnucmat.2015.12.034.

الخواص الميكانيكية للفولاذ المقاوم للصدأ AISI 316L المُنتَج بواسطة الصهر الانتقائي بالليزر

رائد محمد هادي [1] زياد اياد طه [2]

[1، 2] معهد الليزر للدراسات العليا /جامعة بغداد

الخلاصة : لقد أثبت التصنيع الإضافي أنه عملية إنتاج قابلة للتكيف يمكنها تغيير التصنيع التقليدي بشكل أساسي في المستقبل. نظرًا لاستراتيجيتها التصنيعية ، فإن الصهر الانتقائي بالليزر (SLM) مناسب للتكوينات المعقدة. الهدف من هذا العمل هو التحقيق في تأثير سرعة المسح وقوة الليزر على المسامية ومقاومة التآكل والصلابة للفولاذ المقاوم للصدأ AISI 316L الذي تنتجه SLM. عند المقارنة بالفولاذ المقاوم للصدأ المدلفن ، فإن التحسن ملحوظ. لفحص البنية المجهرية للعينات ، استخدم الفحص المجهري البصري (OM) ، والمسح المجهري الإلكتروني (SEM) ، و EDX ،وكذلك قوة الشد والصلابة بالنسبة للخواص الميكانيكية . أوضحت النتائج أن العينات ذابت تماما وكانت الصلابة 285 HV. مقارنة بالنماذج التي تنتجها البراميترات الأخرى ، تم الحصول على أفضل مسامية 0.3٪ باستخدام طاقة ليزر 100 واط ، وفتحة مسافة 70 ميكرومتر ، وسمك طبقة 30 ميكرومتر ، وسرعة مسح 600 مم / ثانية. بالإضافة إلى ذلك ، كانت قيمة كثافة الطاقة الحجمية لأفضل النتائج 79 جول/ملم^3.